A reconstruction of temperature, ice volume and atmospheric CO_2 over the past 40 million years

Bas de Boer

ISBN 978-90-393-5732-3

Institute for Marine and Atmospheric research Utrecht (IMAU)
Faculty of Science, Department of Physics and Astronomy
Utrecht University, The Netherlands

Cover: Russell Glacier (Greenland, July 2010) with sea level curve from Fig. 3.1

A reconstruction of temperature, ice volume and atmospheric CO_2 over the past 40 million years

Een reconstructie van temperatuur, ijsvolume en CO_2 in de atmosfeer over de afgelopen 40 miljoen jaar

(met een samenvatting in het Nederlands)

PROEFSCHRIFT

ter verkrijging van de graad van doctor aan de Universiteit Utrecht
op gezag van de rector magnificus, prof. dr. G.J. van der Zwaan,
ingevolge het besluit van het college voor promoties
in het openbaar te verdedigen op

maandag 27 februari 2012 des middags te 2.30 uur

door

Bas de Boer

geboren op 4 april 1982 te Gorinchem

Promotoren:	Prof. dr. J. Oerlemans
	Prof. dr. L. J. Lourens
Co-promotor:	Dr. R. S. W. van de Wal

Financial support was provided by the Netherlands Organisation for Scientific Research (NWO) in the framework of the Netherlands Polar Programme (NPP).

The early bird catches the worm

De morgenstond heeft goud in de mond

Contents

Samenvatting

Het klimaat van de Aarde kent vele gezichten. Rond de evenaar heerst er grotendeels een warm en vochtig klimaat, de tropen. In de subtropen bevindt zich onder andere het extreem droge en hete klimaat van de woestijnen en rond de polen is het juist heel koud. Deze verschillen worden grotendeels veroorzaakt door het verschil in straling van de zon, die rond de evenaar het hele jaar veel hoger aan de hemel staat dan aan de polen. Hier verdwijnt de zon tijdens de wintermaanden zelfs helemaal onder de horizon. Regionale verschillen worden daarnaast ook veroorzaakt door bijvoorbeeld begroeiing, topografie, of de aanwezigheid van een ijskap of gletsjer.

Naast de straling van de zon wordt het klimaat ook beïnvloed door de broeikasgassen in de atmosfeer, zoals koolstofdioxide, methaan en ozon. De grootste bijdrage aan het broeikaseffect wordt echter geleverd door waterdamp. Het broeikaseffect - het invangen van langgolvige straling door de atmosfeer - zorgt voor een toename van de temperatuur op het oppervlak. Zonder dit effect zou de temperatuur op Aarde veel lager zijn dan in het huidige klimaat en zou de Aarde vrijwel niet leefbaar zijn. Tijdens de afgelopen 65 miljoen jaar, het Cenozoïcum, spelen beide effecten een belangrijke rol in veranderingen van het mondiale klimaat. Dit blijkt uit de vele beschikbare klimaatarchieven, zoals ijskernen, die terug gaan tot 800 000 jaar geleden en boringen van diepzee sedimenten die fossielen bevatten tot wel honderden miljoenen jaren geleden.

Op basis van deze gegevens zijn er verschillende periodes die opvallen. Een voorbeeld is de overgang van het Eoceen naar het Oligoceen, ca. 34 miljoen jaar geleden. Dit is een opmerkelijke periode met een grote daling van de temperatuur en voor het eerst een grote ijskap op Antarctica. Verschillende oorzaken worden genoemd voor deze snelle groei van ijs, zoals het overschrijden van een bepaalde waarde van koolstofdioxide (CO_2) in de atmosfeer, maar ook veranderingen in de oceaanstromingen. Een andere opvallende periode is de afgelopen miljoen jaar. Daarin vertoont het klimaat een grote variatie tussen hele koude periodes (een glaciaal) en warme periodes (een interglaciaal). Een glaciaal wordt gekenmerkt door grote ijskappen op het noordelijk halfrond, terwijl het klimaat tijdens interglaciale periodes ongeveer net zo warm of warmer is als het huidige interglaciaal waarin we ons nu bevinden wat het Holoceen wordt genoemd. De waarnemingen uit de ijskernen geven aan dat de grote variaties

van de temperatuur sterk samenhangen met de gemeten CO_2 in de luchtbelletjes opgesloten in dezelfde ijskern.

De variaties van de straling van de zon vertonen een duidelijke periodiciteit met bepaalde frequenties. Onder andere de schuine stand van de aardas en de vorm van de elliptische baan van de Aarde om de zon variëren in de tijd met periodes van tienduizenden jaren. Deze frequenties zijn ook vaak terug te vinden in de klimaatarchieven. Variaties in ijsvolume worden vaak gerelateerd aan deze periodische veranderingen van de baanparameters. Dit blijkt uit de gegevens over de afgelopen 800 000 jaar uit ijskernen, die vooral grote variaties vertonen door het groeien en smelten van de grote ijskappen op het noordelijk halfrond. Daarnaast is deze periodiciteit terug te vinden tot miljoenen jaren terug in de diepzeeboringen voor zowel variaties in ijsvolume als broeikasgassen.

In het geologische verleden zijn geen directe metingen beschikbaar van bijvoorbeeld temperatuur, broeikasgassen of ijsvolume, behalve dan de broeikasgassen uit de luchtbelletjes in de ijskernen. Hierdoor zijn we grotendeels afhankelijk van klimaatproxies. Dit zijn meetbare variabelen die gerelateerd kunnen worden aan veranderingen in bijvoorbeeld de hierboven genoemde variabelen. Een goed voorbeeld zijn boomringen. Door de veranderingen in dikte per jaar kunnen hieruit variaties in temperatuur en neerslag worden bepaald tot een paar duizend jaar terug. Voor lange tijdschalen zijn verhoudingen in isotopen van atomen één van de meest toegepaste klimaatproxies. Isotopen zijn atomen van hetzelfde chemische element en met hetzelfde aantal protonen, maar met een verschillend aantal neutronen, waardoor een verschil in atoommassa ontstaat. Van bijvoorbeeld zuurstof, met 8 protonen in de kern, zijn er drie stabiele isotopen op de Aarde, met 8, 9 en 10 neutronen. De lichtste, ^{16}O komt met 99,75% veruit het meeste voor. De hoeveelheid van deze stabiele isotopen per onderdeel van het klimaatsysteem kan behoorlijk verschillen. De "zwaardere" isotoop ^{18}O komt minder vaak voor in sneeuw op de polen, omdat verdamping van water, H_2O, een voorkeur heeft voor lichtere moleculen. Daarnaast heeft het ontstaan van neerslag weer een voorkeur voor zwaardere moleculen. Hierdoor bevatten wolken nog minder van de zwaardere isotopen van zuurstof zodat richting de polen de relatieve hoeveelheid ^{18}O steeds verder afneemt. Zodoende bestaat er een duidelijke relatie tussen de hoeveelheid ^{18}O in neerslag en temperatuur. Hoewel deze ook wordt beïnvloed door andere factoren, zoals seizoen variaties en de bronlocatie waar het water is verdampt.

Het aantal atomen van een stabiel isotoop wordt veelal gemeten in verhouding met de meest voorkomende isotoop. In het geval van zuurstof dus in verhouding met ^{16}O. Daarnaast wordt deze verhouding van isotopen, bijvoorbeeld ^{18}O / ^{16}O, vaak uitgedrukt ten opzichte van een standaardverhouding in promille (per duizend) ‰. Dit wordt weergegeven met een $\delta^{18}O$-waarde. In de loop van de twintigste eeuw zijn de $\delta^{18}O$-waardes steeds vaker gemeten uit de diepzee kernen van met name de gefossiliseerde schelpen (kalk, $CaCO_3$) van kleine eencellige beestjes genaamd foraminifera.

Een bepaalde soort van deze beestjes, benthische foraminifera, leeft op of rond de oceaanbodem. De δ^{18}O-waarde in de schelp wordt voornamelijk beïnvloed door de lokale diepwater temperatuur en het mondiale ijsvolume. De temperatuur heeft met name invloed op de opname van het CO_3 ion in de schelp. Uit het vergelijken van temperatuur en benthische δ^{18}O waarnemingen blijkt dat deze relatie negatief en vrijwel lineair is. Het groeien of krimpen van een ijskap heeft invloed op de hoeveelheid water die wordt verdampt uit de oceaan, wat weer wolken vormt en uiteindelijk zorgt voor sneeuwval op een ijskap. Door de verdamping van water vind er een verdeling van de isotopen plaats, hetgeen de δ^{18}O-waarde van het oceaanwater beïnvloedt. Een toename van ijs leidt tot een toename van de δ^{18}O-waarde van het oceaanwater. Het verdampte water bevat immers minder ^{18}O, waardoor de δ^{18}O-waarde van oceaanwater toeneemt. Die wordt uiteindelijk opgeslagen in de schelpen, wat weer leidt tot een toename van de benthische δ^{18}O-waarde.

Over de afgelopen decennia hebben vele diepzeeboringen een rijkdom aan informatie opgeleverd over klimaatveranderingen in het verleden. Dit proefschrift verschaft nieuwe inzichten in het klimaat, voortkomend uit de benthische δ^{18}O gegevens over de afgelopen 40 miljoen jaar, de periode met grote ijskappen op Aarde. De waarnemingen uit de diepzeeboringen tonen aan dat de benthische δ^{18}O-waarde wordt beïnvloed door twee klimaat variabelen, het mondiale ijsvolume en de lokale diepwater temperatuur. Met behulp van ijskapmodellen en een inventieve methode worden deze twee signalen gescheiden.

De beide signalen worden in het model berekend op basis van de bekende relaties met de benthische δ^{18}O-waarde. Ten eerste wordt de diepwater temperatuur bijdrage aan δ^{18}O-veranderingen bepaald door een negatieve en lineaire relatie tussen veranderingen in temperatuur en δ^{18}O ten opzichte van het huidige klimaat. De bijdrage van het ijsvolume wordt berekend op basis van behoud van massa tussen de δ^{18}O-waarde van het ijs en van het oceaanwater. Met een ijskapmodel wordt ijsvolume en de δ^{18}O-waarde van het ijs berekend. De volledige methode wordt uitgebreid besproken in hoofdstuk 2. Op de eerste plaats wordt de inverse routine uitgelegd. Uit de veranderingen in de benthische δ^{18}O-waarde wordt temperatuur afgeleid, wat de kern vormt van de methode. Met deze routine wordt een temperatuur anomalie berekend als functie van het verschil tussen de berekende en waargenomen benthische δ^{18}O-waarde 100 jaar later. Vervolgens wordt met behulp van deze temperatuur anomalie de nieuwe bijdrage van de ijskappen en van de diepwater temperatuur veranderingen bepaald, om daarna de benthische δ^{18}O-waarde voor de volgende tijdstap te berekenen.

De inverse routine wordt toegepast met twee verschillende ijskapmodellen, die uitvoerig worden besproken in hoofdstuk 2. Op de eerste plaats wordt in hoofdstuk 3, 4 en 5 een ééndimensionaal cirkel-symmetrisch ijskapmodel gebruikt. Dit model berekent ijsstromingen in een radiale richting over een kegelvormig continent. Met deze

versimpelde representatie van de ijskappen is het mogelijk om een simulatie te doen van 40 miljoen jaar, doordat de rekentijd vele malen verlaagd wordt in vergelijking met meer geavanceerde modellen. In hoofdstuk 6 wordt vervolgens een driedimensionaal ijskapmodel gebruikt, wat ijsdikte berekent op een tweedimensionaal grid en een driedimensionaal temperatuur en snelheidsveld bepaald over 15 verticale hoogtes binnen de ijskap. Het meer geavanceerde driedimensionale model wordt gebruikt voor kortere simulaties, tot een paar miljoen jaar geleden, maar biedt veel meer detail.

In hoofdstuk 3 wordt een set van vijf ééndimensionale ijskapmodellen gebruikt voor een reconstructie van temperatuur en ijsvolume over de afgelopen 35 miljoen jaar. De simulatie bevat drie modellen die representatief zijn voor de ijskappen op het noordelijk halfrond: Groenland, Noord-Amerika en Eurazië. Daarnaast worden er nog twee aparte modellen gebruikt voor Oost- en West-Antarctica. Elk model heeft zijn eigen bodemtopografie die zodanig wordt afgestemd dat het gemodelleerde ijsvolume overeenkomt met waarnemingen en/of bevindingen met het driedimensionale model. De simulatie met de versimpelde ééndimensionale modellen komt goed overeen wat betreft temperatuur en ijsvolume met een veel gedetailleerde simulatie met driedimensionale modellen over de afgelopen drie miljoen jaar. Gemiddeld genomen zijn de verschillen slechts 1.0 °C voor temperatuur en 6.2 m voor de mondiaal gemiddelde zeespiegel. Ook wordt er gekeken naar de gevoeligheid van verschillende parameters in het model en wat de invloed van verschillende waarden is op de modelresultaten.

Vervolgens wordt in hoofdstuk 4 een meer grondige bestudering van de resultaten uit hoofdstuk 3 gepresenteerd. In de wetenschapsliteratuur worden vaak aannames gebruikt om de benthische δ^{18}O-waarde te verdelen in de ijsvolume- en temperatuurbijdragen. Een voorbeeld hiervan is een constante schaling tussen zeespiegelvariaties en variaties in de δ^{18}O-waarde van het zeewater. Met een aantal gevoeligheidsexperimenten wordt de bijdrage van de ijskappen aan de benthische δ^{18}O-waarde bekeken door de huidige δ^{18}O-waarde van het ijs te variëren. Gedurende de afgelopen 40 miljoen jaar toont het model aan dat de verhouding tussen de zeespiegel en δ^{18}O-waarde van het zeewater niet constant is, alhoewel gemiddeld genomen de waarde redelijk in de buurt komt van de algemeen aangenomen waardes van 1.0-1.1 ‰ per 100 meter zeespiegelverandering. Daarnaast wordt bekeken hoe ijsvolume-veranderingen zich verhouden tot variaties in temperatuur. Tijdens de vroegere periodes worden ijsvolume-variaties gedomineerd door de Antarctische ijskap. De toe- of afname van Antarctisch ijsvolume ten opzichte van de temperatuur variaties zijn de grootste in vergelijking met de ijskappen op het noordelijk halfrond. Dit hoofdstuk toont aan dat dit variabele gedrag door de tijd erg belangrijk is voor de interpretatie van de waarnemingen, met name ten opzichte van klimaat gevoeligheid en klimaat verandering over de afgelopen 40 miljoen jaar.

De toepassingen met het ééndimensionale model wordt afgesloten in hoofdstuk 5. Hierin wordt de gemodelleerde temperatuur gebruikt om een reconstructie te maken

van CO_2 over de afgelopen 20 miljoen jaar. De afkoeling tijdens het Cenozoïcum wordt grotendeels toegewezen aan een afname van CO_2 concentraties in de atmosfeer. Naast de metingen uit de ijskernen die teruggaan tot 800 000 jaar geleden is er echter geen onafgebroken reeks van CO_2 beschikbaar over deze periode. Een volledig beeld van bijvoorbeeld de aanvang van ijsgroei op het noordelijk halfrond, ca. 2.8 miljoen jaar geleden, ontbreekt hierdoor. In dit hoofdstuk wordt de temperatuursreconstructie uit hoofdstuk 3 vergeleken met de metingen van CO_2 uit de ijskernen. Hieruit wordt een (lineaire) relatie afgeleid die gebruikt wordt om verschillende klimaatproxies voor CO_2 tot 20 miljoen jaar te selecteren. De proxies die hetzelfde verloop vertonen ten opzichte van temperatuur worden gebruikt voor de reconstructie van een onafgebroken reeks van CO_2. Deze lange termijn relatie wordt aan de hand van een grafische analyse tussen temperatuur en de verschillende datasets van CO_2 bepaald. Ook wordt er een theoretische berekening van de gevoeligheid van temperatuur voor CO_2-variaties uitgevoerd. Hierin wordt o.a. rekening gehouden met korte- en lange-termijn terugkoppeling in het klimaatsysteem en veranderingen van andere broeikasgassen. De beide berekeningen komen goed met elkaar overeen en de klimaatgevoeligheid is vrijwel constant voor de gehele periode van 20 miljoen jaar.

In hoofdstuk 6 wordt vervolgens dezelfde inverse routine gebruikt voor een simulatie met driedimensionale ijskapmodellen. Over de afgelopen 1 miljoen jaar wordt een simulatie uitgevoerd met modellen voor Antarctica, Groenland, Noord-Amerika en Eurazië. De begincondities voor de vier modellen zijn gebaseerd op waarnemingen van de huidige topografie, de neerslag en de temperatuur. Door de vier ijskappen tegelijkertijd te simuleren is het mogelijk om een uitgebreide analyse uit te voeren van de individuele bijdrages aan de veranderingen van de gemiddelde zeespiegel over de afgelopen 1 miljoen jaar. Hieruit volgt dat tijdens glaciale periodes de Antarctische en Groenlandse ijskappen ongeveer 10% hebben bijgedragen aan de zeespiegel daling. De grote ijskappen op het noordelijk halfrond zijn verantwoordelijk voor de overige 90 %. Een vergelijkbare berekening is ook gedaan voor de bijdrage aan de variaties in de δ^{18}O-waarde van het zeewater van de verschillende ijskappen. Dit wordt berekend als functie van veranderingen in ijsvolume en δ^{18}O-waarde van het ijs. Door de veel lagere waarde van de δ^{18}O-waarde van de Antarctische ijskap, veroorzaakt door lagere temperaturen en een hoger oppervlak, is de bijdrage van Antarctica en Groenland ongeveer 10 tot 20% tijdens glaciale periodes. Als laatste is bekeken hoe de individuele ijskappen reageren op afzonderlijke daling van de zeespiegel of van temperatuur. Uit deze simulaties blijkt dat het ijsvolume op Antactica toeneemt voor een daling van de zeespiegel. Dit wordt versterkt als de daling van de temperuur wordt meegenomen. Alleen een temperatuursdaling heeft geen toename van ijsvolume tot gevolg. Echter de ijskappen op Eurazilë en Noord-Amerika gaan juist groeien voor een daling in temperatuur, wat wordt versterkt als de zeespiegeldaling wordt meegenomen.

1

Introduction

The Cenozoic era covers the past 65 million years of the Earth's history, and is characterised by a wide range of different climate states. During the Eocene epoch, starting 55 million years ago, the climate cooled down significantly and ends with the inception of a large Antarctic ice sheet, around 34 million years ago. Throughout the next two epochs, the Oligocene and Miocene, significant ice volume on Earth predominantly existed on Antarctica. Succeeding, the continent was covered by an ice sheet similar to its present-day form during the Late Miocene, ca. 10 million years ago. Glaciation on the Northern Hemisphere initiated around 2.8 million years ago, when the global average temperature significantly dropped below the present day temperature. During the Pleistocene, the past 2.6 million years, there is strong variability between glacial and interglacial climate stages. The former is characterised by significant ice sheets on both hemispheres, whereas the latter only includes ice on Antarctica and (partially) Greenland, similar to the current interglacial: the Holocene. Information of past climate on these long time scales predominantly originates from deep-sea sediment cores. Changes in for example temperature and sea level can be deduced from oxygen isotope ratios that are measured from fossilised calcite shells embedded in the sediment. In this chapter, an introduction is given on past climate variability as is indicated by the deep-sea sediment cores. Additionally, the influence of solar radiation on the climate system is described. Furthermore, it is shown that a separate signal for both climate variables can be obtained from the oxygen isotope ratios. This can be used to reconstruct ice volume and temperature over millions of years.

1.1 Earth's climate over the past 65 million years

During the past 65 million years (Myr), the climate of the Earth has changed significantly. Through the course of the Cenozoic the climate cooled down from a warm climate dominated by high values of greenhouse gases (e.g. Royer, 2006), to an ice-sheet dominated climate since the Eocene-Oligocene transition (about 40 Myr ago; e.g. Shackleton and Kennett, 1975; Lear et al., 2000; DeConto and Pollard, 2003b). Prior to the Cenozoic era, the climate of the Cretaceous (from 145 to 65 Myr ago) was characterised by a globally warm climate. Sea level stands were high (e.g. Kominz et al., 2008) and CO_2 levels were thought to be as high as 2000 parts per million (ppm) (e.g. Royer, 2006). Moreover, fossils of warm-adapted vegetation and animals have been found in high latitudes (Ruddiman, 2008). Also, temperatures are deduced to have been substantially higher than today, coinciding with a lower meridional temperature gradient (Littler et al., 2011).

The start of the Cenozoic is characterised by the K-T (Cretaceous-Tertiary) Boundary. A mass extinction event well known for the demise of the dinosaurs, which occurred around 65 Myr ago. Predominantly, the K-T Boundary is thought to have been caused by a large meteorite impact (e.g, Alvarez et al., 1980). Although temperatures remained relatively warm thereafter, long-term cooling initiated around 49 Myr ago in the Early Eocene. The long-term cooling trend is largely assumed to be related to a decrease in atmospheric pCO_2 (Zachos et al., 2001). The cooling trend leads to the first initiation of Antarctic ice during the Late Eocene, as is illustrated in Fig. 1.1. The figure shows deep-sea benthic $\delta^{18}O$ measurements from marine sediment cores, which indicates variations in temperature and sea level (Zachos et al., 2008). This data is used throughout this thesis and will be thoroughly explained in Section 1.4.

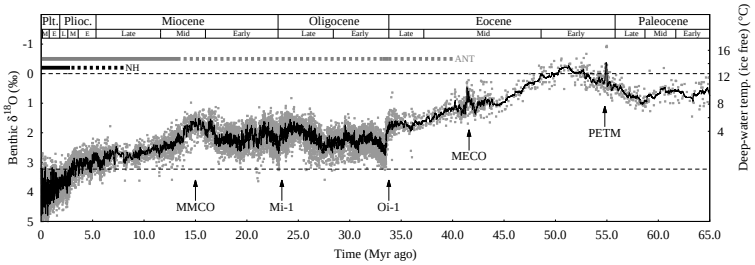

Figure 1.1 | *Benthic $\delta^{18}O$ in the Cenozoic era.* *Stacked benthic $\delta^{18}O$ from Zachos et al. (2008) indicating fluctuations in both ice volume and temperature. On top the Geological time scale: Plt: Pleistocene, Plioc: Pliocene, horizontal bars indicates the presence of the Antarctic ice sheet (grey) and Northern Hemisphere glaciation (black), for either partial (dashed) or full scale glaciation (solid). Bottom dashed line indicates the present day value of 3.23‰. MMCO: Mid-Miocene Climate Optimum, Mi-1: Miocene isotope excursion 1, Oi-1: Oligocene isotope excursion 1, MECO: Mid-Eocene Climate Optimum, PETM: Paleocene-Eocene Thermal Maximum. The right y-scale indicates deep-water temperatures for ice-free conditions.*

The knowledge on past climate, i.e. paleoclimate, largely emerges from the marine records retrieved from deep-sea sediments. A wealth of data has been obtained through international collaborative projects, such as the Integrated Ocean Drilling Program (IODP). The IODP started in 2003 and continued on earlier projects such as the Deep Sea Drilling Project (DSDP) and the Ocean Drilling Program (ODP). During the course of the Cenozoic a few distinct periods emerge from the stacked record, a compilation of multiple sediment cores, as shown in Fig. 1.1.

The PETM

Around the boundary of the Paleocene and Eocene, ∼55 Myr ago, a strong warming event (hyperthermal) is clearly identified in the benthic δ^{18}O records. This event is called the Paleocene-Eocene Thermal Maximum (PETM) (e.g. Kennett and Stott, 1991; Sluijs et al., 2006). The marine records show a strong decrease of carbon isotopes and calcite ($CaCO_3$) (Zachos et al., 2005) indicating a high input of greenhouse gas concentrations in the atmosphere. During this period, which lasted around 200,000 years (200 kyr), temperatures increased by 4-8 °C (Tripati and Elderfield, 2005).

The MECO

Another hyperthermal, which occurred during the long-term cooling trend around 40 Myr ago, is the Mid-Eocene Climate Optimum (MECO). Similarly to the PETM, this warming event is related to high values of greenhouse gasses (Bijl et al., 2010). The MECO is indicated by an increase in both surface and deep-water temperatures of about 5 °C (Bohaty et al., 2009) over a period of about 0.5 Myr.

Oi-1

The most distinct climate transition in the Cenozoic is the Eocene-Oligocene transition, ∼34 Myr ago, also known as Oi-1 (Miller et al., 1991). The transition is widely known as being the first period when major glaciation occurred on the Antarctic continent (Shackleton and Kennett, 1975). Several causes have been proposed, such as a threshold response to a decrease in atmospheric CO_2 concentrations or the opening of ocean gateways (DeConto and Pollard, 2003b). As is indicated by the benthic δ^{18}O records, the climate cooled significantly in the atmosphere and in the deep-ocean according to a two-step pattern (Coxall et al., 2005).

Mi-1 and MMCO

During the course of the Miocene, several oxygen isotope excursions appear in the benthic δ^{18}O records related to fluctuations in ice volume (Miller et al., 1991; Holbourn et al., 2005). One of the strongest excursions is the Mi-1 event occurring at the

Oligocene-Miocene boundary. Also shown to be related to a strong increase in ice volume and lower temperatures (Liebrand et al., 2011). Furthermore, another marked period is the Mid-Miocene Climate Optimum (MMCO), a warm period lasting for about 2 Myr with little glaciation and warmer than present day (PD) temperatures (You et al., 2009). Following the MMCO, ice volume increased rapidly leading to a permanent large ice sheet on Antarctica. Similarly, to the Oi-1 event several causes have been hypothesised, such as a decrease in pCO_2 (Langebroek et al., 2009).

Plio-Pleistocene climate

Over the past 5 Myr, during the Pliocene and Pleistocene, the Earth's climate was strongly fluctuating as indicated by the benthic $\delta^{18}O$ data in Fig. 1.1. The benthic $\delta^{18}O$ data mostly has values higher than PD that indicate temperatures below PD and the presence of large ice sheets on the Northern Hemisphere (NH) (Emiliani, 1955; Chappell and Shackleton, 1986; Bintanja et al., 2005a). Glaciation on the NH initiated during the Mid Pliocene, around 2.8 Myr ago (Whitman and Berger, 1992; Sato and Kameo, 1996).

During the Pleistocene ice ages, vast ice sheets covered the NH continents and an Antarctic ice sheet expanded to the continental edge, as illustrated in Fig. 1.2. Due to the large increase of ice volume on land, regional sea level has been as low as ∼120 meters below PD sea level (Lambeck and Chappell, 2001; Rohling et al., 2009). The origin of the Pleistocene ice ages is strongly coupled to variations in solar forcing.

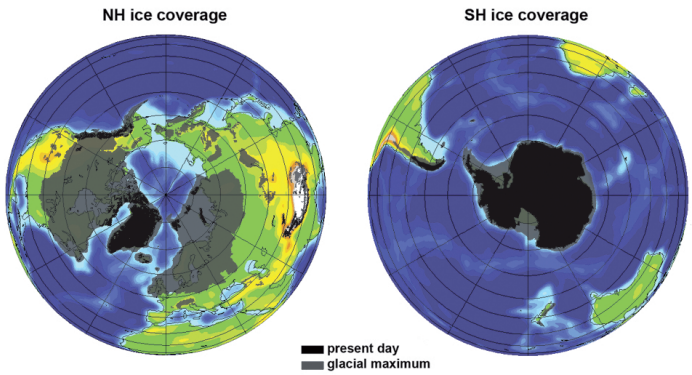

Figure 1.2 | *Pleistocene ice coverage.* *Ice coverage during the Pleistocene glacial cycles (Ehlers and Gibbard, 2007). On the left for the Northern Hemisphere, on the right for the Southern Hemisphere. Maximum glaciation is shown in transparent grey, the PD ice coverage is shown in black. Topography is from the SRTM30_PLUS dataset (Becker et al., 2009).*

1.2 Variability in Solar forcing

The cyclic behaviour during the Plio-Pleistocene, but also during earlier stages in the Cenozoic, is related to the main driver of the Earth's climate: The Sun. Solar insolation varies on many different time scales, from 10 kyr to millions of years (Berger and Loutre, 1992; Laskar et al., 2004). These frequencies are prominently reflected in the climate records from the marine sediments (Hays et al., 1976; Imbrie et al., 1992, 1993). The influence of astronomical variations on the climate is called the Milankovitch theory (Milankovitch, 1930), describing the three variations in solar insolation, i.e. eccentricity, precession and obliquity (see Fig. 1.3). All three Milankovitch cycles vary at their own frequencies, and have their own distinct influences on the distribution of solar insolation over the Earth.

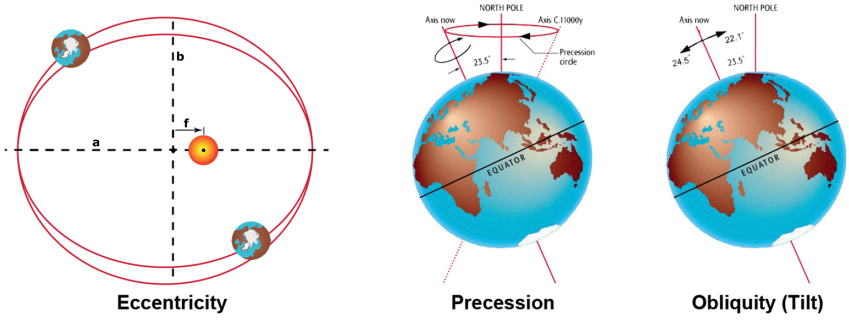

Figure 1.3 | *Milankovitch cycles.* *The three major variations in solar insolation, first described by Milankovitch (1930). From left to right: Eccentricity refers to variations in the Earth's orbit around the sun; Precession refers to wobble cycle of the axis of rotation; Obliquity refers to variations in the tilt of the axis of rotation of the Earth.*

Eccentricity

The orbit of the Earth around the sun is an ellipse, for which eccentricity is a measure of the elliptic shape of the orbit. Eccentricity is defined as ε = f/a, the ratio between the semi-major axis and the distance from a focal point to the center, see Fig. 1.3. The sun is located in one of the two focal points of the ellipse. The orbital eccentricity varies around a mean value of 0.028, with a maximum value of 0.058 and a minimum, nearly a circle (ε = 0), of 0.005. At present, the orbit has an eccentricity of 0.017. The major long-term period is 413 kyr, while the most well known frequency is that of 100 kyr, a combination of 95 and 125 kyr cycles. Eccentricity is the only orbital parameter which influences the global mean annual insolation, although the impact is very small. Additionally, eccentricity modulates precession.

Precession

The direction of the Earth's axis of rotation wobbles around a fixed line, which is perpendicular to the orbital plane. This motion is caused by tidal forces of the Sun and Moon exerted on the solid Earth, modulated by the shift of the entire elliptically shaped orbit of the Earth. The combined effect is called climatic precession, or just precession. Naturally, if the orbital shape were a circle, i.e. $\varepsilon = 0$, this effect would disappear. The two major periods of precession are 19 and 23 kyr, regulating the position of the seasons on the orbit (e.g. Berger and Loutre, 1992).

Obliquity

The angle of the axis of rotation (tilt) varies with respect to a fixed line perpendicular to the orbital plane of the Earth between a value of 22.1° and 24.5°. Currently, the axis is tilted at 23.44° and is slowly decreasing. The main period, the time it takes to shift between the maximum and minimum values and back, is 41 kyr. The change in tilt mainly influences the absorbed solar insolation at higher latitudes.

Orbital cycles and past climate

Over the past few decades, numerous studies have related climate variations during the Cenozoic to the different frequencies in insolation for the marine records of; the PETM (Lourens et al., 2005), the Miocene (Holbourn et al., 2005), and the Pleistocene (Hays et al., 1976). Other examples are given by Oerlemans (1980, 1982), relating insolation to ice-sheet variations during the past glacial cycles. Shackleton (2000) performed a combined analysis of deep-sea sediments and ice-core records, and Liebrand et al. (2011) used a combination of deep-sea sediment data and ice-sheet simulations for the Miocene.

Furthermore, a striking dissimilarity has been observed between the deep-sea records and insolation variations during the Pleistocene. During the mid 1970s, Hays et al. (1976) already noticed that the main periodicity of the climate signal shows an increase in 100-kyr periods, whereas the insolation data shows a decrease over time in 100-kyr power (see also Imbrie et al., 1993). This change in the frequency is also related to the the so-called 'Mid-Pleistocene Transition' (MPT). The MPT indicates the transition from dominant 41-kyr (obliquity) to 100-kyr glacial cycles between 0.8 and 1.2 Myr ago. Several explanations have been proposed, predominantly induced by non-linear responses within the climate system. For example; the merging of ice sheets (Bintanja and Van de Wal, 2008); the interaction between ice-sheets and subglacial sediments (Clark and Pollard, 1998); or a non-linear response to obliquity cycles (Huybers, 2007). The latter has also been identified in the ice-core records (Jouzel et al., 2007), and for earlier Pleistocene glacial cycles (Lourens et al., 2010).

1.3 Past changes in the carbon cycle and CO_2

The climate during the Pleistocene is dominated by cyclic behaviour due to the waxing and waning of large ice sheets in the NH. This variability is not only related to changes in solar insolation. Also variability in atmospheric greenhouse gasses are shown to have strong coherence with ice volume and temperature. Predominantly CO_2 measurements from ice cores are shown to have a strong link to temperature and the orbital frequencies (e.g. Petit et al., 1999; Siegenthaler et al., 2005; Lüthi et al., 2008), as is illustrated in Fig. 1.4.

The interaction between greenhouse gasses, temperature and ice volume is not straightforward. For the atmosphere an increase in for example CO_2 leads to a stronger greenhouse effect. This enhances absorption of longwave radiation from the Earth and warms the lower atmosphere and the surface. Naturally, changes in atmospheric CO_2 concentrations also induce changes in the global carbon cycle. Therefore also changing sources and sinks with the biosphere, soil and the ocean (e.g. Köhler and Fischer, 2006). Besides, positive and negative feedbacks between the different reservoirs influence CO_2 in the atmosphere, but are also dependent on temperature.

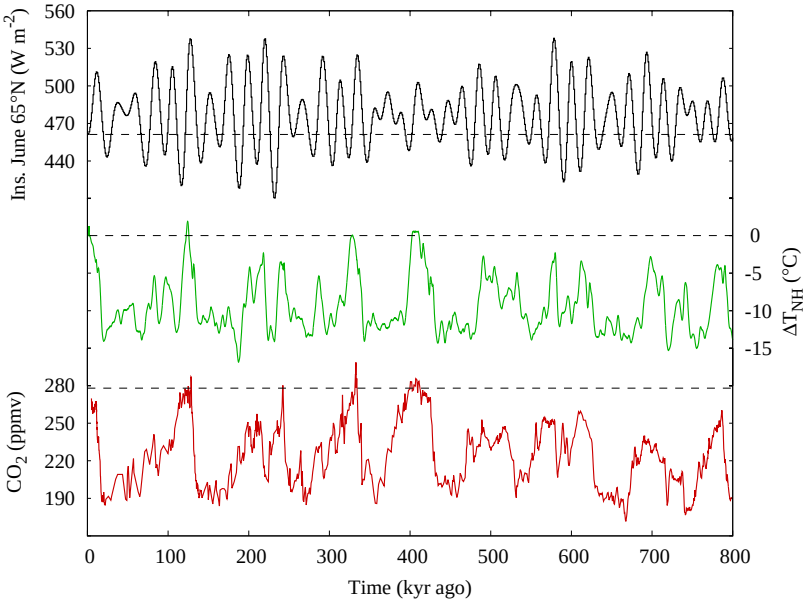

Figure 1.4 | *Pleistocene climate variability.* *Insolation, temperature and CO_2 variability during the past 800 kyr, from top to bottom: June 65° N insolation (black; Laskar et al., 2004), modelled NH surface-air temperature relative to PD (green) and CO_2 from the EPICA Dome C ice core (red: Lüthi et al., 2008). The dashed lines indicate the present day values, in case of pCO_2 the pre-industrial value of 278 ppm (In 2011 the concentration was about 390 ppm).*

In general, the prevailing picture that emerges from the ice-core record shown in Fig. 1.4 is a positive and quite steady relationship between CO_2 and temperature. In terms of leads and lags, the pCO_2 data from the ice-core records actually lags temperature (from the ice-core record on the same time scale) for most time periods. Accordingly, it does not necessarily mean that one variable influences the other, but rather that a (more or less) steady relationship exists between different components of the climate system, at least for this period in time (Siegenthaler et al., 2005).

1.4 Isotope ratios as climate indicators

To study climate over long intervals, up to millions of years, direct measurements of climate variables are not possible. Instead, climate proxies, i.e. indicators of climate change, have been used to study past climate variability (Ruddiman, 2008). Many different types of proxies have been used in the literature. For example; pollen records for changes in precipitation (e.g. Brewer et al., 2008); Mg/Ca ratios as indicator for deep-water temperature (e.g. Lear et al., 2010; Elderfield et al., 2010); and sea-surface temperatures are indicated by Mg/Ca ratios, membrane lipids of plankton (named TEX_{86}) or alkanones (e.g. Schouten et al., 2002; Dekens et al., 2008; Littler et al., 2011). Furthermore, isotope ratios (e.g. $\delta^{18}O$, $\delta^{13}C$, or $\delta^{11}B$) are one of the prime past climate proxies used in paleoclimatology. Indicating changes for a wide range of different variables such as, temperature, sea-level, precipitation, ocean salinity, or CO_2 concentrations.

Isotope ratios were one of the first proxies used to study past climate change (Emiliani, 1955). Isotopes are atoms of the same chemical element, but with a different number of neutrons, and hence a different atomic mass. The number of protons is the same, since this determines the type of chemical element. For example, oxygen (O), has 8 protons in its nucleus, for which three stable oxygen isotopes exist on the Earth, which are shown in Table 1.1. Furthermore, isotopes can also occur in an unstable form, for example ^{15}O for oxygen or ^{14}C for carbon. Naturally these isotopes decay into a stable form, with a specific half-life time, for which ^{14}C is well known for its application in dating organic material.

The concentrations of stable oxygen isotopes vary among the different components of the climate system due to chemical or physical processes. For example, evaporation of water (H_2O), which falls as precipitation, favours molecules with lighter isotopes

Table 1.1 | *Occurrences of stable oxygen isotopes on the Earth (Gat et al., 2001).*

	^{16}O	^{17}O	^{18}O
natural variation (%)	99.759	0.037	0.204

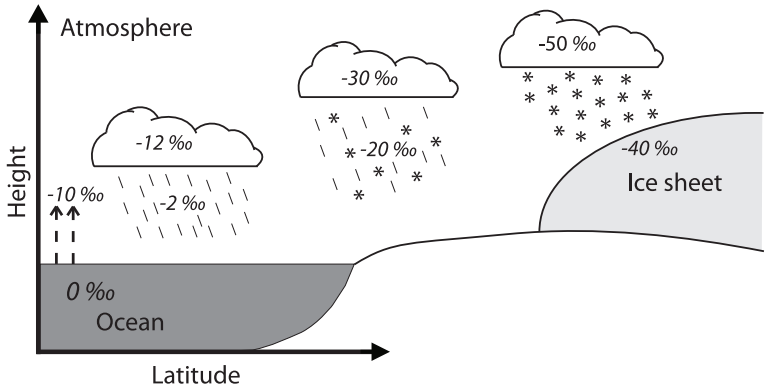

Figure 1.5 | *Rayleigh fractionation.* *The fractionation process of oxygen isotopes in water on Earth. Most water evaporates in the tropics (left), which contains relatively less heavy isotopes. Condensation, on the other hand, favours heavier molecules, following that rain contains relatively more heavy isotopes than the cloud from which it is formed. Furthermore, water is in general transported towards higher latitudes where the large ice-sheets are present (right).*

due to the slightly different physical properties of the molecules. Therefore, there is less of the heavy isotope ^{18}O in fresh water and in polar ice. Similarly, if water vapour in clouds condenses to form rain, rainwater is enriched with heavier isotopes, leading to "lighter" H_2O in the clouds. This process is illustrated in Fig. 1.5 and is called Rayleigh fractionation (e.g. Dansgaard (1964) and references therein). As is shown, precipitation contains less heavy water molecules as it falls at higher latitudes and is therefore a measure for changes in temperature.

With this distinction in mind, changes in isotope ratios can be used to deduce changes in past climate. As was already shown by Dansgaard (1964), there is a clear relation between surface-air temperatures and ^{18}O in precipitation. However, this relation is not constant through time, and is influenced by, for example, the water vapour source area, seasonal effects, and the strength of the temperature inversion (Helsen, 2006). The abundance of isotopes is in general measured as a ratio between the stable isotope and the most abundant species of the atom. In case of oxygen, ^{18}O is measured relative to ^{16}O:

$$R[^{18}O] = \frac{^{18}O}{^{16}O}. \tag{1.1}$$

Furthermore, this ratio is measured with respect to a standard ratio, which for water is the Vienna Standard Mean Ocean Water (VSMOW). Isotope ratios are calculated in parts per thousand, ‰, relative to the standard, and are called the δ^{18}O ratio:

$$\delta^{18}O = \left(\frac{R_{sample}}{R_{standard}} - 1 \right) \times 1000\,‰, \tag{1.2}$$

The PD global average of the ocean is equal to 0‰ VSMOW. During the course of the twentieth century, measuring δ^{18}O ratios from deep-sea sediment cores became well established (e.g. Emiliani, 1955; Shackleton and Kennett, 1975). Predominantly fossilised shells of foraminifera (forams) were used for measuring changes in δ^{18}O. Forams (Fig. 1.4) are small ocean-dwelling species, for which most species create a calcite ($CaCO_3$) shell that can be well fossilised. The δ^{18}O is measured from the calcite shell, with respect to the Vienna Pee Dee Belemnite (VPDB) standard. The VPDB reference value for calcite δ^{18}O ratios is related to VSMOW as: VPDB = VSMOW - 0.28‰. The calcite δ^{18}O ratio is influenced by several properties of the ocean environment. The two main components affecting the uptake of ^{18}O in the calcite shell are temperature and the δ^{18}O of the water (Chappell and Shackleton, 1986).

Although there are numerous different species, two main types of forams are distinguished. The surface dwelling planktonic species and the benthic species that live on or near the seabed. In case of planktonic forams, the δ^{18}O can also be influenced by differences in surface salinity, changes in seasonal growth and depth habitat, and is therefore not easy to interpreted (Chappell and Shackleton, 1986). On the other hand, benthic forams predominantly provide a record for local deep-water temperature and global ice volume. For the latter, ice volume changes are reflected in the δ^{18}O of seawater, for which a more in-depth discussion of this relationship is included in Section 1.5.

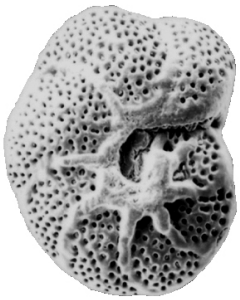

Figure 1.6 | *Benthic foraminifera.* *An example of a benthic foram shell (from UCL: http://www.ucl.ac.uk/GeolSci/micropal/foram.html).*

Within paleoclimate research oxygen isotopes are not only measured from foraminiferal shells, which can go back to 100 Myr ago. Also ice cores provide a wealth of information from both Greenland (e.g. GRIP Members, 1993) and Antarctica (e.g. Epica Community Members, 2006). Past temperatures are derived from δ^{18}O of the ice, although spanning a shorter time interval, back to 800 kyr before present. Also, δ^{18}O of the enclosed air (O_2) has been measured, relating it to changes in ice volume and the hydrological cycle (Sowers et al., 1993).

As is illustrated in Fig. 1.7, the similarity in glacial-interglacial change over the past 120 kyr is striking between the benthic deep-sea record from the East Pacific (in green; Mix et al., 1995) and the Antarctic ice-core record (in blue; Epica Community Members, 2006). On the smaller (kyr) time scale there seems to be not much coherence between these two records, mainly due to the low resolution of the benthic

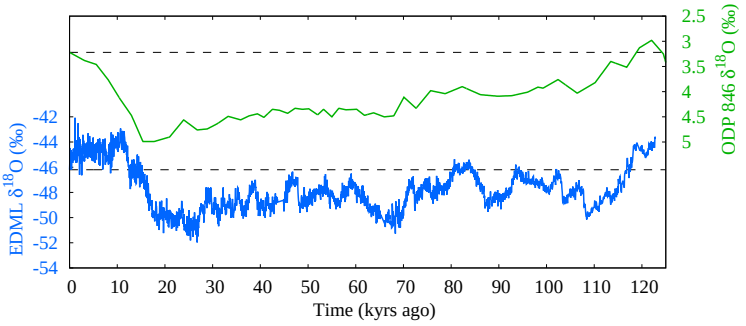

Figure 1.7 | $\delta^{18}O$ data. *In green, Ocean Drilling Program (ODP) site 846 benthic $\delta^{18}O$ data (Mix et al., 1995) and in blue, Antarctic $\delta^{18}O$ of the EPICA Dronning Maud Land (EDML) ice-core (Epica Community Members, 2006) over the past glacial cycle. Dashed lines represent the PD values, 3.22 and -46.2‰, respectively.*

deep-sea data. Also there is a clear time lag in the deep-sea record relative to the ice-core data. Nevertheless, it is clearly visible that during the glacial period (from 120 to 20 kyr ago) $\delta^{18}O$ from the ice decreases with respect to the PD value, whereas the benthic $\delta^{18}O$ increases (note that the right green y-axis has been reversed). Furthermore, the ice-core $\delta^{18}O$ is heavily depleted in ^{18}O, due to the Rayleigh fractionation explained in Fig. 1.5, while on the contrary the benthic $\delta^{18}O$ are more enriched during glacial stages.

1.5 Modelling benthic oxygen isotopes

To separate the benthic $\delta^{18}O$ data into a deep-water temperature and global ice volume signal is still one of the fundamental issues in paleoclimate research. In case of deep-water temperature, the degree of uptake of $\delta^{18}O$ in the carbonate ions (CO_3) in the shell is influenced by temperature variations (Zachos et al., 2001). From a comparison of observed deep-sea data it is shown that the relation between benthic $\delta^{18}O$ and local deep-water temperature is negative and linear (e.g. Shackleton, 1974; Duplessy et al., 2002). Although this relation is only valid for a certain range of temperatures (e.g. Duplessy et al. (2002) indicates up to 12 °C).

As is shown in Fig. 1.5, evaporation of sea water favours lighter isotopes, and therefore leading to significantly lower values of ice $\delta^{18}O$. Hence, buildup of ice volume leads to a rise in $\delta^{18}O$ of ocean water (from hereon referred to as δ_w), and therefore to an increase in benthic $\delta^{18}O$, as is illustrated in Fig. 1.7. To calculate δ_w, mass conservation between $\delta^{18}O$ of the ice and ice volume with δ_w and ocean volume is considered:

$$\delta_w V_o + \overline{\delta^{18}O_i} V_i = constant. \tag{1.3}$$

Here, V_o and V_i are respectively the ocean and ice volume (in km^3 water equivalent), δ_w the ocean-water δ^{18}O and $\overline{\delta^{18}O_i}$ the mean ice-sheet δ^{18}O (both in ‰ VSMOW). The *constant* is defined here as the PD contribution of δ^{18}O stored in the ice, scaled with ice and ocean volume. Rewriting equation (1.3) to a function of δ_w and correcting for the difference between VSMOW and VPDB yields:

$$\delta_w = -\frac{\overline{\delta^{18}O_i}V_i}{V_o} + \left[\frac{\overline{\delta^{18}O_i}V_i}{V_o}\right]_{PD} - 0.28. \tag{1.4}$$

The first term on the r.h.s. is the time-dependent variables influencing δ_w, the second term the PD reference value and the 0.28 is included to account for the difference between VSMOW and VPDB. Equation (1.4) can also be written relative to PD, equivalent to VSMOW:

$$\Delta\delta_w = -\frac{\overline{\delta^{18}O_i}V_i}{V_o} + \left[\frac{\overline{\delta^{18}O_i}V_i}{V_o}\right]_{PD}. \tag{1.5}$$

The second important contribution, the influence of deep-water temperature, is parameterised as a linear relation between temperature and δ^{18}O changes relative to PD:

$$\Delta\delta_T = \gamma\Delta T_o. \tag{1.6}$$

The value of γ is adopted from Duplessy et al. (2002), in which they showed a linear relation between benthic δ^{18}O and deep-water temperatures with a slope of $-0.28‰^{\circ}C^{-1}$. Following, the changes in benthic δ^{18}O can be computed by combining the two contributions shown in equations (1.5) and (1.6):

$$\Delta\delta^{18}O_b = -\frac{\overline{\delta^{18}O_i}V_i}{V_o} + \left[\frac{\overline{\delta^{18}O_i}V_i}{V_o}\right]_{PD} + \gamma\Delta T_o, \tag{1.7}$$

with Δ denotes values relative to PD. Finally, the volume of the ocean, V_o, is calculated with the PD depth of the ocean (D_o = 4 km) corrected for eustatic sea-level change relative to PD, ΔS. The area of the world's ocean (O_{area}) is assumed to remain constant at 3.62×10^8 km^2:

$$V_o = (D_o + \Delta S)O_{area}. \tag{1.8}$$

An example of the separate signals over the past 3 glacial cycles is shown in Fig. 1.8. During glacial periods, the benthic δ^{18}O data (in black) increases (the y-axis has been reversed). Both the temperature (blue) and ice volume (red) contribution show coherent changes with a colder climate and more ice volume.

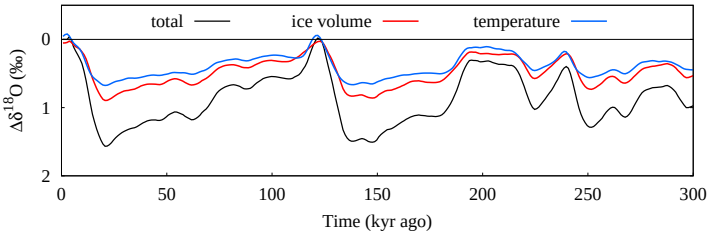

Figure 1.8 | *Reconstruction over the past 300 kyr.* *Modelling result showing the two separate contributions to the benthic $\delta^{18}O$ data (in black) over the past 300 kyr. The ice volume contribution, equation* (1.5)*, is shown in red and the deep-water temperature part, equation* (1.6)*, is shown in blue. All values are relative to PD and the y-axis is reversed with positive values below, related to a colder climate with more ice.*

1.6 Outline

The deep-sea records obtained throughout the past decades have provided the community with a wealth of knowledge on past climate changes on multiple time scales. The main aim of this research is to provide new insights into the climate data provided by deep-sea benthic δ^{18}O records over the past 40 million years, the time of major glaciation on Earth. The combined influence of global ice volume and local deep-water temperature on the benthic δ^{18}O data forms the basis of the research presented in this thesis. Both variables can provide valuable insight in past climate changes from millennial to 100-kyr time scales.

First and foremost, in Chapter 2 the modelling approach to reconstruct the two climate signals from the benthic δ^{18}O data is explained. With an inverse forward modelling approach temperature is derived from the change in benthic δ^{18}O data. In addition, a thorough description is given of the methodology involved in modelling ice sheets, for a 1-Dimensional (1-D) and a 3-D ice-sheet model. This is the main component within the modelling framework.

Next, Chapter 3 consists of the basic results obtained from 1-D ice-sheet modelling over the second half of the Cenozoic. Providing a reconstruction of temperature and sea level, calculated from ice volume, over the past 40 million years. In Chapter 3, a comparison is presented with previous modelling efforts and observed sea-level records. Furthermore, the obtained results are thoroughly analysed with several sensitivity tests. Additionally, in Chapter 4 a more comprehensive analysis is presented of the results shown in Chapter 3. Giving new insights in the transient behaviour of the Earth's climate and demonstrating the possible implications that can occur while interpreting the benthic δ^{18}O data. Finally, Chapter 5 finishes the experiments with the 1-D ice-sheet models, and presents a continuous CO_2 reconstruction over the past 20 million years. The reconstruction is based on a comparison of the reconstructed

temperature from Chapter 3 with ice-core and proxy-derived CO_2 records. This chapter shows the CO_2 proxy data in a broader framework and examines the changes in CO_2 possibly related to the initiation of NH glaciation and the MPT.

Chapter 6 combines the inverse forward modelling approach with sophisticated 3-D ice-sheet models. A simulation is performed over the past 1 million years, reconstruction ice volume on Antarctica, Greenland, Eurasia and North America. The full 3-D model approach creates the possibility to assess the complete contributions of the ice sheets to eustatic sea level and sea water $\delta^{18}O$. Finally, Chapter 7 concludes this thesis with a short summary of the main results obtained with the 1-D and 3-D models. Additionally, some possible new implementations that could be included in the 3-D modelling framework are discussed. Such as improvements in the climate physics involving interaction of the ice sheets with the ocean and the atmosphere.

2

Methodology

As has been introduced in the previous chapter, benthic δ^{18}O data are used in this thesis to reconstruct a temperature and ice-volume record over the past 40 million years. This chapter explains the methodology involved in using benthic δ^{18}O data to drive ice-sheet models. Commonly, an ice-sheet model is forced with temperature and sea-level observations. However, in the approach used in this thesis a temperature anomaly relative to present day is derived from the benthic δ^{18}O forcing, and sea level is internally calculated from ice volume. In this chapter, the inverse forward modelling approach is explained. The temperature anomaly is linearly related to the difference between modelled and observed δ^{18}O, forming the central framework of the approach. The temperature anomaly is forwarded to the ice-sheet model and a simplified deep-water temperature model to derive the two contributions to the benthic δ^{18}O record. Furthermore, two types of ice-sheet models are introduced here that are used in the consecutive chapters. Firstly, an 1-D axisymmetrical ice-sheet model, which calculates ice flow in one radial direction on an initially cone-shaped continent, is used for the 35 million year time scale. Secondly, a 3-D thermomechanical model is introduced, providing much more detail for shorter term simulations up to 1 million years.

2.1 Introduction

The work presented in this thesis builds on earlier studies with ice-sheet models, reconstructing ice volume and temperature over the past million years. Firstly, Bintanja et al. (2002) used a 3-D thermomechanical ice-sheet model to reconstruct ice volume over the past glacial cycle, forced with a separate temperature (Jouzel et al., 1993) and sea-level record (CLIMAP Project members, 1976). The 3-D ice-sheet model is largely based on a study by Van de Wal (1999a), who examined the Greenland ice sheet (GrIS). Secondly, the study of Bintanja et al. (2005b) also covered the past glacial cycle, with a focus on changes in the NH. Moreover, a new methodology was introduced at that time by forcing the ice-sheet models with sea level only. In this concept, temperature is derived using an inverse forward modelling approach, which will be explained shortly hereafter in Section 2.2. Likewise, Wilschut et al. (2006) used the same approach with a simplified 1-D ice-sheet model, investigating hysteresis between temperature and sea level for the last glacial cycle.

A first attempt to derive ice volume from benthic δ^{18}O data was performed by Oerlemans (2004b). In this study, a linear approach was used to derive Antarctic ice volume and deep-water temperatures from benthic δ^{18}O data covering the Cenozoic (Zachos et al., 2008). On shorter time scales, Bintanja et al. (2005a) and Bintanja and Van de Wal (2008) applied the inverse approach to derive ice volume and temperature from the benthic δ^{18}O stack of Lisiecki and Raymo (2005) with 3-D ice-sheet models for two NH ice sheets. The study of Bintanja et al. (2005a) focused more on the initial reconstruction, while Bintanja and Van de Wal (2008) provided a more in-depth analysis of past glacial changes of the North American ice sheet and its link to the switch from 41-kyr to 100-kyr glacial cycles, i.e. the classical problem of the MPT. The inverse approach combined with benthic δ^{18}O data as was introduced by (Bintanja et al., 2005a) serves as the basis of the modelling work presented in this thesis.

2.2 Inverse forward modelling

Throughout all following chapters, temperature and sea level are derived from benthic δ^{18}O data with an inverse forward modelling approach. The method is based on the assumption that both ice volume and deep-water temperature are strongly related to the mid-latitude-to-subpolar NH surface-air temperature. This continental mean (40° to 80°N) temperature anomaly controls the waxing and waning of the Eurasian Ice sheet (EuIS) and the North American Ice Sheet (NaIS) (Bintanja et al., 2005a). The procedure linearly relates the NH temperature to the difference between the modelled and observed benthic δ^{18}O 100 years later, the time resolution of the forcing, given by:

$$\Delta T_{NH} = \overline{\Delta T_{NH}} + c\left[\delta^{18}O(t) - \delta^{18}O_{obs}(t + 0.1kyr)\right], \tag{2.1}$$

Here, $\overline{\Delta T_{NH}}$ is the mean NH temperature anomaly over the preceding 2 kyr and c represent the temperature response to changes in the $\delta^{18}O$ record (as listed in Table 2.1). Furthermore, the modelled benthic δ^{18}O is calculated as followed, based on equation (1.7):

$$\delta^{18}O = \left[\delta^{18}O_b\right]_{PD} - \frac{\overline{\delta^{18}O_i}V_i}{V_o} + \left[\frac{\overline{\delta^{18}O_i}V_i}{V_o}\right]_{PD} + \gamma\Delta T_o. \tag{2.2}$$

The first term on the right hand side (r.h.s.) is the PD value of δ^{18}O taken from the observations. The second and third term on the r.h.s. represent the ice volume contribution (equation (1.5)). The temperature contribution is given by the last term on the r.h.s. (equation (1.6)). As a constraint, the modelled δ^{18}O data are determined by minimising the difference between modelled and observed δ^{18}O i.e. the observed δ^{18}O record must be accurately followed as is illustrated in Fig. 2.1.

Most importantly, in this way a continuous and self-consistent record on the same time scale is constructed of temperature, sea level (ice volume) and benthic δ^{18}O. One should note, however, that sea level is internally derived from ice volume alone. Other influences such as changes in mid-ocean ridge length, spreading rates, oceanic area change and sedimentation (Müller et al., 2008; Moucha et al., 2008) are not included in what is defined here as eustatic sea level change.

As is illustrated in Fig. 2.1, the calculated temperature anomaly, ΔT_{NH}, is forwarded to two model routines; (1) The ice-sheet model, which can be a set of 1-D or

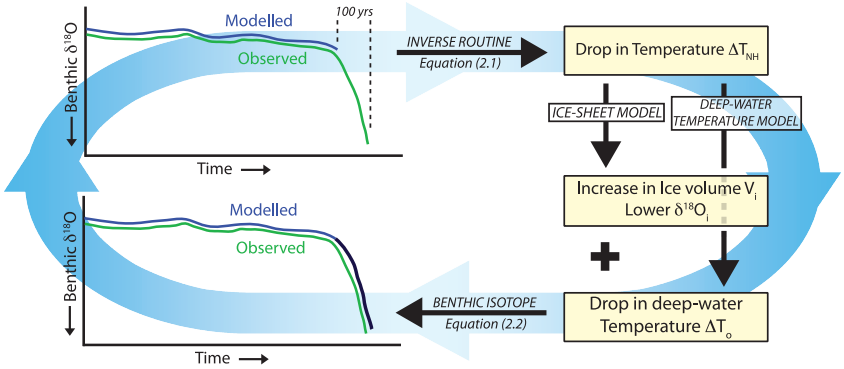

Figure 2.1 | *Inverse forward modelling scheme.* *Starting in the top left corner, every 100 years the NH continental mean surface-air temperature relative to PD ΔT_{NH} is calculated using the inverse routine, equation* (2.1)*, for which an increase in $\delta^{18}O$ leads to a drop in temperature. Next, the temperature anomaly is forwarded to the ice-sheet and deep-water temperature models, resulting in an increase in ice volume, a drop in $\delta^{18}O_i$ and a drop in the deep-water temperature anomaly ΔT_o. Finally, the benthic modelled $\delta^{18}O$ is calculated according to equation* (2.2)*, and is forwarded to the inverse routine to determine the next time step temperature anomaly.*

3-D models that will be explained in Sections 2.3 and 2.4, respectively; And (2) the deep-water to surface-air temperature coupling, for which a parameterisation used by Bintanja et al. (2005a) has been adopted, linearly relating the deep-water temperature ΔT_o to the 3-kyr mean NH temperature ΔT_{NH} (°C):

$$\Delta T_o = \lambda_{dw} \Delta T_{m-3kyr}. \tag{2.3}$$

In this way, ΔT_o can be seen as a mean deep-water temperature anomaly relative to PD, related to deep-water formation in the NH. The 3-kyr time lag can be qualitatively understood from the response timescales of the ocean with respect to the atmosphere (the former has a timescale of several kyr; the latter a few months). According to Bintanja et al. (2005a), long-term variations in deep-water and surface temperatures show sufficient coherence to justify the use of this relationship. The coupling coefficient λ_{dw} was determined using a simplified atmosphere–ocean climate model (Bintanja and Oerlemans, 1996) by correlating atmosphere to deep-water temperatures in a series of transient climate runs, leading to a value of λ_{dw} = 0.20. In Chapter 3, a more extensive analysis will be presented on the model sensitivity to this parameter.

2.3 1-D ice-sheet model

The 1-D model that is used here was first introduced by Wilschut et al. (2006). In their study one model was used to simulate NH glaciation, forcing the model with sea level observations using the inverse method equivalent to Bintanja et al. (2005b). The 1-D ice-sheet model has an axisymmetrical shape that simulates ice flow over an initially cone-shaped 'continent', i.e. with a constant negative bedrock slope in the radial direction, as is illustrated in Fig. 2.2.

2.3.1 Mass continuity and ice flow

The 1-D ice-sheet model is applied along a flow line on an equally spaced grid. The height of the ice sheet H and the bedrock elevation b (both in m) are explicitly calculated on each grid point with a time step of 1 month. The rate of change of the ice thickness is given by the continuity equation (Van der Veen, 1999; Wilschut et al., 2006):

$$\frac{\partial H}{\partial t} = \frac{1}{r}\frac{d}{dr}(rHU) + B. \tag{2.4}$$

U is the mean horizontal velocity (m s^{-1}), B is the local surface mass balance (m yr^{-1}) and r is the distance from the centre (m). The mean horizontal velocity consists of a deformation and sliding velocity. The latter results from driving stresses and is based on the shallow ice approximation (SIA), neglecting longitudinal stress and

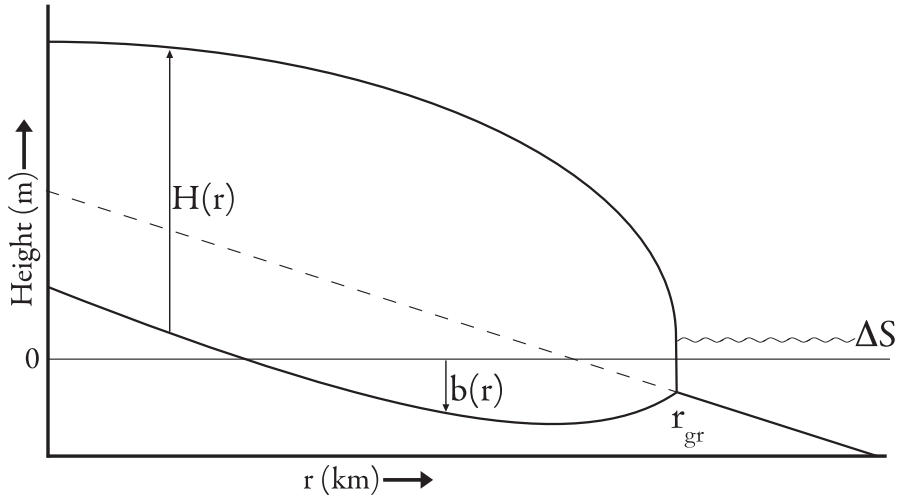

Figure 2.2 | *1-D model.* *Scheme of the 1-D ice-sheet model, with r the radial distance from the ice divide (r = 0) in kilometers, H(r) the ice thickness, b(r) the bedrock height, both in meters and measured relative to PD sea level (ΔS=0), and r_{gr} the grounding line position. The dashed line represents the initial bedrock shape, with a constant negative bedrock slope, and an initial height above sea level.*

only uses shear stress (Van den Berg et al., 2006). A Weertman-type sliding velocity representing velocities at the bed (Van der Veen, 1999):

$$U = f_d H \tau_d^n + f_s \frac{\tau_d^n}{H}. \tag{2.5}$$

Here, f_d (3.2×10^{-23} Pa^{-3} s^{-1}) is the deformation parameter, f_s (9.5×10^{-19} Pa^{-3} m^2 s^{-1}) is the sliding parameter, and $n = 3$ is the exponent in Glen's flow law. The driving stress τ_d (kg m^{-1} s^{-2}) is proportional to the ice thickness H and the slope of the ice surface according to (Van der Veen, 1999):

$$\tau_d = \rho g H \frac{dh}{dr}. \tag{2.6}$$

The mass continuity equation can be rewritten into a diffusion equation, for which the ice flux HU is written as $-D\frac{dH}{dr}$ (Van der Veen, 1999; Van den Berg et al., 2006):

$$\frac{\partial H}{\partial t} = \frac{1}{r}\frac{d}{dr}(-rD\frac{dH}{dr}) + B. \tag{2.7}$$

Here, the diffusion D is written as:

$$D = (\rho g)^3 \left(\frac{dh}{dr}\right)^2 H^3 \left[f_d H^2 + f_s\right], \tag{2.8}$$

combining equations (2.5) and (2.6). The equations are solved on the regular grid, for which the fluxes are calculated in between the ice-thickness grid points using the type II model as described in Van den Berg et al. (2006). Furthermore a slope correction is applied by using a Taylor expansion to calculate the slope (dh/dr). Therefore, points beyond the ice margin are not used and thus avoiding discontinuity (see Section 4.1.4. in Van den Berg et al., 2006).

2.3.2 Surface temperature

The NH temperature anomaly relative to PD, ΔT_{NH} as calculated with the inverse approach (equation (2.1)), is applied on each model grid and first corrected for elevation change with a lapse rate of -6.5 °C km^{-1}. In addition, a sine function is added to accommodate seasonal variability with an amplitude of 10 °C:

$$T_{ma} = \Delta T_{NH} - 0.0065 \times Hs, \tag{2.9}$$

$$T_{ms} = T_{ma} + 10 sin(\frac{\pi}{6}(m-5)). \tag{2.10}$$

T_{ma} is thus the mean annual temperature corrected for elevation, and T_{ms} is the mean seasonal temperature. Here shown in the NH case, with a minimum in February and a maximum in August. For the SH this is reversed.

2.4 3-D ice-sheet model

For a more detailed analysis of ice-sheet dynamics, a 3-D thermodynamic coupled ice sheet-ice shelf-bedrock model has been used, which solves the prognostic equations for ice thickness and temperature. The model is based on the models used by, e.g., Huybrechts (1990) and Van de Wal (1999a). The equations are solved on a 2-D grid, with a grid distance of 20 km for Greenland, and 40 km for Antarctica, Eurasia and North America. For the thermodynamics a 3-D field of velocities and temperatures are calculated over 15 grid points in the vertical, which is scaled with ice thickness and has a higher resolution at the bottom, starting with 1% and increasing to 10% at the top.

In this section, the modelling equations involved in solving mass continuity are introduced, which are related to the force balance within an ice sheet, due to stresses on and deformation of the ice. Throughout the past 30 years, the development of 3-D

ice-sheet models has evolved drastically. However, the basis still remains the same, for which most models use approximate equations of the force balance to calculate ice velocities (e.g. Huybrechts, 1990; Van de Wal, 1999a; Pollard and DeConto, 2009; Bueler and Brown, 2009). The approximations are largely based on the shallowness of a large ice body, with spatial scales far larger than the thickness of the ice. Therefore, some stresses can be neglected. Most commonly used are the Shallow Ice Approximation (SIA) (Hutter, 1983) and the Shallow Shelf Approximation (SSA) (Morland, 1987).

In this model both approximations are used, with the SIA as the basis for velocities on the ice sheet neglecting longitudinal stress, and the SSA is used for ice-shelf and sliding velocities neglecting shearing. The approach to combine both the SSA and SIA is adopted from the Parallel Ice sheet Model (PISM; Martin et al., 2011; Winkelmann et al., 2011), Although the ice-dynamical approach is quite similar to that of PISM, other model components, such as the surface mass balance and thermodynamics have not been adopted from PISM. Moreover, all velocities in this model are calculated on the regular ice-sheet grid, for which only the ice fluxes, shown in Section 2.4.4, are calculated in between grid points.

Table 2.1 | *Physical and model parameters used for the 3-D ice-sheet model.*

Constant & description		value
c	Temperature response to δ^{18}O (°C ‰$^{-1}$)	40 (1-D) / 20 (3-D)
ρ_i	ice density (kg m^{-3})	910
ρ_w	seawater density (kg m^{-3})	1028
g	gravity acceleration (m s^{-2})	9.81
n	flow exponent in Glen's flow law	3
p	power-law parameter for basal stress	0.3
β	Clausius Clapeyron gradient (K m^{-1})	8.7×10^{-4}
R	gas constant (J mol^{-1} K^{-1})	8.314
F_{ghf}	geothermal heat flux (W m^{-2})	0.0545
T_0	triple point of water (K)	273.16

2.4.1 The Shallow Ice Approximation (SIA)

In 3-D ice-sheet modelling the SIA has been used widely as the standard way to calculate ice flow for the central part of the ice sheet (e.g. Huybrechts, 1990; Van de Wal, 1999a; Bintanja et al., 2002; DeConto and Pollard, 2003a). In the case of the SIA the normal, longitudinal, stresses are neglected relative to the horizontal shear stress. In this way, shearing stresses induced by vertical changes of the horizontal velocities are only balanced by the driving stress (2-D form of equation (2.6)). This results in an integral equation for the horizontal velocities (e.g. Van de Wal, 1999a; Bueler and Brown, 2009):

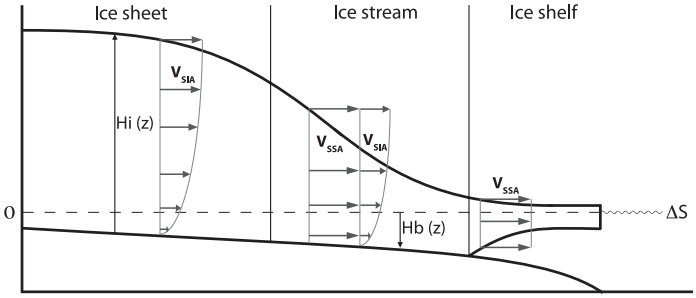

Figure 2.3 | *3-D model.* *Scheme of the 3-D ice-sheet model, illustrating the separate velocity regimes. From left to right, the shearing SIA velocities, with zero velocity at the base, dominate in the center of the ice sheet, where basal sliding is approximately zero. In the ice stream, the transition zone from sheet to shelf, basal sliding occurs and the stronger SSA velocities are added to the SIA velocities. In the ice shelf, with ice floating, shearing can be neglected and the flow is dominated by SSA type velocities. Hi, is the ice thickness, and Hb the bedrock height relative to sea level ΔS. Similar to Winkelmann et al. (2011).*

$$\vec{V}_{SIA} = -2(\rho_i g)^n |\nabla H_s|^{n-1} \nabla H_s \int_b^z A(T^*)(H_s - z)^n d\zeta. \tag{2.11}$$

Here, ∇H_s is the horizontal surface slope, ζ the scaled vertical coordinate, ρ_i the density of ice, g the gravity acceleration and n the flow exponent in Glen's flow law (shown in Table 2.1). Furthermore, A(T^*) is the temperature dependent flow-rate factor calculated with the Arrhenius relationship that accounts for a higher activation energy (Q) for ice temperatures above -10°C:

$$A(T^*) = mA_0 exp\left[\frac{-Q}{RT^*}\right] \tag{2.12}$$

With Q the activation energy for creep, m an enhancement factor (set to 4 for grounded and 1 for floating ice) and R is the gas constant (Table 2.1). T^* is the absolute temperature corrected for the dependence of the melting point on overburden pressure of the ice:

$$T^* = T + \beta H, \tag{2.13}$$

with β the Clausius Clapeyron gradient, shown in Table 2.1. The following values for A_0 and Q are used:

$$\begin{array}{llll} T^* < 263.15K & A_0 = 1.14 \times 10^{-5} Pa^{-3} yr^{-1} & Q = 60 kJmol^{-1}, \\ T^* \geq 263.15K & A_0 = 5.47 \times 10^{10} Pa^{-3} yr^{-1} & Q = 139 kJmol^{-1}. \end{array} \tag{2.14}$$

Equation (2.11) is easily solved on the regular ice-sheet grid by integration with the bottom boundary set to zero, resulting in depth dependent velocities, as illustrated in Fig. 2.3.

2.4.2 The Shallow Shelf Approximation (SSA)

In case of the SSA, longitudinal stresses are important and are dominant over the shear stresses. This results in stretching, i.e. the change of the horizontal velocities in the horizontal plane, which are independent of depth. These forces can be neglected in the interior of the ice sheet, but are important for the transition zone, i.e. ice streams, and the floating ice shelves (see Fig. 2.3). The SSA has been widely used to determine velocities in ice shelves (e.g. Huybrechts, 1990; Bueler and Brown, 2009), for which basal friction and shearing are practically zero. The stretching equations used are given by (Pollard and DeConto, 2007; Bueler and Brown, 2009):

$$\frac{\partial}{\partial x}\left[2\mu H_i\left(2\frac{\partial u}{\partial x}+\frac{\partial v}{\partial y}\right)\right]+\frac{\partial}{\partial y}\left[\mu H_i\left(\frac{\partial u}{\partial y}+\frac{\partial v}{\partial x}\right)\right]+\tau_{b,x}=\rho g H_i\frac{\partial H_s}{\partial x}, \quad (2.15)$$

$$\frac{\partial}{\partial y}\left[2\mu H_i\left(2\frac{\partial v}{\partial y}+\frac{\partial u}{\partial x}\right)\right]+\frac{\partial}{\partial x}\left[\mu H_i\left(\frac{\partial v}{\partial x}+\frac{\partial u}{\partial y}\right)\right]+\tau_{b,y}=\rho g H_i\frac{\partial H_s}{\partial y}. \quad (2.16)$$

Here, u and v are the SSA velocities in the x and y direction, respectively. In this equation, the deformational stresses due to stretching are balanced by the gravitational driving stress (with H_s the surface elevation; $H_s=(1-\rho_i/\rho_w)H_i$ for shelves) and the basal stresses $\tau_{b,x}$ and $\tau_{b,y}$. These are calculated according to Winkelmann et al. (2011) depending on the basal velocities and the yield stress for saturated till, as will be shown in Section 2.4.3. The parameter μ is the vertical averaged viscosity, a function of the strain rates:

$$\mu=\frac{1}{2\overline{A}^{1/n}}\left[\left(\frac{\partial u}{\partial x}\right)^2+\left(\frac{\partial v}{\partial y}\right)^2+\left(\frac{\partial u}{\partial x}\right)\left(\frac{\partial v}{\partial y}\right)+\frac{1}{4}\left(\frac{\partial u}{\partial y}+\frac{\partial v}{\partial x}\right)^2\right]^{\frac{1-n}{2n}}, \quad (2.17)$$

with $\overline{A}$ the vertical mean flow rate factor $A(T^*)$ from equation (2.12). Equations (2.15) and (2.16) are non-linear equations both depending on U_{SIA} and V_{SIA}. Therefore, they are solved on the regular ice-sheet grid for both horizontal velocities U_{SIA} and V_{SIA} through an iterative process. Before the iteration starts, velocities from the previous iteration are used to initialise the viscosity μ, equation (2.17) (e.g. Pollard and DeConto, 2007; Bueler and Brown, 2009).

2.4.3 Basal Stress Conditions

The basal stresses are calculated according to a power law function of the basal sliding velocity (e.g. Gladstone et al., 2010; Schoof, 2010), which relates the basal stress to the basal velocities as:

$$\tau_b = C'|v|^{m'-1}\vec{v}. \tag{2.18}$$

With C' and m' the inverse basal sliding coefficient and parameter, respectively (see also the Suppl. Inf. of Pollard and DeConto, 2009). Most commonly, the basal velocities are calculated according to a Weertman type sliding law (Weertman, 1957), calculating the sliding velocities at the base as function of the driving stress. A similar approach is used in the 1-D model, equation (2.5) with a constant value for the sliding coefficient C'. In the 3-D model the PISM approach is applied by determining the basal stress as function of a till stress and the basal sliding velocity (e.g. Bueler and Brown, 2009, PISM online User's Manual: www.pism-docs.org):

$$\tau_b = \tau_c \frac{|V_{SSA}|^{p-1}}{u_{threshold}^{p}} \vec{V}_{SSA}. \tag{2.19}$$

The plastic parameter is set to $p = 0.3$ (Table 2.1), and $u_{threshold}$ is a scaling velocity set to 100 m s^{-1}. The yield stress τ_c (in Pa) for saturated till is given by:

$$\tau_c = tan(\phi)(\rho g H_i - p_w), \tag{2.20}$$

which is actually only a yield stress in the case of a perfect-plastic basal model for p=0. The pore water pressure calculated as: $p_w = \lambda 0.96 \rho_i g H_i$. A scaling function of bedrock elevation relative to sea level is used to change the water content below the ice: λ is 1 below sea level, i.e. full water content, and scaled down to 0 for bedrock 1000 meters above sea level (Martin et al., 2011). The parameter ϕ is the till-friction angle (Clarke, 2005), which defines the strength of the till. In this model, the friction angle is a function of bedrock elevation, similar to the approach of Martin et al. (2011):

$$\phi = \begin{cases} 5^\circ & H_b \leq -1000 \\ 5^\circ + 15^\circ \left(1 + \frac{Hb}{1000}\right) & -1000 < H_b < 0 \\ 20^\circ & 0 \leq H_b \end{cases} \tag{2.21}$$

Although this parameterisations can be subject to change, the choice of ϕ and the pore water pressure p_w result in a higher yield stress τ_c for lower parts of the continents, e.g. West Antarctica, and thus a higher τ_b and eventually higher velocities.

2.4.4 Mass continuity in 2-D

Similar to the 1-D model, the mass continuity equation is written as (Van der Veen, 1999):

$$\frac{\partial H_i}{\partial t} = -\nabla \cdot (\vec{\overline{V}} H_i) + B, \tag{2.22}$$

with H_i the ice thickness (in m), $\vec{\overline{V}}$ the depth-averaged 2-D horizontal velocity vector (m yr^{-1}) and B the mass balance. The mass balance consists of the surface mass balance and sub-shelf melt or refreezing. The equation is explicitly solved through a series of steps. Firstly, the flow on land (SIA velocities) can be regarded as diffusive. Therefore, the ice flux in equation (2.22) can be divided in a diffusive (SIA) and SSA part as:

$$\vec{\overline{V}} H_i = Q = -D \cdot \vec{\nabla} H_s + \vec{V}_{SSA} H_i. \tag{2.23}$$

With the diffusivity D the scalar part from equation (2.11) and defined as $D \cdot \vec{\nabla} H_s = \vec{V}_{SIA} H_i$. The velocities are calculated on the regular grid. Following, the ice fluxes are calculated in between grid points A and B using a centered difference discretisation:

$$Q = \frac{(D_A + D_B)}{2} \frac{(HsB - HsA)}{\Delta x} + \frac{V_A + V_B}{2} H_i. \tag{2.24}$$

In the SSA term, H_i is chosen to be H_{iA} if the averaged SSA velocity between A and B is positive and H_{iB} if negative. For each grid point, four fluxes are calculated to the directly adjacent grid points, which can only be negative, i.e. outgoing, fluxes. Secondly, two tests are performed in order to prevent a negative ice thickness, and keeping mass conserved. First, the (negative) mass balance is adjusted if it exceeds the available ice thickness. If this is the case, the mass balance is taken to be 100% of the available ice thickness for this time step and the four outgoing fluxes are set to zero. Secondly, the outgoing fluxes are adjusted if their combined advective flux exceeds the available ice volume plus the mass balance (either negative or positive). If the advective flux is too large, the available ice volume is scaled and equally divided over the four outgoing fluxes. Lastly, the total advective flux and mass balance are used to determine the total mass change for the grid point, and the outgoing fluxes are applied to the four surrounding grid points as additional mass.

2.4.5 Thermodynamics

The temperature distribution throughout the ice is calculated in 3-D, which follows from the conservation of energy (Van de Wal, 1999a):

$$\frac{\partial T_i}{\partial t} = \frac{k_i}{\rho_i c_p} \nabla^2 T_i - \vec{V} \cdot \nabla T_i + \frac{\Phi}{\rho_i c_p}. \tag{2.25}$$

In this equation, the first term on the r.h.s. represents heat diffusion, depending on the thermal diffusivity k_i, ice density ρ_i (shown in Table 2.1) and the specific heat capacity of ice c_p. The second term represents advection of heat and the last term is deformational heating, with Φ the internal heating rate, due to the deformation of ice and stresses acting on the ice. Both the thermal diffusivity and the specific heat capacity are depended on the ice temperature as in Huybrechts (1992):

$$k_i(T_i) = 3.101 \times 10^8 \, e^{-0.0057(T_i+T_0)}, \quad (2.26)$$

$$c_p(T_i) = 2115.3 + 7.79293 T_i, \quad (2.27)$$

with the temperature of ice in °C. To solve the 3-D equation (2.25) for temperature, a surface boundary condition is applied using the surface-air temperature with a maximum value of T_0. The bottom boundary condition incorporates frictional heating due to sliding (Huybrechts, 1992) and a geothermal heat flux with a constant value as listed in Table 2.1.

Table 2.2 | *Mapping parameters for the four ice sheets, see Reerink et al. (2010) for details on the mapping procedure. the angle α_s defines the standard parallel, i.e. the latitude for which the projection is true to scale (see also Snyder, 1987).*

Parameter	Description	EuIS	NaIS	GrIS	AIS
ϕ_M	Latitude of center of projection (°N)	75	62	72	-90
λ_M	Longitude of center of projection (°E)	75	250	320	0
α_s	angle defining the standard parallel	25.1	23.8	7.5	19

2.4.6 Initial conditions

Initial bedrock height and ice thickness for Antarctica are taken from the ALBMAP dataset (Le Brocq et al., 2010), which includes improvements on earlier versions of BEDMAP, commonly used for the initial Antarctic ice-sheet. In case of Greenland, BEDMAP (Bamber and Layberry, 2001) was used for the initial bedrock height and ice thickness fields. For Eurasia and North America, a very high resolution PD topography dataset (Becker et al., 2009) was used, from which a 1-minute average topography is extracted, i.e. 1/60th of a degree resolution. Since the grid distance of the ice-sheet models used here is 40 km, a lower resolution of 12-minutes, 1/5th of a degree, ca. 20 km, has been used to interpolate the data on the ice-sheet grid with OBLIMAP (Reerink et al., 2010).

For the initial climate forcing of the 3-D model, PD meteorological conditions have been used for all ice sheets. Precipitation (in m w. e. yr^{-1}), 2-meter surface-air temperature (°C), and 850 hPa wind fields (in m s^{-1}) have been interpolated on the rectangular ice-sheet grid. For the interpolation an oblique stereographic projection is

applied with OBLIMAP (Reerink et al., 2010), for which specific projection parameters are shown in Table 2.2. All initial climate fields used here are taken from ERA-40 Re-analysis dataset, averaging the monthly fields from 1971 to 2000 (Uppala et al., 2005). Temperature is used as forcing to the mass balance model, as will be thoroughly explained in Chapter 6, using the 2-meter surface-air temperature. Moreover, the surface temperature is used as an upper boundary condition for the ice temperatures that have a maximum value of the melt temperature, T_0 (see Table 2.1).

3

Cenozoic global ice volume and temperature simulations

Variations in global ice volume and temperature over the Cenozoic era have been investigated with a set of 1-D ice-sheet models. Simulations include three ice sheets representing glaciation in the Northern Hemisphere, i.e. in Eurasia, North America and Greenland, and two separate ice sheets for Antarctic glaciation. The continental mean Northern Hemisphere surface-air temperature has been derived through an inverse procedure from observed benthic δ^{18}O records. These data have yielded a mutually consistent and continuous record of temperature, global ice volume and benthic δ^{18}O over the past 35 million years. The simple 1-D model shows good agreement with a comprehensive 3-D ice-sheet model for the past 3 million years. On average, differences are only 1.0 °C for temperature and 6.2 m for sea level. Most notably, over the past 35 million years, the reconstructed ice volume–temperature sensitivity shows a transition from a climate controlled by Southern Hemisphere ice sheets to one controlled by Northern Hemisphere ice sheets. Although the transient behaviour is important, equilibrium experiments show that the relationship between temperature and sea level is linear and symmetric, providing limited evidence for hysteresis. Furthermore, the results show a good comparison with other simulations of Antarctic ice volume and observed sea level.

This chapter is based on:
De Boer, B., R. S. W. van de Wal, R. Bintanja, L. J. Lourens and E. Tuenter, Cenozoic global ice volume and temperature simulations with 1-D ice-sheet models forced by marine $\delta^{18}O$ records, *Annals of Glaciology*, **51 (55)**, 23-33, 2010.

3.1 Introduction

The history of the Earth over the past 65 million years (Myr; the Cenozoic) is characterised by a general cooling trend from a 'greenhouse' to an 'icehouse' world (Lear et al., 2000). The variability in climate has increased considerably over time from a world with little continental ice prior to ∼34 Myr ago to an ice-dominated climate after this transition (e.g. Liu et al., 2009). This variability is strongly reflected in benthic deep-sea sediment records (Zachos et al., 2001), which serve as a proxy for global ice volume and local deep-water temperature (e.g. Chappell and Shackleton, 1986; Bintanja et al., 2005a).

In this chapter, both sea level and temperature over the second half of the Cenozoic era have been investigated with the axisymmetrical 1-D ice-sheet model (Wilschut et al., 2006) simulating glaciation with five hypothetical ice sheets. On the NH, two continental ice sheets represent glaciation on the Eurasian and North American continents, respectively the EuIS and NaIS, and another ice sheet simulates the Greenland ice sheet (GrIS). Antarctic glaciation has been simulated with two separate ice sheets. This separation was included to create a more climate-sensitive West Antarctic ice sheet (WAIS), i.e. to make it more responsive to temperature and sea-level fluctuations than the East Antarctic ice sheet (EAIS). In this way the obtained sea-level reconstruction has been derived from ice-volume fluctuations representative of all significant continental ice sheets that existed during the past 35 Myr. Furthermore, key processes for simulating ice-sheet evolution have been included in the model such as the feedback mechanisms between mass balance and albedo and between surface height and surface mass balance, as well as adjustment for the underlying bedrock.

3.2 Model formulation

The model used for all five ice sheets has been thoroughly explained in Section 2.3, a short summary is presented here of the most important model characteristics and parameterisations used in this chapter. The model is an axisymmetrical 1-D ice-sheet model that simulates ice flow over an initially cone-shaped 'continent', i.e. with a constant negative bedrock slope in the radial direction (values and constants are listed in Tables 3.1 and 3.2, respectively). The inverse method, Section 2.2 has been used to derive the continental mean NH temperature, using stacked benthic δ^{18}O records as forcing (Lisiecki and Raymo, 2005; Zachos et al., 2008). The derived NH temperature was used to run the ice-sheet model in forward mode over 100 years. The temperature anomaly derived from the inverse approach, Equation (2.1), is used in two procedures: the ice-sheet model and the evaluation of the deep-water temperature anomaly ΔT_o. Within the ice-sheet model, the isotopic content and ice volume are calculated with a time-step of 1 month and are forwarded to the ocean isotope module.

Table 3.1 | *Model parameters for the five ice sheets.*

Parameter	Description	EuIS	NaIS	GrIS	EAIS	WAIS
H_{bc}	Central height of the bed (m)	1250	1400	800	1450	400
$\mathrm{d}b/\mathrm{d}x$	Bedrock slope	0.0016	0.0017	0.0014	0.001	0.0011
P_0	Uncorrected precipitation (m a^{-1})	1.0	1.3	1.1	0.6	1.0
R_c	Critical radius (km)	1700	2200	700	2000	700
β_T	Isotopic sensitivity (‰ $^{\circ}\mathrm{C}^{-1}$)	0.35	0.35	0.35	0.6	0.8
β_Z	Isotopic lapse rate (‰ km^{-1})	–6.2	–6.2	–6.2	–11.2	–11.2
N_{grid}	Number of grid points	100	100	100	120	100
Δl	Grid size (km)	25	25	15	20	15
δT_{NH}	Temp. difference from NH ($^{\circ}$C)			–4	–10	–6
PD ΔS	PD ice volume (m s.e.)			7	56	7
PD $\delta^{18}\mathrm{O_i}$	PD ice-sheet isotopic content (‰)			–36	–55	–42

The inverse method is based on the fact that the two dominant contributions to the benthic δ^{18}O signal, i.e. ice volume and deep-water temperature, are closely related to the mid-latitude-to-subpolar NH temperature, which controls the waxing and waning of the EuIS and NaIS (Bintanja et al., 2005a). The derived surface-air temperature anomaly ΔT_{NH} is therefore representative of both continents and can be directly applied to the ice-sheet models for the EuIS and NaIS. To apply the temperature anomaly ΔT_{NH} to the Antarctic and Greenland ice sheets, however, a temperature difference from EuIS/NaIS needs to be derived. This temperature difference between the continents can be interpreted as a combination of two components: the different geographical location (i.e. a higher latitude leads to lower temperatures) and the presence of an ice sheet which lowers temperatures through feedbacks to the local climate.

The differences for the PD climate were determined by calculating the continental mean temperatures from the Climate Prediction Center dataset (1948–2008; Fan and van den Dool, 2008) for Antarctica and from the Climate Research Unit TS3 0.5° dataset (1901–2006; Brohan et al., 2006) elsewhere. Temperatures were reduced to sea level using the PRISM (Parameter elevation Regressions on Independent Slopes Model) dataset (Edwards, 1992) with a lapse rate of 6.5 $^{\circ}$C km^{-1}, equivalent to the lapse rate used in the models.

The geographically induced differences from the NH continental mean temperature, δT_{NH}, can be directly applied to the surface temperature calculated from the inverse routine ΔT_{NH} and are listed in Table 3.1. The choice of δT_{NH} is a subject for discussion, and the sensitivity of the model to different values of δT_{NH} is tested in section 3.4. For both the EAIS and GrIS, however, δT_{NH} has been used to tune the volume changes to a strong volume increase of the EAIS around the Eocene–Oligocene boundary (DeConto and Pollard, 2003b) and to a simultaneous initiation of the GrIS with the EuIS and NaIS, respectively. For the latter, the initiation of NH glaciation (and especially initiation of the GrIS) is still under discussion (e.g. Bartoli

Table 3.2 | *Constants used in the model, values are adopted from Wilschut et al. (2006).*

Constant	Description	Value
T_b	Relaxation time of asthenosphere (kyr)	3
k	Density ratio of ice and bedrock	3
ρ_w	Density of water (kg m^{-3})	1000
ρ_i	Density of ice (kg m^{-3})	910
α_g	Albedo of bare soil	0.2
α_{sn}	Albedo of snow	0.8
α_{ice}	Albedo of glacier ice	0.45

et al., 2005), but most evidence points to an initiation around 3 Myr ago (e.g. Whitman and Berger, 1992; Sato and Kameo, 1996).

The feedback mechanism between ice sheet and climate is less straightforward and has been tested as a parameterisation dependent upon the ice-sheet radius. The model outcome including this parameterisation, however, did not show any large differences from the original results. An additional correction to temperature is therefore excluded, in order to keep the interpretation of sea-level and temperature variations as transparent as possible.

3.2.1 Including δ^{18}O in ice-sheet models

The calculation of the benthic δ^{18}O ratio has already been introduced in Section 2.2, showing a combined equation for the ice-sheet and deep-water temperature contributions to variations in benthic δ^{18}O:

$$\delta^{18}O = \left[\delta^{18}O_b\right]_{PD} - \frac{\overline{\delta^{18}O_i}V_i}{V_o} + \left[\frac{\overline{\delta^{18}O_i}V_i}{V_o}\right]_{PD} + \gamma\Delta T_o. \tag{3.1}$$

Here, the ice-sheet model part is represented by the second term on the r.h..s., for which ice volume, V_i is calculated directly from the ice thickness calculations, V_o is the ocean volume calculated as in equation (1.8), and $\overline{\delta^{18}O_i}$ is the mean oxygen isotope content of the ice sheets (‰). The third term on the r.h.s. represents the PD values of equivalent sea level (adopted from Bintanja et al., 2002) and $\overline{\delta^{18}O_i}$ (from Lhomme and Clarke, 2005), which are listed in Table 3.1. For the isotope content of the ice sheet, $\delta^{18}O_i$, the formulation introduced by Cuffey (2000) is used:

$$\delta^{18}O_i = \delta^{18}O_{PD} + \beta_T\Delta T + \beta_Z\Delta Z, \tag{3.2}$$

where $\delta^{18}O_{PD}$ (‰) is the PD distribution over the ice sheet as a function of the mean annual temperature, corrected for surface elevation T_{ma} (°C) as described by equation (2.9).

For the GrIS the relation derived by Zwally and Giovinetto (1997) was adopted:

$$\delta^{18}O_{PD} = 0.691T_{ma} - 13.43, \tag{3.3}$$

which is also applied to the EuIS and NaIS. Although the isotopic depletion of the EuIS and NaIS cannot be constrained, the $\delta^{18}O_i$ will most probably be close to (but slightly higher than) that of the GrIS (see Duplessy et al., 2002). This difference, however, is included due to the applied temperature difference δT_{NH} between Greenland and the NH ice sheets. For the EAIS and WAIS, a different equation was used, adopted from a similar study for Antarctica (Giovinetto and Zwally, 1997):

$$\delta^{18}O_{PD} = 0.852T_{ma} - 6.78. \tag{3.4}$$

The additional terms in equation (3.2) relate $\delta^{18}O_i$ to changes in temperature (°C) and surface elevation (km) with respect to PD. Values for the isotopic parameters β_T and β_Z are listed in Table 3.1 and selected within the range presented by Lhomme and Clarke (2005).

The last term on the r.h.s. of equation (3.1) represents the contribution of the ocean deep-water temperature ΔT_o (°C), with $\gamma = -0.28‰°C^{-1}$ (Duplessy et al., 2002). As has been introduced in Section 2.2, the deep-water temperature is linearly related to the 3-kyr mean NH temperature ΔT_{NH}:

$$\Delta T_o = \lambda_{dw} \Delta T_{m-3kyr}. \tag{3.5}$$

The coupling coefficient λ_{dw} was determined using a simplified atmosphere–ocean climate model (Bintanja and Oerlemans, 1996) by correlating atmosphere to deep-water temperatures in a series of transient climate runs. In Bintanja et al. (2005a), $\lambda_{dw} = 0.20$ (denoted by α in the supplementary information of Bintanja and Van de Wal (2008)). This value is also adopted for the NH-only experiment. In contrast, for the full model a slightly lower value of $\lambda_{dw} = 0.15$ was used. This resulted in a lower reconstructed sea level during the Pleistocene with respect to the latter value, and better agreement with observed sea-level variations. A more thorough discussion of model sensitivity to this parameter is included in Section 3.3.4.

3.2.2 Bedrock adjustment

The adjustment of the bedrock to the ice load is based on the principle of local isostatic equilibrium (Van der Veen, 1999) and is given by:

$$\frac{db}{dt} = -\frac{1}{T_b}\left(\frac{H}{k} + b - b_0\right), \tag{3.6}$$

where T_b is the relaxation time of the asthenosphere in years and k is the ratio of the density of ice and the underlying bedrock material, listed in Table 3.2. The initial state of the bedrock is given by $b_0 = H_{bc} - (db/dx)x$, where H_{bc} is the central bedrock height (m) and db/dx the slope of the bedrock, as listed in Table 3.1.

The choice of these parameters is critical for the model results; changing the bedrock slope has a significant impact on both temperature and sea level. As a tuning target in the model, these two parameters were chosen such that the simulated NH ice volume at the Last Glacial Maximum (LGM, around 20 kyr ago) is close to the generally established sea-level drop of 120 ± 10m (e.g. Rohling et al., 2009). For the Antarctic and Greenland ice sheets, the values were chosen such that ice volume (m s.e.) at PD is close to the PD value shown in Table 3.1.

3.2.3 Mass balance

The mass-balance parameterisation is an important aspect of an ice-sheet model and serves as the coupling between temperature and ice volume. Both mass-balance components (accumulation and ablation) are calculated explicitly for each grid point. The ablation rate A (m yr^{-1}) is a function of temperature and solar insolation, and is based on PD mass-balance observations and modelling results for Antarctica and Greenland (Bintanja et al., 2002):

$$A = \left[4T_{ms} + 0.513(1-\alpha)Q + C_{abl}\right]/100, \tag{3.7}$$

where Q is the monthly mean incoming shortwave radiation at the top of the atmosphere (W m^{-2}) which varies over time (Laskar et al., 2004). For each ice sheet, a different latitude was used to calculate the monthly mean values: 65°N for the NaIS and EuIS; 70°N for GrIS; and 80°S for EAIS and WAIS. The constant C_{abl} indicates a certain threshold value for ablation to begin, depending on temperature and insolation. For the two NH ice sheets, $C_{abl} = -28$. This balances the PD yearly mean insolation, requiring ablation to be non-zero for temperatures above freezing.

Values for Greenland and Antarctica were based on their PD temperature differences as discussed in Section 3.2, resulting in $C_{abl} = -48, -76$ and -90 for the GrIS, WAIS and EAIS, respectively. Although these are slightly different from the values determined by Bintanja et al. (2002), they have been selected for as much consistency as possible in the model. The temperature T_{ms} (°C) is the mean surface-air temperature corrected for height with a lapse rate of -6.5 °C km^{-1}, and for seasonality by a superimposed sine function, as given by equation (2.10). The surface albedo α is defined:

$$\alpha = \max\left[\alpha_g, \alpha_{sn} - (\alpha_{sn} - \alpha_{su})e^{-15d} - 0.015A\right], \tag{3.8}$$

where α_g, α_{sn} and α_{su} are the soil, snow and surface (soil or ice) albedo, respectively (listed in Table 3.2), d is the snow depth (m) and A is the ablation rate at the previous time-step, calculated from equation (3.7). The e-folding term represents the effect of snow thickness and patchiness on the albedo, with the snow depth determined within the model as a function of the cumulative mass balance (Bintanja et al., 2005b).

Accumulation is determined using temperature and ice-sheet extent. Firstly, temperature influences the moisture content of the atmosphere, i.e. higher temperatures lead to higher humidity and thus relatively more precipitation. This relation is taken into account by means of an exponential dependence on temperature T_{ms} (°C), based on the Clausius–Clapeyron relation. Secondly, a bigger ice sheet prohibits the deposition of snow on the ice sheet. This is taken into account by relating the precipitation to an e-folding critical radius (Oerlemans, 2004a), approximately the maximum extent of the ice sheet:

$$P = P_0 \mathrm{e}^{0.04 T_{ms} - R/R_c}, \tag{3.9}$$

where P_0 (m yr^{-1}) is the uncorrected precipitation constant, R is the radius of the ice sheet and R_c the critical radius (km) (Table 3.1).

Finally, monthly snow accumulation is obtained as a temperature-dependent fraction of precipitation (Bintanja et al., 2002). The values of P_0 represent ice-sheet climate sensitivity, based on PD observational data, and are chosen such that: (1) the NH is wetter than Antarctica; (2) the WAIS is more sensitive than the EAIS; and (3) the NaIS is more sensitive than the EuIS.

3.3 Results

3.3.1 Validation for the Northern Hemisphere

Firstly, to support the 35 Myr simulations presented below, the outcome of the simplified 1-D ice-sheet model was compared to previous simulations conducted using a comprehensive 3-D ice-sheet model (Bintanja and Van de Wal, 2008). Similar to the 3-D model experiment, simulations were performed over the past 4 Myr with the EuIS and NaIS only, forced with the LR04 global stack of 57 benthic δ^{18}O records (Lisiecki and Raymo, 2005), linearly interpolated to a 100 year resolution. Moreover, it is assumed that the NH ice sheets contributed to 85% of global eustatic sea level and 95% of benthic isotope variations, in agreement with the assumptions made by Bintanja et al. (2005a). These two corrections were applied to equations (1.8) and (3.1), respectively.

Over the past 3 Myr, the results for NH glaciation simulations with the 1-D model are similar to the 3-D model results (Bintanja and Van de Wal, 2008), as can be seen in Fig. 3.1. On average, the absolute differences are 1.0 °C for NH temperature and 6.2 m for sea level. The difference (root-mean-square) between modelled and observed

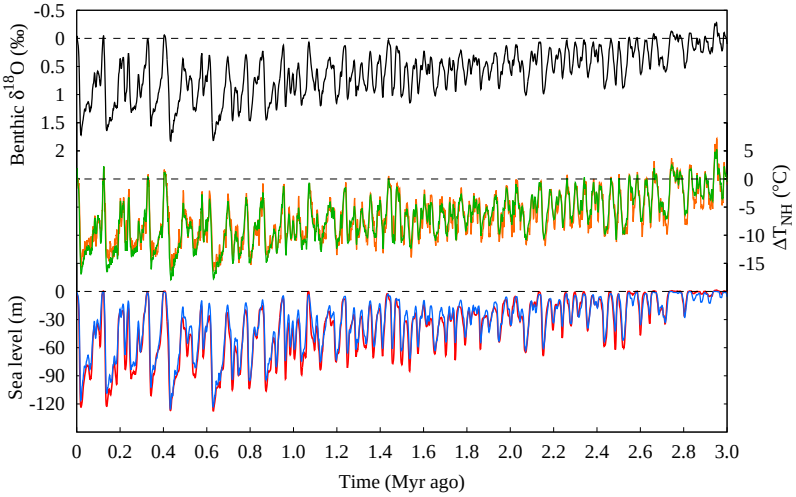

Figure 3.1 | *Reconstructions over the past 3 Myr.* *From top to bottom, the LR04 (Lisiecki and Raymo, 2005) global stack of benthic $\delta^{18}O$ in black; 1-D model reconstructed NH temperature in green; and global sea level in blue. The 3-D model results (Bintanja and Van de Wal, 2008) are shown in orange for temperature and in red for sea level. All values are relative to PD.*

benthic δ^{18}O is very small and less than 0.005‰. Furthermore, the orbital frequencies present in the benthic isotope signal (see Lisiecki and Raymo, 2007) are reproduced by temperature and ice volume. This is illustrated for temperature in Fig. 3.2, which clearly shows the shift from the 41-kyr world to the 100-kyr glacial cycles of the late Pleistocene. Generally, temperatures in the 1-D model are higher than in the 3-D model. The timing of maxima and minima agrees well with the 3-D model, also supported by the similarity of the power spectra (not shown). Sea-level differences are relatively smaller, although ice-sheet growth is initiated at a few degrees above PD. This is in contrast to the 3-D model (Bintanja and Van de Wal, 2008), for which a threshold of -5 °C was observed. As was already pointed out by Wilschut et al. (2006), the simplified geometry of the 1-D model is the major cause of the dissimilarities between the two models.

3.3.2 A 35 Myr record of sea level and temperature

For the complete simulation including ice sheets in both hemispheres the updated composite benthic δ^{18}O dataset of Zachos et al. (2008) was used, shown in Fig. 3.3a, smoothed over six data points and linearly interpolated to 100 year resolution with a 5 kyr running mean. As can be seen in Fig. 3.3b and c showing reconstructed temperature (green) and sea level (blue), respectively, both variables closely follow the pattern of the δ^{18}O record as for the NH-only experiment presented in Section 3.3.1.

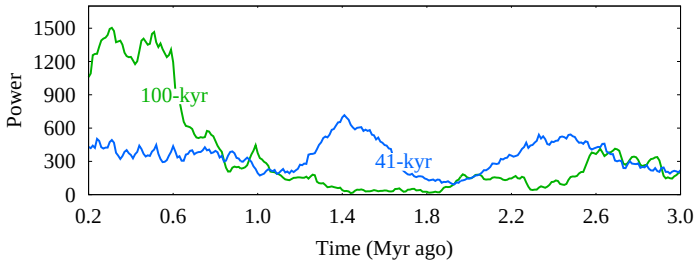

Figure 3.2 | *Power of NH temperature* *Change of the 100-kyr (green) and 41-kyr (blue) frequency power of reconstructed NH temperature over the past 3 Myr. A Blackman–Tukey spectral analysis with a Parzen window was applied, with 95% confidence limits and 3600 lags (90% of the data) to a moving window of 400 kyr shifting with 10 kyr (361 data points in total). Analysis was conducted using the AnalySeries program (version 2.0.3; Paillard et al., 1996).*

The lower part of Fig. 3.3c shows the average standard deviation (a measure of variability) of NH and Antarctic ice-volume change (in m s.e.) over 400-kyr periods. Clearly visible is the strong increase of NH glacial variability beginning at around 5 Myr ago, illustrating the waxing and waning of the EuIS and NaIS in the Pleistocene.

Summarised in Table 3.3 are the tuning targets (or model constraints) for the model simulations which are all met. Sea level at the LGM, however, is around 100 m below PD due to a lower amplitude in the Zachos et al. (2008) record compared to the LR04 forcing (Lisiecki and Raymo, 2005). For the NH-only experiment, constraint 3 in Table 3.3 is therefore satisfied. Furthermore, the difference between modelled and observed δ^{18}O remains within 0.005‰. Other prominent features in the history of the Antarctic ice sheet, such as the short drop in sea level around the Oligocene–Miocene boundary (Mi-1; ∼23 Myr ago) and the increase in ice volume in the mid- to late Miocene (15–10 Myr ago) (Zachos et al., 2001) are well reconstructed by the model.

The two separate signals of the δ^{18}O record are shown in Fig. 3.4 illustrating the large variability in contributions of deep-water temperature and ice volume to the total δ^{18}O signal. Although the variability is large, some distinct features can be recognised. Firstly, ice volume is the dominant signal during the Oligocene and the early to mid-Miocene, contributing to about 60% of changes in benthic δ^{18}O.

Table 3.3 | *Tuning targets for the full Cenozoic simulations.*

Tuning target		Source
1	PD ice volume of GrIS, EAIS and WAIS	Bintanja et al. (2002)
2	LGM ice volume of ∼120 m s.e.	Rohling et al. (2009)
3	Oi-1 increase of EAIS of ∼40 m s.e	DeConto and Pollard (2003b)

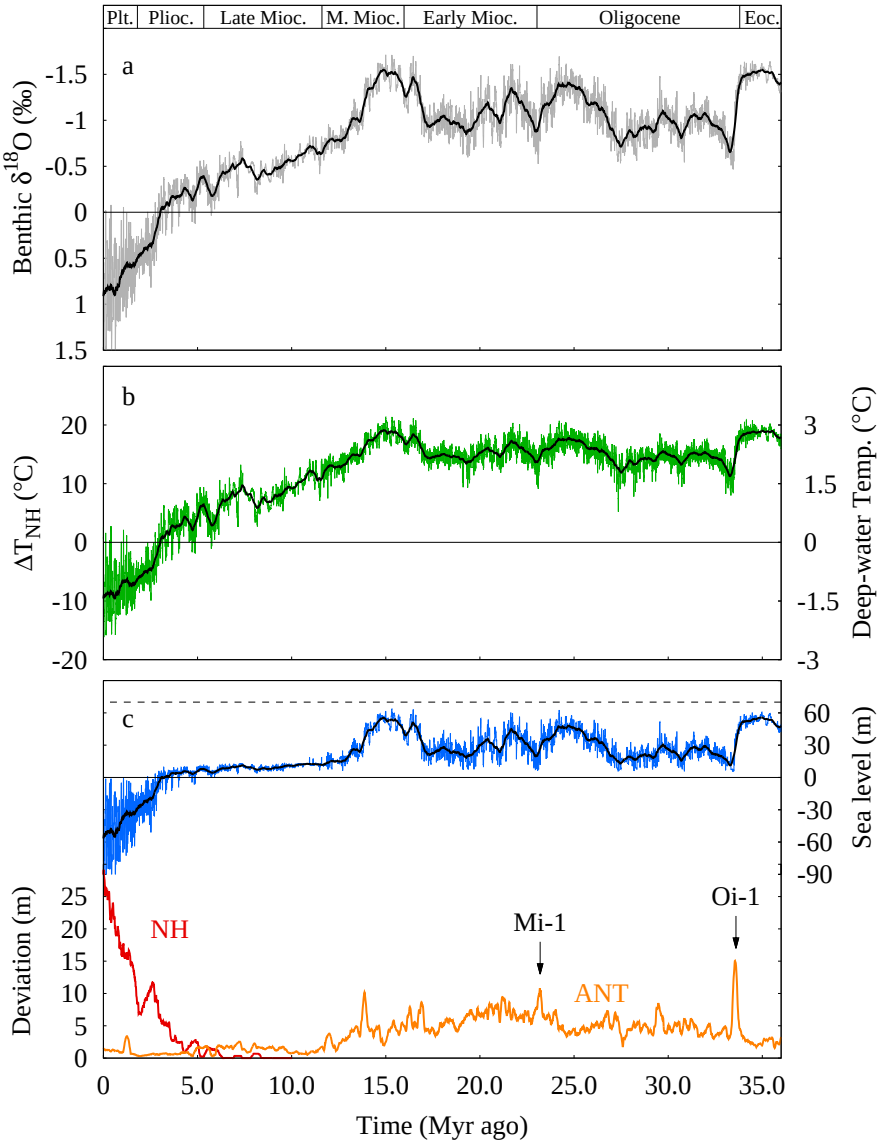

Figure 3.3 | *Reconstruction over 35 Myr.* *(a) The Zachos benthic $\delta^{18}O$ data input (grey) over the past 35 Myr relative to PD (3.23‰). (b) Reconstructed temperature (green). (c) Reconstructed sea level (blue) with the average standard deviation of the ice sheets calculated over 400-kyr periods for the NH (red) and Antarctic (orange). All values are relative to PD, and black lines represent the 400-kyr running mean.*

Secondly, during the late Miocene (around 12–13 Myr ago), deep-water temperature becomes the major contribution to benthic δ^{18}O ($\sim$70%). During this time interval, the modelled EAIS reached its maximum extent, resulting in little change in sea level thereafter (see Fig. 3.3c). Since the benthic δ^{18}O is still increasing during the late Miocene (see Fig. 3.3a), temperature lowers (see Fig. 3.3b) in order to satisfy the requirement that the difference between modelled and observed δ^{18}O is minimised. Thirdly, over the past 3 Myr, ice volume is again the dominant signal due to the waxing and waning of the NH ice sheets. The percentage contribution is only slightly larger than 50%, however.

The model outcome compares favourably with individual benthic δ^{18}O contributions (at the LGM) discussed in the literature. For example, Zachos et al. (2001) stated a contribution of the Antarctic and NH ice sheets of 1.2 and 1.1‰, respectively. Miller et al. (2005) found a slightly lower contribution of the Antarctic ice sheet, 0.8–0.9‰, with a similar NH value of 1.2‰. These values are similar to the outcome of the 1-D model simulations, with contributions at the LGM of 1.0 and 0.8‰ relative to PD, respectively.

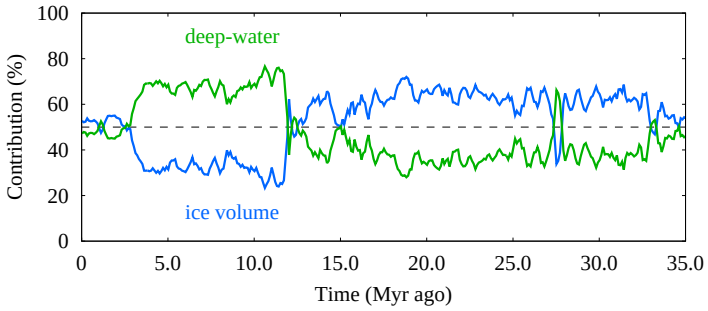

Figure 3.4 | *Percentage contributions to δ^{18}O.* *Percentage contribution of deep-water temperature (green) and ice volume (blue) to changes in benthic δ^{18}O over the past 35 Myr, plotted as a 400-kyr running mean.*

3.3.3 Equilibrium experiment

To further highlight the transition from Southern Hemisphere (SH-) to NH-controlled climate, an equilibrium experiment was performed using a stepwise changing δ^{18}O as input, with steps of 0.1‰. The experiment was initiated at a δ^{18}O value of 1.1‰ then increased to a maximum value of 5.1‰, from which δ^{18}O was reduced back to the initial value. Each δ^{18}O value was kept constant for 60 kyr allowing the ice sheets to develop to a steady state, resulting in an equilibrium temperature and sea level corresponding to every δ^{18}O value.

The experiment shows little hysteresis (Fig. 3.5: black line). An almost equal relationship between temperature and sea level is present compared to the transient experiment (blue boxes with bars). The shift from SH- to NH-dominated climate is well illustrated by the transition period centred around interglacial temperatures (∼0-8 °C above PD). This indicates that interglacials are relatively stable periods compared to ice-volume change over the past 35 Myr, with the Antarctic ice sheet being in a more or less steady state and featuring minor to no glaciation in Eurasia and North America.

The red boxes with bars in Fig. 3.5 represent the transient simulations with the 3-D ice-sheet model (Bintanja et al., 2005a) over the past 1Myr. The results are similar to the 1-D model (in blue) for temperatures until ∼8°C below PD. For lower temperatures, however, there is a significant difference between the two models, for which the 1-D model results reveal lower temperatures for the same ice volume. These differences are mainly due to the inclusion of slightly different isotopic equations, such as equations (3.1) and (3.2), and due to the simplified geometry. As was also mentioned by Wilschut et al. (2006) the lack of hysteresis can also be ascribed to the simplified geometry of the 1-D model.

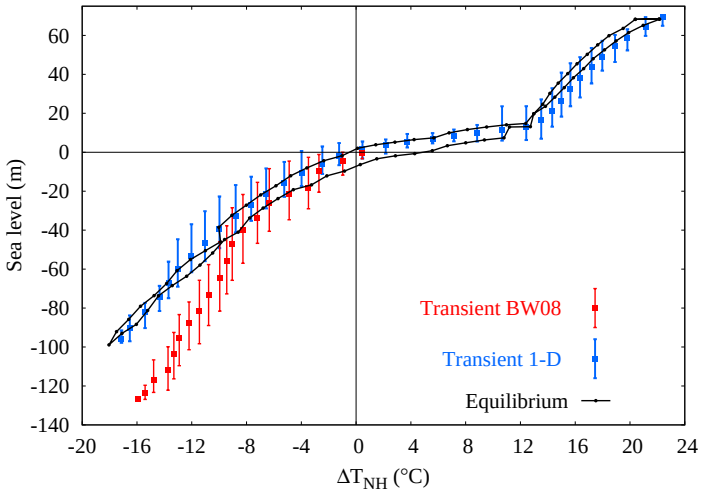

Figure 3.5 | *Equilibrium experiment.* *The experiment plotted for each $\delta^{18}O$ step (black); arrows indicate the direction of stepwise changing $\delta^{18}O$. Average sea level and temperature from the transient simulations for each $\delta^{18}O$ value (within a range of $\pm$ 0.05‰): 1 Myr run of the 3-D model (Bintanja et al., 2005a, in red) and 35 Myr transient run of the 1-D model (blue). The bars indicate the range in sea level.*

3.3.4 Sensitivity tests

A large number of parameters in the model can be varied to satisfy the tuning targets implemented in the methodology, which are shown in Table 3.3. Two parameters, i.e. the deep-water to surface-air temperature coefficient λ_{dw} and the temperature difference with the NH ice sheets, δT_{NH}, were investigated for their sensitivity to model results. Additionally, the uncertainty in the benthic δ^{18}O record has been analysed.

Because the model includes ice sheets in both hemispheres, the outcome of the sensitivity experiments can be divided into two regimes: (1) before inception of NH ice sheets with higher than PD temperatures and (2) a regime including ice in the NH with temperatures (on average) lower than PD, roughly the past 3 Myr. As is implemented in the methodology, the modelled δ^{18}O closely follows the observed $\delta^{18}O_{obs}$ record. In order to satisfy this requirement, each change in deep-water temperature or ice volume is compensated by its counterpart (see equation (3.1)).

This is also shown in Table 3.4; the rightmost two columns list the changes in contribution to δ^{18}O (equal in magnitude and of opposite sign). For experiment A, the deep-water to surface-air temperature coefficient λ_{dw} was replaced by the values shown in the table. The changes are shown with respect to the result with a value of $\lambda_{dw} = 0.20$. For experiment B, the difference between Antarctica and the NH ice sheet, δT_{NH}, was increased/decreased by 4 °C. Changes are shown with respect to δT_{NH} = -10 and -6 °C for the EAIS and WAIS, respectively. In case of experiment C, the contribution changes (in ‰) are not shown since the reference value of the benthic δ^{18}O has been changed itself.

Experiment A: deep-water temperature

The first parameter to be tested, which was also addressed with the 3-D model (Bintanja and Van de Wal, 2008), is the coupling between deep-water and surface-air temperature. This relationship is based on an idealised climate–ocean model that linearly relates the deep-water temperature to the 3-kyr mean NH temperature; see equation (3.5). Bintanja and Van de Wal (2008) used a value of 0.20 for λ_{dw}, which is also adopted for the NH-only experiment described in Section 3.3.1. Similar to the tests performed by Bintanja and Van de Wal (2008), the 1-D model was tested with two additional values for λ_{dw} (0.15 and 0.25; Experiment A) as depicted in Fig. 3.6a.

As can be seen in Table 3.4, changing the λ_{dw} value resulted in coherent changes in temperature and sea level (ice volume). The parameterisation within the model is adjusted by changing λ_{dw}, therefore affecting the deep-water temperature calculation first. Since temperatures are calculated relative to PD, a lower λ_{dw} results in deep-water temperatures closer to PD, i.e. deep-water temperatures are lower and higher prior to and after 3 Myr ago, respectively.

Table 3.4 | *Averaged changes of the three sensitivity experiments over the two periods.*

Experiment	NH temp.	Sea level	Ice volume contribution	Deep-water contribution
	°C	m	‰	‰
A: 35–3 Myr ago				
$\lambda_{\mathrm{dw}} = 0.25$	−1.32	−5.01	0.07	−0.07
$\lambda_{\mathrm{dw}} = 0.15$	1.68	6.97	−0.09	0.09
A: 3 Myr ago to PD				
$\lambda_{\mathrm{dw}} = 0.25$	0.51	4.03	−0.05	0.05
$\lambda_{\mathrm{dw}} = 0.15$	−1.27	−4.90	0.03	−0.03
B: 35–3 Myr ago				
$\delta T_{\mathrm{NH}} + 4$	−2.19	6.98	−0.09	0.09
$\delta T_{\mathrm{NH}} - 4$	1.82	−5.39	0.08	−0.08
B: 3 Myr ago to PD				
$\delta T_{\mathrm{NH}} + 4$	0.08	−0.86	0.00	0.00
$\delta T_{\mathrm{NH}} - 4$	0.47	1.85	0.02	−0.02
C: 35–3 Myr ago				
δ^{18}O - 0.16	1.79	7.61		
δ^{18}O + 0.16	−4.03	−12.02		
C: 3 Myr ago to PD				
δ^{18}O - 0.16	1.56	10.47		
δ^{18}O + 0.16	−3.42	−22.16		

In order to compensate for the changes in deep-water temperature contribution to benthic δ^{18}O, both surface temperatures and ice volume counteract the deep-water temperature changes. In summary, a lower (higher) λ_{dw} leads to a decrease (increase) of deep-water temperatures prior to 3 Myr ago, resulting in higher (lower) surface temperatures and sea level, i.e. less (more) ice volume. After 3 Myr ago, the changes are reversed.

Experiment B: north–south temperature gradient

The second parameter which has been tested is the temperature difference from the NH ice sheets, δT_{NH}, indicating the difference between the Antarctic (or Greenland) and NH continental mean temperature reduced to sea level (without any ice). Although the values shown in Table 3.1 are selected from a realistic range, there is still some uncertainty related to this parameter. Three different sets of values for Antarctica have been chosen to test the sensitivity of the model output in steps of 4 °C, i.e. δT_{NH} = -14 and -10 °C and δT_{NH} = -6 and -2 °C as extreme values. Central values are shown in Table 3.1: δT_{NH} = -10 and -6 °C for the EAIS and WAIS, respectively.

The results with respect to the central values are presented in Fig. 3.6b and clearly show that the separate regimes are also present for this experiment. Prior to 3 Myr ago, the differences are quite large; for the past 3 Myr, however, changes in temperature and

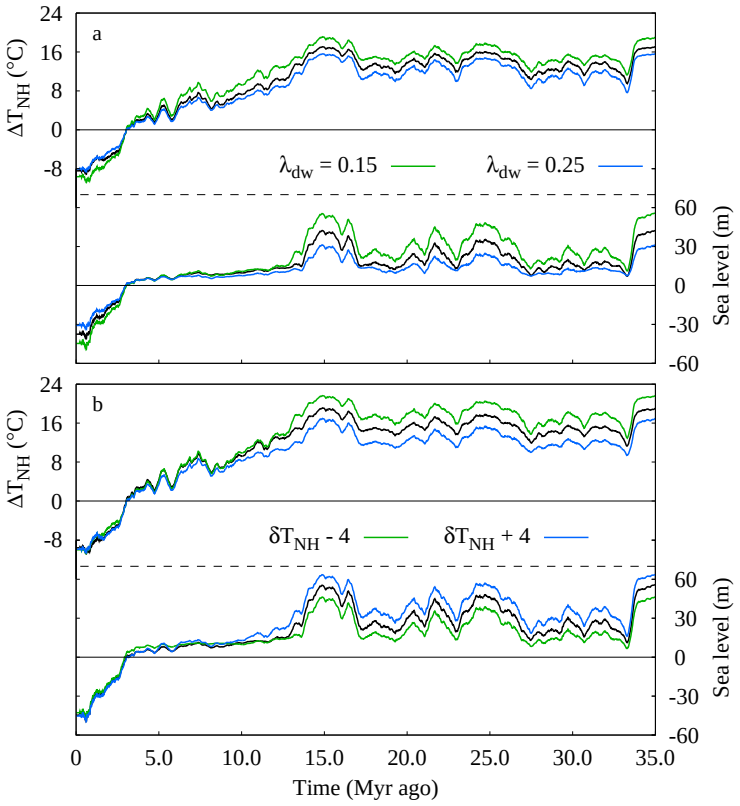

Figure 3.6 | *Sensitivity tests with λ_{dw} and δT_{NH}.* *Tests performed with the model shown as 400-kyr running mean over the past 35 Myr. (a) Varying the deep-water to surface-air temperature coupling, NH temperature (top) and sea level (bottom) over the past 35 Myr. The default experiment with λ_{dw} = 0.20 is shown in black. (b) Varying the temperature difference from the NH ice sheets. Values indicate deviations from the gradients shown in Table 3.1 (black line), $\delta T_{NH} = -12$ and -8 °C (-4, green) and $\delta T_{NH} = -4$ and 0 °C (+4, blue) for the EAIS and WAIS, respectively.*

sea level are much smaller (Table 3.4). For the latter regime this is due to the limited variability of the EAIS and WAIS, as both have reached the continental margins prior to this period. As can be seen in Fig. 3.6b and Table 3.4, a reduction in ice volume is accompanied by an increase in temperature and vice versa (in contrast to Experiment A). Changes prior to 3 Myr ago, however, are quite straightforward. Antarctic surface-air temperature is lower when the temperature difference δT_{NH} is larger, i.e. more negative. Although precipitation is reduced due to a reduction in the moisture-holding content of the atmosphere, the accumulation increases (more snow) and ice volume is increased. To compensate for the increase in ice-volume contribution to benthic δ^{18}O, deep-water and surface temperatures are higher.

The differences over the past 3 Myr, when temperatures are generally below PD, are mainly due to a small reduction in EAIS volume due to a change in accumulation as a result of lower (or higher) temperatures. In summary, a larger (smaller) δT_{NH} increases (decreases) ice volume prior to 3 Myr ago, resulting in an increase (decrease) in ice-volume contribution to δ^{18}O. This is compensated by an increase (decrease) in deep-water and surface-air temperatures.

The choice for the parameters used in the standard experiment is based on the tuning targets, with $\lambda_{dw} = 0.15$ because of a better agreement with Plio-Pleistocene sea-level and NH temperature variations. Furthermore, the choice for δT_{NH} is less significant since its influence is mostly limited to Antarctic ice volume (for which the PD ice volume and a strong increase at Oi-1 are satisfied in all cases). The intermediate values of δT_{NH}, -8 and -4 °C for East and West Antarctica, respectively, are therefore used.

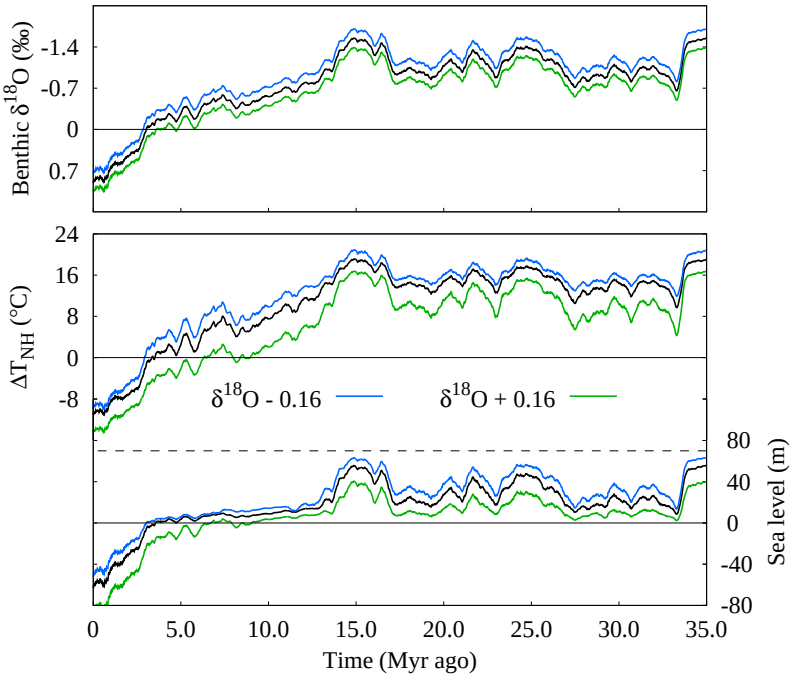

Figure 3.7 | *Sensitivity tests with benthic $\delta^{18}O$.* *Tests performed with the model shown as 400-kyr running mean over the past 35 Myr. Top figure shows the different $\delta^{18}O$ forcing to the model, testing the error in the data record, bottom panel shows the differences for temperature and sea level. The default experiment with the original smoothed data is shown in black, blue is with a $\delta^{18}O$ forcing lowered by 0.16‰, for green the forcing has been increased with 0.16‰.*

Experiment C: uncertainty in the benthic δ^{18}O forcing

To assess the uncertainty in the modelling results that arise from the benthic data record, additional sensitivity tests have been performed by varying the benthic δ^{18}O forcing. To determine this uncertainty, the smoothed record of the data has been compared with the original raw data at the original time points. For each time point the difference has been calculated and over the full time scale the root mean square difference has been determined to be $\sim$0.16‰. To test this uncertainty in the model, this difference of 0.16‰ is added to, or subtracted from, the smoothed record, such that an artificial record is obtained, keeping the PD benthic δ^{18}O value the same.

As is shown in Fig. 3.7, the results are what can be expected. In case of a lowered δ^{18}O record (shown in blue), the results shows higher temperatures and thus less ice volume. In case of an increase in δ^{18}O forcing (in green), the differences are similar, which a decrease in temperature and an increase in ice volume, which is most prominent during the past 3 Myr. The coherent changes of temperature and sea level are also clearly presented in Table 3.4, showing that the model is especially sensitive to an increase in benthic δ^{18}O forcing (green curves), implying colder conditions and larger ice sheets.

3.4 Discussion

A reconstruction of global sea level and NH surface-air temperature over the past 35 Myr has been presented. Following the inverse procedure introduced by Bintanja et al. (2005a) with benthic δ^{18}O as input, the δ^{18}O signal has been separated into an ice-volume and deep-water temperature contribution.

The results of the 1-D model, however, can be affected by several model parameters such as the deep-water to surface-air temperature coupling (λ_{dw}) and the difference between the Antarctic and NH continental temperature (δT_{NH}). It has been shown that both parameters have a significant influence on the individual contributions of ice volume and temperature to the benthic δ^{18}O signal. The largest differences in model results were found prior to 3 Myr ago. Changes in the contribution of ice volume were about 10%, which are essentially changes in Antarctic ice volume as NH ice sheets had not yet developed.

Due to the simple geometry and the use of a fixed-grid ice-sheet model, the modelled Antarctic ice sheets showed little sensitivity to sea-level change. Tests have been carried out using a stretching grid, but over the past 35 Myr differences were very small compared to the fixed-grid simulations. For these long-term changes, the low sensitivity is therefore not a concern for Antarctic ice-volume evolution.

Over the past 3-5 Myr, however, Antarctic ice volume stays more or less constant, which is not in agreement with several other studies (e.g. Conway et al., 1999; Huy-

brechts, 2002; Pollard and DeConto, 2009). The large sea-level fluctuations during the Pleistocene allowed the grounding line of the WAIS to migrate through the shallow Ross and Weddell Seas (Conway et al., 1999), increasing its volume significantly during glacial maxima. Although sea-level and temperature fluctuations over the Plio-Pleistocene are mainly caused by changes of the NH ice sheets, the simple geometry of the Antarctic ice sheets does not allow for large changes in West Antarctica. According to other modelling studies, differences in Antarctic ice volume could be of the order of 10 m of sea level (Huybrechts, 2002). For the Pleistocene, therefore, a significant uncertainty range ($\sim$10%) can be accounted for during glacial periods.

Table 3.5 | *Comparison of model constants used in this study and by Oerlemans (2004b).*

Constant	This study	Oerlemans (2004b)
ΔT_o VPDB (°C)	8.3	8.9
γ and b (‰ °C^{-1})	–0.28	–0.25
$(I_\mathrm{i}/V_\mathrm{o})_\mathrm{PD}$ and c (‰ m^{-3})	3.26×10^{-17}	4.0×10^{-17}

3.4.1 Comparison of reconstructed sea level

Although there is some uncertainty related to the short-term changes, over the past 35 Myr the reconstructed sea level and temperature records are comparable to observations and other studies. For example, Oerlemans (2004b) used a continuity model for the Antarctic ice sheet to separate the deep-water temperature and ice-volume signals from the benthic δ^{18}O record. Overall the methodology is quite different, but in this study an axisymmetric model is also used with a sloping bed.

The method of Oerlemans (2004b) is based on a linear relation between δ^{18}O and both deep-water temperature and ice volume:

$$\delta^{18}O = a + bT_o + cV_i, \tag{3.10}$$

where a is related to the deep-water temperature for δ^{18}O = 0, if the stable oxygen isotope ratio is at the VPDB standard level. From equation (3.10), the deep-water temperature is derived as a function of δ^{18}O (input) and ice volume (calculated with the model). Furthermore, the Antarctic temperature is related to the deep-water temperature (Oerlemans, 2004b, equation (7)) as a function of Δ, a constant temperature difference between the deep-sea and Antarctic continent, and to an additional feedback parameterisation between ice sheet and climate.

For a more straightforward comparison with the approach presented here, equation (3.10) can be restated relative to PD (similar to the treatment of equation (1.7) in Section 1.5):

$$\Delta\delta^{18}O = b\Delta T_o + c\Delta V_i. \tag{3.11}$$

When comparing equations (3.11) and (1.7), the biggest difference is the constant c; it is assumed that the isotopic content of the ice-sheet and ocean volume remains constant throughout the Cenozoic. Nevertheless, as shown in Table 3.5, the constants are similar to those used in this chapter.

A comparison of both reconstructions is shown in Fig. 3.8, for which the original compilation by Zachos et al. (2001) was used, interpolated to a 100 years resolution as input for a better comparison with Oerlemans (2004b) (who used the same input smoothed to a 100-kyr resolution). From the Eocene to the middle Miocene ($\sim$10 Myr ago), the 1-D model reconstructed Antarctic ice volume (blue curve in Fig. 3.8b) is very similar to that of Oerlemans (2004b) for $\Delta = 9\ ^{\circ}C$ (shown in orange). The deep-water temperature reconstructions, however, are less similar as shown in Fig. 3.8a. In particular, 1-D model temperatures are significantly lower during the Oligocene (33-26 Myr ago) and mid- to late Miocene (15-4 Myr ago). The average trend over the latter period, however, is comparable, with approximately equal temperatures at 15 and 4 Myr ago.

In addition to the comparison with other modelling results, Fig. 3.9a shows a comparison with two long-term records over the past 35 Myr by Müller et al. (2008) (red) with error envelope and Miller et al. (2005) (green). The Müller curve shows a reconstruction of the effects of changes in crustal production, sediment thickness, ocean-basin depth and area on sea level, and illustrates sea-level changes owing to long-term effects other than ice-volume fluctuations. Although the mean (thick red line) curve

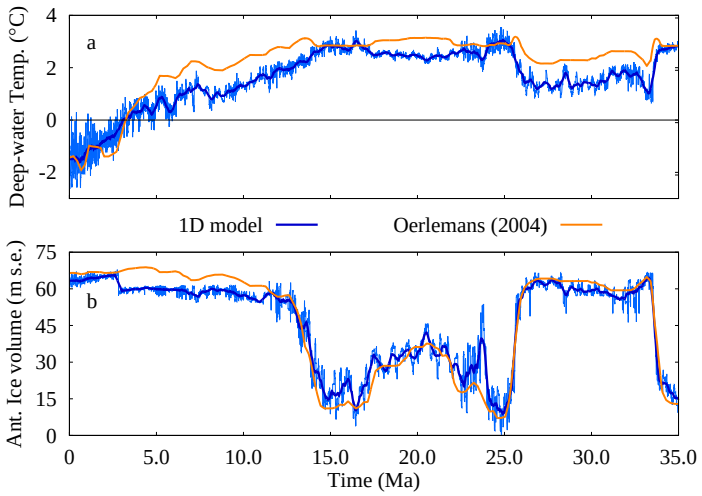

Figure 3.8 | *Comparison with Oerlemans (2004b).* *(a) Reconstructed deep-water temperature relative to PD and (b) Antarctic ice volume of the 1-D model (blue). The dark blue curve is the 400-kyr running mean, and the results from Oerlemans (2004b) for $\Delta = 9\ ^{\circ}C$ are in orange.*

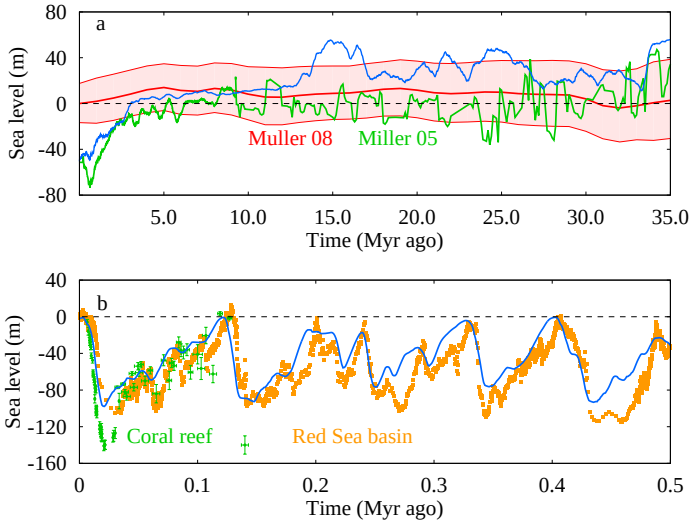

Figure 3.9 | *Reconstructed sea level (blue) compared with other sea-level reconstructions.* *(a) Over the past 35 Myr with sea-level curves of Müller et al. (2008) in red with error envelope and Miller et al. (2005) in green; and (b) over the past 0.5 Myr with Red Sea basin sediment $\delta^{18}O$ records (Rohling et al., 2009) and New Guinea and Barbados coral reef data (Lambeck and Chappell, 2001).*

does not show much variability over the past 35 Myr, the error envelope is significant and shows that there is still much debate about past sea-level height. Nevertheless, the volume of the ocean basin only changes by a maximum of $\sim$1% (Müller et al., 2008) and therefore shows that the assumption of a constant ocean depth and area is acceptable.

The Miller et al. (2005) sea-level record (in green) prior to 9 Myr ago is based on 'backstripping' a New Jersey stratigraphic record, which mainly accounts for the effects of sediment compaction, loading and water-depth variations. Changes in Antarctic ice volume are taken into account, but are smaller than the 1-D model simulations (blue curve). The record shows strong variability and, prior to 10 Myr ago, seems to agree more with the record of Müller et al. (2008) than with the sea-level curve derived from the 1-D ice-sheet models. Over the past 10 Myr the similarities are evident. Over this period, however, the Miller et al. (2005) record is directly derived from $\delta^{18}O$ using a scaling of 0.1‰ per 8 m and correcting the data prior to 2.5 Myr ago by 0.5‰ due to deep-ocean cooling. However, this is inconsistent with the 1-D model derived relationship, clearly showing a variable contribution of temperature (see Fig. 3.3). It is therefore not surprising that both records show a coherent drop in averaged sea level over the past 5 Myr.

A completely independent comparison can be seen in Fig. 3.9b, which shows past sea-level changes derived from Red Sea sediments (Rohling et al., 2009) and coral reef data from New Guinea and Barbados (Lambeck and Chappell, 2001). In terms of timing of glacial maxima, i.e. minima in sea level, the agreement is evident although the comparison for Termination V ($\sim$0.42 Myr ago) has improved with respect to a previous reconstruction (Siddall et al., 2003). The amplitude of the reconstructed sea level (blue curve) is, however, smaller for all past terminations, mainly due to the small amplitude in the Zachos et al. (2008) δ^{18}O record.

3.5 Conclusions

A complete global ice-volume reconstruction has been presented, mutually consistent with NH surface-air temperatures and benthic δ^{18}O over the past 35 Myr, using a consistent method to derive the ice volume and temperature signal from benthic δ^{18}O records. The method has worked well for a combination of five ice-sheet models representing glaciation of all the major ice sheets which existed during the Cenozoic.

The main result of the 1-D ice-sheet model simulation over the past 35 Myr shows that the contributions of ice volume and deep-water temperature to the benthic δ^{18}O data exhibit large variations and cannot be assumed constant. Moreover, the results show a shift from a climate dominated by SH ice sheets to one dominated by NH ice sheets over the past 35 Myr, and reveal that the relationship between sea level and temperature is not constant with time.

Furthermore, it is shown that the 1-D ice-sheet model performs in line with the 3-D model results presented in Bintanja and Van de Wal (2008) over the past 4 Myr and agrees well with observed sea-level records. The ice-sheet model, however, is a simplified representation of an actual ice sheet and has several limitations such as the unrealistic geometry, which does not support the merging of ice sheets and the formation of ice shelves. Also, as has been shown in Section 3.3.4 the modelling results can be quite sensitive to the chosen parameters, which are subject to change. Moreover, the modelling results are shown to have the largest changes due to a change in the benthic δ^{18}O forcing, for which average differences relative to the standard run are 1.7 °C for temperature and 7 m s.e. ice volume (averages of differences shown in Table 3.4).

In the following chapter, a more in-depth investigation on the transient nature of these results will be presented, i.e. how do temperature and sea level vary relative to each other and how does this influence the interpretation of benthic δ^{18}O data? Additionally, another sensitivity test has been performed related to the ice-volume contribution to benthic δ^{18}O, followed by a complete assessment of the uncertainty of the modelling results to summarise the 1-D ice-sheet model reconstructions.

4

The transient nature of Earth's climate

From the marine benthic δ^{18}O records it is known that the Earth's climate has experienced significant variability over the past 40 million years. In general, a number of assumptions are often needed to disentangle the benthic δ^{18}O data into its temperature and ice-volume contributions. In this chapter, a more in-depth analysis is presented of the 1-D modelling results presented in Chapter 3. The contribution of land ice to benthic δ^{18}O is examined with a set of sensitivity experiments, varying the mean δ^{18}O of the ice for different ice sheets. It is shown that the scaling factor of sea-water δ^{18}O (δ_w) to sea level is not constant over the long time scales. However, the sensitivity experiments do show that over the long time scale, the general assumed 1.0-1.1‰ per 100 meters of sea level is in reasonable agreement with the 1-D model results. Moreover, the sea-level (ice volume) response to temperature ($\Delta S/\Delta T$) is shown to vary through time, with the largest response found when variations in Antarctic ice volume dominates the sea-level variations during the Oligocene to Early Miocene. Furthermore, this response is quite large compared to the individual response of ice sheets during the Plio-Pleistocene, whereas the combined $\Delta S/\Delta T$ in this period is comparable to that during the Oligocene. Accordingly, the transient behaviour is very important for the interpretation of data records, with respect to climate sensitivity and climate change during the past 40 million years.

This chapter is based on:
De Boer, B., R. S. W. van de Wal, L. J. Lourens and R. Bintanja, The transient nature of Earth's climate and its implications on the interpretation of benthic δ^{18}O records, *Palaeogeography, Palaeoclimatology, Palaeoecology*, in press, 2011.

4.1 Introduction

Over the past 40 million years (Myr), the Earth's climate has changed significantly, and went through a series of different climate states, as is clearly reflected in the benthic δ^{18}O record (Zachos et al., 2001). The most prominent features being: (1) a climate without large ice sheets prior to 33.8 Myr ago (e.g. Coxall et al., 2005; Lear et al., 2008); (2) a partially glaciated Antarctica from 35 to 15 Myr ago (e.g. DeConto and Pollard, 2003a; Oerlemans, 2004b; Van Tuyll et al., 2007; Langebroek et al., 2009); (3) glacial conditions with large glacial extent on both hemispheres; and (4) interglacial stage, with (partial) ice cover on Antarctica and Greenland, such as the PD conditions. (e.g. Van de Wal, 1999b; Huybrechts, 2002; Tarasov and Peltier, 2003; Zweck and Huybrechts, 2005; Bintanja and Van de Wal, 2008; Pollard and DeConto, 2009)

Climate models have been used for the interpretation of geological data in the past (e.g. Huber et al., 2004; Braconnot et al., 2007; Haywood et al., 2009), with a focus on comparing independent paleo data with climate model variables. However, for processes on time scales of Myr, limited computer power severely restrict the level of sophistication of transient simulations. A comprehensive Atmosphere Ocean General Circulation Model (AOGCM) with resolution of about 100 km is still not feasible for long transient runs. For this reason many equilibrium, or time slice, experiments have been performed. These experiments, however, cannot be used to study processes which are determined by the slow transient nature of the system, such as ice-sheet evolution, for which forcing and response are on the order of 1,000 to 10,000 years (1-10 kyr).

Another issue with the interpretation of geological records is that often idealised assumptions, with respect to other climate variables, are needed for the interpretation. For example, the marine benthic δ^{18}O record, which is a mixture of temperature and ice volume (Chappell and Shackleton, 1986), can be interpreted in terms of deep-ocean temperature if ice volume is known, or vice versa. The inverse forward modelling approach presented in Chapter 2, combined with physical based ice-sheet models, serves as a basis to disentangle the benthic δ^{18}O record. With this type of model the continental mean surface-air temperature for the Northern Hemisphere, relative to PD is reconstructed based on benthic δ^{18}O data (Lisiecki and Raymo, 2005; Zachos et al., 2008) as constraint. The temperature is used to calculate deep-water temperatures and ice volume, and as a result a self-consistent and continuous record of δ^{18}O, eustatic sea level (inverted from ice volume) and NH temperature is generated over the past 40 Myr with a 0.1 kyr resolution.

Fig. 4.1 shows the modelled climate over the past 40 Myr, the standard results as shown in Fig. 3.3 in Chapter 3, for which a large part is dominated by variability of the Antarctic Ice Sheet (AIS), while major NH glaciation only occurred during the

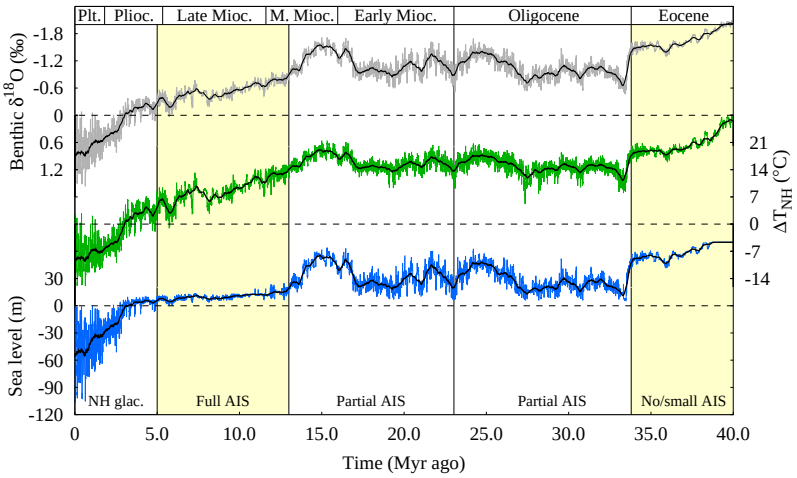

Figure 4.1 | *1-D Ice-sheet model results over the past 40 million years.* *From top to bottom, the deep-sea benthic $\delta^{18}O$ forcing (Zachos et al., 2008) in grey, Northern Hemisphere continental mean surface temperature (green) and sea level (blue). All values are relative to PD, with black lines indication 400-kyr running means. The different climate states as mentioned in the text are indicated at the bottom. (AIS: Antarctic Ice Sheet, NH glac.: Northern Hemisphere glaciation)*

past 5 Myr. Fig. 4.1 clearly illustrates the transient behaviour of the system which is the focus of this chapter. Firstly, in Section 4.2 a short summary is given of the modelling strategy, which is thoroughly explained in Chapter 2, and its position within the framework of paleoclimate modelling in general. Secondly, in Section 4.3 we present a more extensive analysis of the result presented earlier, for which new sensitivity tests have been performed on the mean $\delta^{18}O$ of the ice sheets. Thirdly, Section 4.4 deals with the transient nature of key climate variables such as sea level, ice volume and temperature, using the sensitivity test presented in Section 4.3, and an additional experiment to investigate the influence of assuming a constant value for the $\delta^{18}O$ of the ice sheets. Lastly, this is followed by a more in-depth analysis of the sensitivity of the individual ice sheets to changes in temperature.

4.2 Model strategies

4.2.1 Modelling paleoclimate

Over the past few decades there have been numerous examples of paleoclimate modelling. Most commonly used are the stand-alone experiments of General Circulation Models (GCMs) and of ice-sheet models, whereas GCM experiments also have been used in different forms such as atmosphere only, or coupled to an ocean and/or veg-

etation model. Most recently, intercomparison projects with GCMs, such as PMIP2 (Braconnot et al., 2007) and PlioMIP (Haywood et al., 2009), have focused on steady-state experiments of the mid-Holocene and Last Glacial Maximum (LGM) and on the mid-Pliocene climate, respectively. More deep-time experiments have also been conducted by, for example, Huber et al. (2004) who investigated the Eocene climate, before major glaciation started on the Antarctic continent. Notwithstanding, these models are highly sophisticated and serve a great number of detail in terms of climate variables, they are less suited for the analysis of slowly progressing transient processes such as the evolution of ice sheets.

Besides the GCM experiments, ice-sheet models have been used in stand-alone experiment for over 3 decades, including the key processes involved in the evolution of ice sheets such as ice deformation, snow accumulation and melt at the surface (i.e., the surface mass balance), basal melting and depression and rebound of the underlying bedrock. Naturally, there are different approaches to force the ice-sheet model and to determine its surface mass balance (Pollard, 2010), such as using an energy balance model (Tarasov and Peltier, 1997; Langebroek et al., 2009), asynchronous coupling with climate models (DeConto and Pollard, 2003b,a) or using climate parameterisations (e.g. Huybrechts, 2002; Bintanja et al., 2002; Tarasov and Peltier, 2003; Zweck and Huybrechts, 2005; Bintanja and Van de Wal, 2008; Pollard and DeConto, 2009). Although fully synchronous coupled ice sheet-climate models are the most sophisticated and favourable approach, Myr transient simulations are restricted by limited computer power. However, Earth Models of Intermediate Complexity (EMICs) have been used to perform simulations in the order of 100 kyr (e.g. Kageyama et al., 2004; Lourens and Tuenter, 2009; Ganopolski et al., 2010; Ziegler et al., 2010). Likewise, energy balance climate models have been used for simulations over the past glacial cycles (Berger, 1992; Berger et al., 1998), and for Miocene climate simulations coupled to a 2.5-D ice-sheet model of the Antarctic ice-sheet (Langebroek et al., 2009, 2010).

Concerning the surface mass balance, the use of climate parameterisations is most suitable for long-term simulations. In some studies, the initial temperature and precipitation fields originate from GCMs and are adjusted according to glacial-interglacial scaling between GCM fields (Zweck and Huybrechts, 2005; Pollard, 2010). Regardless of the wide range of different types of paleoclimate reconstructions, long transient simulations, as has been introduced in Chapter 3, are sparse.

4.2.2 Ice-sheet models forced with oxygen isotopes

The best examples of long-term climate records of benthic foraminifera are the stacked data sets of Lisiecki and Raymo (2005) (LR04) and Zachos et al. (2008) which cover 5 and 65 Myr of Earth's history, respectively. Pollard and DeConto (2009) used the

stacked LR04 record to largely parameterise the mechanisms involved in forcing an ice-sheet model for the Antarctic ice sheet. In their approach, sea level is determined in proportion to δ^{18}O, and already existing surface temperature and precipitation parameterisations (see references therein) are varied as function of δ^{18}O. Furthermore, a sub-ice-shelf oceanic melt parameterisation is implemented which is believed to be controlled by climatic influences that vary in coherence with NH glacial-interglacial cycles, and thus with deep-sea δ^{18}O or the Plio-Pleistocene. However, they do not attempt to separate the temperature and sea-level information in the benthic δ^{18}O record in a systematic way.

In this chapter, a more comprehensive analysis is presented of the results shown in Chapter 3, focusing on the transient nature of sea level, temperature and benthic δ^{18}O, using five 1-D axisymmetrical ice-sheet models representing the Eurasian Ice Sheet (EuIS), the North American Ice Sheet (NaIS), the Greenland Ice Sheet (GrIS) and the East and West Antarctica Ice Sheet (respectively EAIS and WAIS). All five ice-sheets have different characteristics which are representative for each individual ice-sheet. Furthermore, the ice-sheet model incorporates changes in the isotopic depletion of the ice-sheet, $\delta^{18}O_i$, which varies as a function of temperature and elevation. Additionally, the mass-balance parameterisation includes key processes such as the change in albedo and the mass balance height feedback, and the bedrock elevation is adjusted locally to changes in the ice load, with a relaxation time of the asthenosphere of 3 kyr. A more thorough description of the model and methodology is presented in Chapters 1 and 3.

4.3 Assessing the uncertainty in $\delta^{18}O_i$

An important source of uncertainty for this type of simulations arises from the uncertainty in the PD distribution of $\delta^{18}O_i$. For this reason a number of sensitivity experiments have been performed, changing the PD distribution of oxygen isotopes for Antarctica and Greenland. For all ice sheets, the isotopic depletion of the ice as function of time is calculated with (equation (3.2)):

$$\delta^{18}O_i = \delta^{18}O_{PD} + \beta_T \Delta T + \beta_Z \Delta Z, \tag{4.1}$$

with $\delta^{18}O_{PD}$ the PD distribution over the ice sheet, which is calculated from the mean annual temperature, ΔT and ΔZ are the changes in temperature and elevation relative to PD, respectively, and β_T and β_Z are the isotopic sensitivity and isotopic lapse rate (shown in Table 3.1), respectively, which are kept constant and adopted from Lhomme and Clarke (2005). Although there is quite a good knowledge on the PD distribution of the isotopic composition of the surface snow (e.g. Masson-Delmotte et al., 2008; Wang et al., 2009), to translate this to a mean excess of the entire ice sheet requires a tracer-

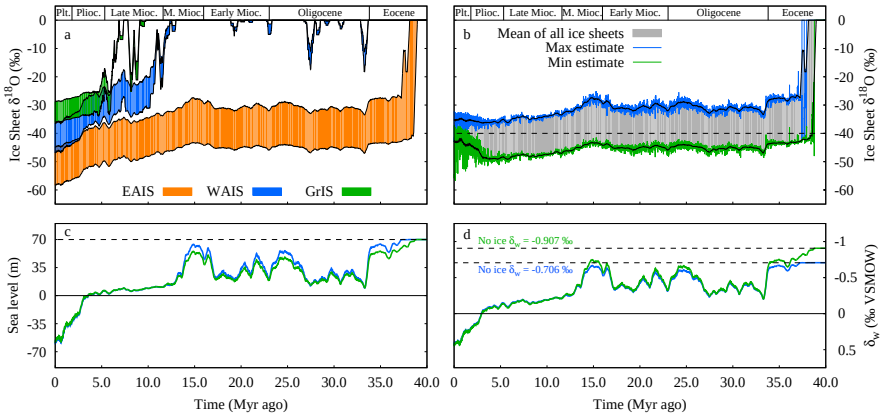

Figure 4.2 | *Modelling results over the past 40 Myr.* *a) Bulk $\delta^{18}O_i$ of the GrIS (green), WAIS (blue) and EAIS (orange), showing the range between the maximum and minimum estimates of PD $\delta^{18}O_i$ indicated in Table 4.1; b) The mean bulk $\delta^{18}O_i$ of all ice sheets combined, the high time-resolution data for the maximum estimate (blue) and minimum estimate (green), and the range between the two estimates averaged over 400 kyr (grey area). The dashed line represents -40‰, which is the constant values assumed in the δ_w to sea-level ratio experiment presented in Fig. 4.3b; c) Eustatic sea level for the maximum and minimum estimates; and d) sea-water $\delta^{18}O$ (δ_w) for the maximum and minimum estimates. The two dashed lines indicate the values when no ice is present (∼ prior to 39 Myr ago) for the two experiments. All variables are plotted as 400-kyr running means calculated for each 10 kyr, except for the coloured lines in figure b.*

transport scheme (e.g. Lhomme and Clarke, 2005; Clarke et al., 2005; Sima et al., 2006) which is not included in the 1-D axisymmetrical ice-sheet model experiment.

Nevertheless, there is a wide range of estimates present in the literature for the isotopic depletion for all large ice sheets that have existed in the past, as shown in Table 4.1. Minimum and maximum estimates have been used to perform sensitivity tests for the three large ice sheets that are present today, i.e. the EAIS, WAIS and the GrIS. Here, the maximum estimates are calculated from the surface distribution equations of Zwally and Giovinetto (1997) and Giovinetto and Zwally (1997) for the Greenland and Antarctic ice sheets, respectively. The minimum estimates mainly come from an ice-dynamical perspective, showing that the PD polar ice sheets consist of ice several tens of kyr old, resulting in a more depleted ice sheet consisting of older ice formed during glacial times (Lhomme and Clarke, 2005).

Since the focus is on the longer time scales, no tests have been performed on minimum or maximum estimates for the EuIS or NaIS, although they are shown in Table 4.1. To calculate the $\delta^{18}O_i$ of both ice sheets, the surface distribution equation for Greenland was used (Zwally and Giovinetto, 1997). Average values during glacial times vary between -25 and -28‰, similar to the values calculated with the 3-D ice-sheet model (Bintanja et al., 2005a), and well within the range indicated in Table 4.1.

Table 4.1 | *Minimum and maximum estimates for PD ice-sheet* $\delta^{18}O_i$.

Ice sheet	Min $\delta^{18}O_i$	Max $\delta^{18}O_i$
EAIS	-55[1]	-43[2]
WAIS	-42[1]	-32[2]
GrIS	-36[3]	-28[4]
NaIS (LGM)	-34[3]	-28[3]
EuIS (LGM)	-40[3]	-16[3]

[1]Lhomme and Clarke (2005)
[2]Giovinetto and Zwally (1997)
[3]Duplessy et al. (2002)
[4]Zwally and Giovinetto (1997)

As can be seen in Fig. 4.2a, the large differences between the maximum and minimum estimates are clearly pronounced over the entire period, especially for the EAIS (in orange). Furthermore, it is evidently shown that during the Oligocene to Mid Miocene the Antarctic ice-sheet is less depleted and rather constant, in coherence with the warmer climate as illustrated in Fig. 4.1. Moreover, the bulk $\delta^{18}O_i$ of all ice sheets shows a strong decrease during the Late Miocene towards the Late Pleistocene, which is also due to an increase in ice volume and thus lower temperatures. However, the mean bulk $\delta^{18}O_i$ of all ice sheets combined, as shown in Fig. 4.2b, remains rather constant during the last 5 Myr. Nevertheless, the variability on the short (0.1-10 kyr) time scale is quite strong. Moreover, the mean bulk $\delta^{18}O_i$ increases during the Plio-Pleistocene, especially for the minimum estimate experiment, due to the increase of ice volume on the NH, which is much less depleted in comparison to the AIS.

Although the uncertainty in PD $\delta^{18}O_i$ is clearly pronounced in the time-related variability of $\delta^{18}O_i$ itself, it seems to have less impact on other variables such as sea level (Fig. 4.2c) and δ^{18}O of the sea water (Fig. 4.2d). The largest differences occur during the Oligocene and Miocene, when both sea level and δ_w are slightly higher for the maximum estimate (blue curve) with respect to the minimum estimate (green curve). On the longer time scale, however, the two experiments appear to be very similar.

4.4 Analysis of transient behaviour

4.4.1 Sea level to δ_w ratio

The interpretation of the geological records can be very complicated and, especially in case of the benthic δ^{18}O data, idealised assumptions are often used to disentangle the climate information it encloses. For example, a constant value for the bulk $\delta^{18}O_i$ is considered, which is used to calculate the change in δ_w using mass conservation (the

2nd and 3th terms on the r.h.s. of equation (2.2)):

$$\delta_w = -\frac{\overline{\delta^{18}O_i V_i}}{V_o} + \left[\frac{\overline{\delta^{18}O_i V_i}}{V_o}\right]_{PD}, \tag{4.2}$$

Here, the first term on the r.h.s. represents the time-dependent variables calculated with the model, and the second term represent the constant PD contribution of the ice-sheets to δ_w, i.e. the contribution of the PD ice sheets when they would melt completely. The results from the minimum and maximum experiments are shown in Fig. 4.2d, for which the dashed lines indicate the resulting PD contribution, i.e. the second term in equation (4.2). Since the reference state of δ_w, the Vienna Standard Mean Ocean Water (VSMOW) is defined at a value of 0‰, equation (4.2) represents both the absolute value of δ_w (in VSMOW) and the change relative to PD.

By assuming a constant value for the bulk $\delta^{18}O_i$, a constant ratio of δ_w relative to sea level (derived from ice volume V_i) is determined, which is used to derive sea level from δ_w or vice versa. In the literature, a wide range of values has been proposed, as shown in Table 4.2. Here, the highest and lowest values are adopted from the study of Duplessy et al. (2002), who analysed a variety of different resources in terms of bulk $\delta^{18}O_i$ and ice volume, ending up with a high and low estimate of the δ_w range during the LGM. The corresponding values for the mean bulk $\delta^{18}O_i$ are shown in Table 4.2, varying from -29 to -43‰, quite close to the range shown in Fig. 4.2b.

For the two sensitivity experiments, the sea-level and δ_w variability did not differ significantly, as presented in Fig. 4.2c and d. However, their ratio does show a large distinction due to the difference between the maximum and minimum estimate of $\delta^{18}O_i$, which is illustrated in Fig. 4.3a. Moreover, additional experiment were performed with a constant δ_w to sea-level ratio of 0.01‰ per 100 m. From equation (4.2) follows, assuming no change in ocean volume and an average ocean depth of 4 km, that the accompanying constant bulk $\delta^{18}O_i$ is -40‰, within the range of the values shown in Table 4.2.

Table 4.2 | *Different δ_w to sea-level ratios used in the literature and the accompanying ice-sheet $\delta^{18}O$.*

$\Delta\delta_w$(‰) per 100 m	$\delta^{18}O_i$ (‰)	Origin	Reference
0.80	-30.3	LGM reconstruction (low estimate)	Duplessy et al. (2002)
0.85	n.a.	LGM scaling from observations	Waelbroeck et al. (2002)
0.85	-29.1	Miocene modelling (low estimate)	Langebroek et al. (2010)
0.97	-35.0	LGM observations	Chappell and Shackleton (1986)
1.00	n.a.	LGM scaling (Fairbanks, 1989)	Sosdian and Rosenthal (2009)
1.08	-42.7	Miocene modelling (high estimate)	Langebroek et al. (2010)
1.10	-42.0	LGM observations	Fairbanks (1989)
1.12	-40.3	LGM reconstruction (high estimate)	Duplessy et al. (2002)

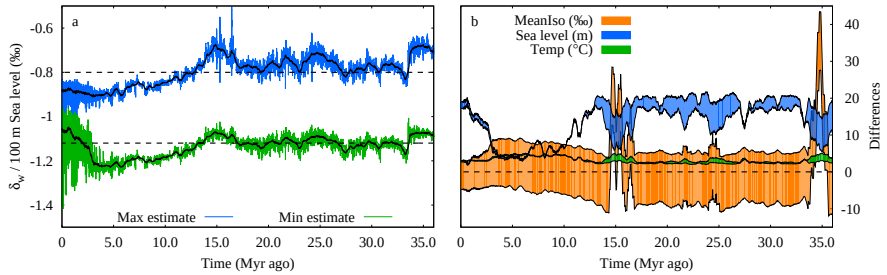

Figure 4.3 | *Sensitivity in model parameters.* *a) Variations in the δ_w to sea-level ratio (per 100 meters) over the past 36 Myr. Similar to Fig. 4.2, showing the maximum estimate experiment (blue) and the minimum estimate (green). Dashed lines indicate the highest and lowest values shown in Table 4.2. b) Differences for the constant δ_w to sea-level ratio experiment (= 1‰ per 100 m) with the maximum and minimum estimate results, for the mean bulk $\delta^{18}O_i$ (‰ in orange; the difference between -40‰ and Fig. 4.2b), for sea level (m in blue), and for temperature (°C in green). Black lines indicate the 400-kyr running means.*

As can be seen in Fig. 4.3b, the differences for sea level, temperature and bulk $\delta^{18}O_i$ are quite pronounced. Naturally, there is a clear departure from the calculated bulk $\delta^{18}O_i$ values (in orange), which is the difference between -40‰ and the results illustrated in Fig. 4.2b. Although the differences for temperature are not so strong, on average around 3 °C, the influence on modelled sea level is evident, varying from 3 to 20 meters. The result of Fig. 4.3a clearly shows the transient nature of the Earth's climate, as a lot of variability is enclosed within just a single parameter. Although the proposed constant values of the δ_w to sea-level ratio shown in Table 4.2 are for the larger part enclosed within the maximum (in blue) and minimum (in green) estimated curves, the results of Fig. 4.3b evidently illustrate that over the longer time scale the use of a constant value can lead to inaccurate interpretation of the data.

4.4.2 Ice volume response to temperature

To furthermore emphasise the large variability the Earth's climate has experienced, the sensitivity of ice-volume change relative to a change in temperature has been analysed. Since this parameter, ΔS/ΔT, is poorly defined for very small changes in both variables, the data has been filtered over 100 kyr and additionally a 400-kyr running mean is applied for each 10 kyr, for which the results are illustrated in Fig. 4.4.

The different climate states mentioned in Section 4.1 are easily recognised in Fig. 4.4. Firstly, a partial glaciated Antarctica, which occurs throughout the Oligocene to Mid Miocene (prior to ∼13 Myr ago), shows quite a variable climate sensitivity (orange curve), with smaller values related to an almost entirely glaciated continent, or no ice sheet at all (before ∼39 Myr ago). Secondly, during the past 5 Myr it is clear that climate is dominated by glaciation on the NH, predominantly by the EuIS (in blue)

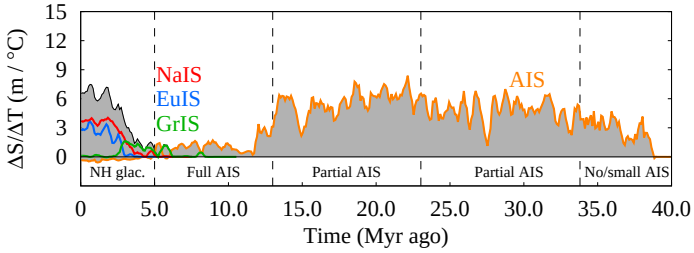

Figure 4.4 | *Sea-level change to temperature change ratio over the past 40 Myr.* *For the NaIS (blue) and EuIS (red) ice sheets, for the GrIS (green) and the response of the AIS (orange) to temperature change, the grey shaded area shows the response of all ice sheets combined. Data is averaged over 400-kyr, plotted for each 10 kyr.*

and NaIS (in red). Although ice volume during glacial maximum, especially for the NaIS, is quite comparable to that of the AIS, sensitivity for the individual ice sheets is lower, whereas the climate sensitivity of all ice sheets combined (grey shaded area) is quite similar for the Pleistocene and prior to 13 Myr ago.

During the Plio-Pleistocene, however, the sensitivity of the AIS (orange curve) shows slightly negative values of sea-level change relative to a change in temperature. Since the model setup does not contain a shallow sea for the WAIS, ice-volume change during glacial times is predominantly restricted to the surface mass balance of both the EAIS and WAIS, which due to lower temperatures is reduced, i.e. lower temperatures lead to a lower moisture capacity of the atmosphere, leading to lower precipitation. This is in coherence with other modelling studies (e.g. Huybrechts, 2002), who also found a reduction in surface elevation of the EAIS during the LGM.

Lastly, the most distinguishable climate state within the past 40 Myr occurred between 5 and 13 Myr ago. This period is characterised by a very small climate sensitivity, due to a fully glaciated Antarctic continent and no to minor glaciation on the NH. The small variations in ice volume lead to a hard to define climate sensitivity, which also applies to the PD situation, as relative small changes in ice volume are occurring on Greenland and Antarctica.

4.5 Discussion

With an inverse modelling technique, the benthic δ^{18}O record is divided into an ice-volume and a deep-water temperature contribution. Hence, a continuous record of sea level and deep-water temperature has been reconstructed in coherence with past δ^{18}O variations. In comparison to the standard approach of correcting the benthic record by means of proxy temperature record via Mg/Ca, as done by Sosdian and Rosenthal (2009) for example, inconsistencies with the original data can arise. In the

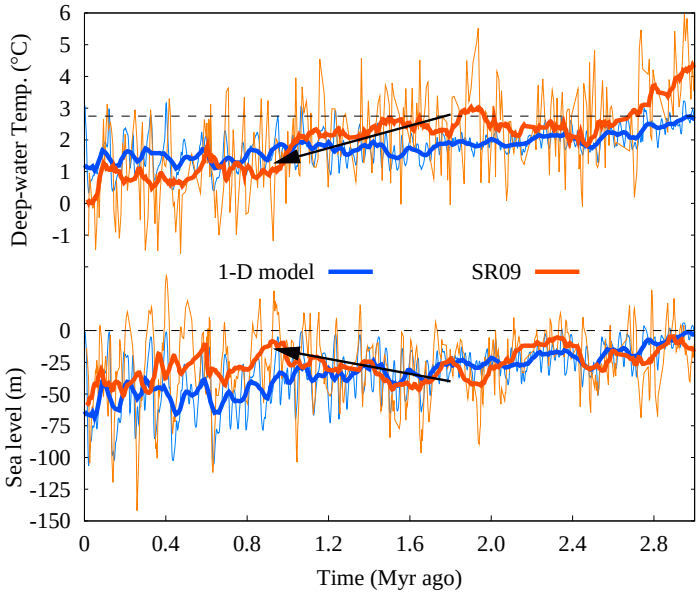

Figure 4.5 | *Comparison with Mg/Ca reconstruction.* *A comparison between the 1-D model reconstructions (blue) and the Mg/Ca derived deep-water temperature and sea-level curves of Sosdian and Rosenthal (2009), indicated by SR09 (red/orange). Top, absolute deep-water temperatures (dashed line indicated PD value of 2.76 °C), and bottom sea level relative to PD. Arrows indicate trend in SR09, thick lines represent a 30-point average (SR09) and an 80-kyr running mean (1-D model)*

study of Sosdian and Rosenthal (2009), deep-water temperature is calculated from the Mg/Ca data, from which a δ_w record is derived with the paleotemperature equation (Shackleton, 1974). Next, a constant value for the δ_w to sea-level ratio is used, as included in Table 4.2, to derive a sea-level record.

Fig. 4.5 shows a comparison of the Sosdian and Rosenthal (2009) data (in orange) with the 1-D ice-sheet modelling results (in blue) over the past 3 Myr. Although the derived temperature record appears to be quite consistent with the 1-D model reconstruction and other observations (Dekens et al., 2008; Etourneau et al., 2009; Herbert et al., 2010), i.e. a downward trend over the Plio-Pleistocene, the reconstructed sea-level curve is inconsistent with the changes in deep-water temperature. As indicated with the black arrows, a decrease in bottom-water temperatures coincides with a gradual rise in sea level, counterintuitive to what should be expected from a decrease in temperature and to what is shown by the 1-D modelling results. Although in the study of Sosdian and Rosenthal (2009) regional records of Mg/Ca and benthic δ^{18}O have been used, whereas here a global stack is used as forcing, the inconsistency between temperature and ice volume is quite substantial.

Other studies calculated a δ_w to sea-level ratio based on ice volume and $\delta^{18}O_i$ estimates (Duplessy et al., 2002; Sima et al., 2006; Langebroek et al., 2010). In coherence with the mass-conservation equation (4.2), these studies used a similar formula to deduce changes in δ_w relative to a certain reference state (e.g. $\delta_w = 0$), whereas here the δ_w value for no ice is used as reference, calculated from the contribution of the PD existing ice sheets. In addition, Table 4.2 also shows ratios based on a comparison of sea level and δ^{18}O data (Chappell and Shackleton, 1986; Fairbanks, 1989; Waelbroeck et al., 2002). Regardless of the method used, the ratios shown in Table 4.2 are quite comparable with each other and fall within the range of the model results (see Fig. 4.3a). However, using a constant ratio can have quite an influence on modelling results, as is clearly presented in Fig. 4.3b and affecting, for example, the results presented in Fig. 4.4, leading to a much less pronounced, and shorter, transitional period between 5 and 13 Myr ago (not shown). Accordingly, the importance of using a self-consistent method for separating the benthic δ^{18}O signal is evident, as is shown in Fig. 4.3 and 4.5. It is clear that a constant value can lead to significant inconsistencies between the data for certain periods of time, and consequently might lead to inaccurate interpretations.

Table 4.3 | *Stnd. dev. and averaged error estimates from the sensitivity tests.*

Variable	σ	max	min
ΔT_{NH}(°C)	2.426	2.035	-4.805
Sea level (m)	8.283	7.936	-15.117

4.5.1 Model uncertainty

Naturally, there is some uncertainty in both the reconstructed temperature and sea level shown in Fig. 4.1, as was already shown in Section 3.3.4, where sensitivity tests were performed on the coupling between deep-water and surface-air temperature (range 0.15 to 0.25), and on the implied difference between the NH and Antarctic ice sheets (range: 6-14 K for EAIS, range: 2-10 K for WAIS). Additionally, in Section 4.3 the model uncertainty regarding the PD $\delta^{18}O_i$ of the Greenland and Antarctic ice sheets has been investigated (range from -43, -32, -28 to -55, -42, -36‰ respectively for EAIS, WAIS and GrIS). These sensitivity experiments show that despite the uncertainty in these parameterisations, the general variability, i.e. the transient nature, of both temperature and sea level remains intact, and therefore these parameterisations are not crucial for the 1-D ice-sheet model results.

As can be seen in Fig. 4.6, which shows the error margin determined from all eight sensitivity tests, the error range for both sea level (in blue) and temperature (in green) varies quite significantly. The differences between the several tests is quite

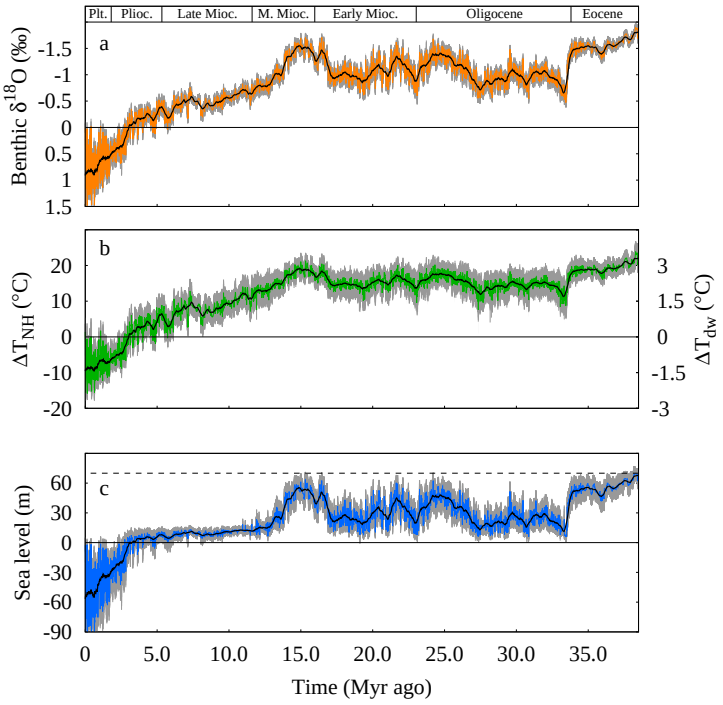

Figure 4.6 | *Error estimates of the 1-D model reconstruction.* *Error estimates from sensitivity tests presented in Sections 3.3.4 and 4.3. From top to bottom, benthic $\delta^{18}O$ data (orange; Zachos et al., 2008), temperature (green) and sea level (blue). black lines indicate the 400-kyr running mean of the standard result, grey shading are the minimum and maximum values, in case of the $\delta^{18}O$ showing the range of experiment C in Section 3.3.4.*

pronounced for certain periods, such as the Eocene and mid to late Miocene, both related to differences in Antarctic ice volume. On average the differences, as shown in Table 4.3, are similar that those reported earlier in Table 3.4, from which was already shown that the largest anomalies originate from the error estimate in the benthic $\delta^{18}O$ forcing.

Since the largest errors arise from deviations in the benthic $\delta^{18}O$ record, it is clear that the modelling results highly depend on the forcing record itself. Naturally the modelling results are tuned such that the tuning targets are met, as shown in Chapter 3, Table 3.3. To test this dependency, the model has been forced with another benthic $\delta^{18}O$ compilation, composed by Cramer et al. (2009). First and foremost, this compilation combines different records of benthic $\delta^{18}O$ in a more consistent manner relative to the Zachos et al. (2008) record, taking into account differences between the separate ocean basins. Furthermore, all model parameters were left unchanged, except

for the deep-water to surface-air temperature scaling λ_{dw}, equation 3.5, which was set to 0.20. As can be seen in Fig. 4.7a, the differences between Zachos et al. (2008) (in red) and Cramer et al. (2009) (in blue), both shown relative to PD, are predominantly pronounced in the Middle to Late Miocene. Most importantly, the higher values of the Cramer et al. (2009) record in the Miocene lead to a larger difference with the benthic δ^{18}O values found at the E-O transition ($\sim$34 Myr ago), thus resulting in lower temperatures and more ice volume. Clearly, the use of a different stack of benthic δ^{18}O results in quite significant differences in both ice volume and temperature. Similar to the other sensitivity results shown in Fig. 4.6, the transient nature of the results remains intact nonetheless.

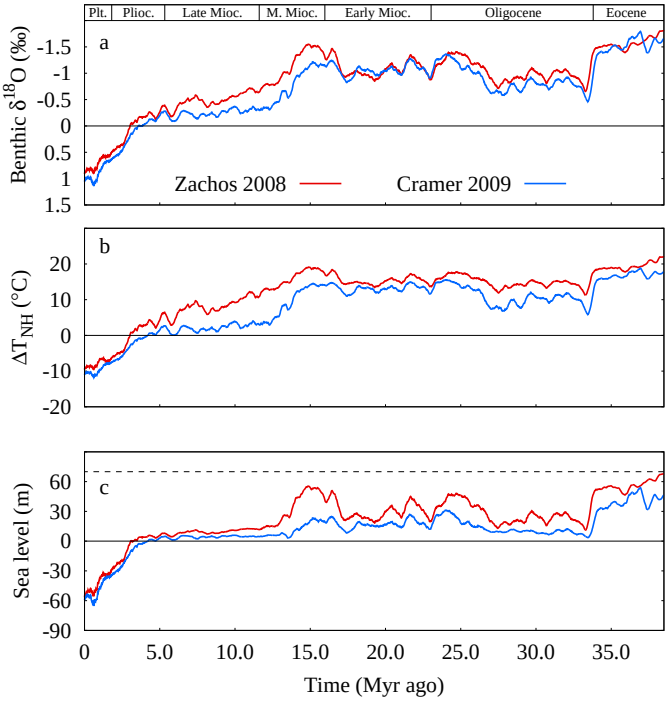

Figure 4.7 | *Comparison of different benthic δ^{18}O forcing records.* *Reconstructions of the model with two different benthic δ^{18}O records, Zachos et al. (2008) (red) and Cramer et al. (2009) (blue). From top to bottom, benthic δ^{18}O data, temperature and sea level. Data is shown as the 400-kyr running mean.*

4.6 Conclusions

The transient nature of the Earth's climate is nicely illustrated in Fig. 4.4, which shows the ice volume response to temperature change over the past 40 Myr. Clearly, the response of the AIS is the dominant signal over the larger part of the Cenozoic, for which the magnitude is similar to the response of the combined NH-dominated response during the past 3 Myr. One distinct period that emerges from this picture is the Mid to Late Miocene (5-13 Myr ago), representing the transitional period from Antarctic to NH glaciation, during which the modelled AIS has reached its maximum size and no glaciation has initiated yet on the NH. Similar to the PD situation, the climate sensitivity of ice volume for temperature changes is hard to define due to small variations in ice volume relative to the change in temperature. For this reason, the PD climate along with the period from 5 to 13 Myr ago show a certain analogue, with lower sensitivity of ice volume to temperature than the rest of the past 40 Myr.

This work shows that it is highly important to try to resolve paleoclimate proxies within the context of transient model simulations, in order to include the physical mechanisms which drive the climate changes. The use of inverse methods, combining physical modelling with paleoclimate proxies, can potentially yield greater understanding than separate analysis of ambiguous proxy records or forward modelling alone.

5

Reconstruction of a continuous high-resolution CO_2 record over the past 20 million years

The gradual cooling of the climate during the Cenozoic has generally been attributed to a decrease in CO_2 concentration in the atmosphere. The lack of transient climate models and in particular the lack of high-resolution proxy records of CO_2 beyond the ice-core record prohibit however a full understanding of for example the inception of the Northern Hemisphere glaciation and mid-Pleistocene transition. In this chapter, the modelled temperature record is compared with ice core and proxy-derived CO_2 data to create a continuous CO_2 reconstruction over the past 20 million years. Results show a gradual decline from 450 ppmv around 15 million years ago to 225 ppmv for mean conditions of the glacial-interglacial cycles of the last 1 million years, coinciding with a gradual cooling of the Northern Hemisphere land temperatures by approximately 27 °C corresponding to a global surface cooling of 10 °C. Between 13 to 3 million years ago there is no long term sea level variation caused by ice-volume changes. No evidence is found for a change in the long-term relation between temperature change and CO_2, other than the effect following from the saturation of the absorption bands for CO_2. The reconstructed CO_2 record shows that the Northern Hemisphere glaciation starts once the long-term average CO_2 concentration drops below 265 ppmv after a period of strong decrease in CO_2. Finally, only a small long-term decline of 23 ppmv is found during the mid-Pleistocene transition, constraining theories on this major transition in the climate system. The approach is not accurate enough to revise current ideas about climate sensitivity.

This chapter is based on:
Van de Wal, R. S. W., B. de Boer, L. J. Lourens, P. Köhler and R. Bintanja, Reconstruction of a continuous high-resolution CO_2 record over the past 20 million years, *Climate of the Past*, **7**(4), 1459-1469, 2011.

5.1 Introduction

The overall climate cooling reconstructed for the past 20 Myr has generally been attributed to a change in CO_2 concentration in the atmosphere (Ruddiman, 2003; Zachos et al., 2008), although the amount of CO_2 decrease and the amplitude of subsequent cooling are discussed widely (Jansen et al., 2007). Since data and modelling studies covering this time period are poorly integrated, the understanding of the inception of ice ages in the Northern Hemisphere (NH) (Raymo, 1994), as well as the mechanisms causing the transition from 41,000-year to 100,000-year dominated climate cycles, the Mid-Pleistocene Transition (MPT) (Tziperman and Gildor, 2003; Clark et al., 2006; Huybers, 2007; Bintanja and Van de Wal, 2008), that occurred without apparent changes in the insolation forcing (Hays et al., 1976; Imbrie and Imbrie, 1980) is still incomplete. Current difficulties in assessing the role of CO_2 on the long timescales are the lack of reliable CO_2 data from the pre ice-core record (Ruddiman, 2010), and the limited data of sea level (Miller et al., 2005; Müller et al., 2008) and temperature. Current knowledge on long-term climate variability builds on the Milankovitch theory of solar insolation variability (Milankovitch, 1930), including scenarios that rely on highly parameterised non-linear response mechanisms to the insolation forcing.

The 1-D ice-sheet model temperature reconstruction introduced in Chapter 3 based on the interpretation of marine benthic $\delta^{18}O$ records and new CO_2 proxies allow us to reassess this understanding and to present a global overview of temperature, sea level and CO_2 changes over time. In this chapter, the NH air temperature (ΔT_{NH}) relative to present day, which gives an estimate of the air temperatures at sea level in areas where the NH ice sheets developed (40°- 80°N), is used to reconstruct a continuous CO_2 record over the past 20 Myr.

For this purpose, the ΔT_{NH} record is compared with existing proxies for CO_2, first for the past 800,000 years using primarily ice-core CO_2 data (Petit et al., 1999; Siegenthaler et al., 2005; Lüthi et al., 2008), and secondly with geochemical and stomata-derived CO_2 proxy data for the older time interval (Tripati et al., 2009; Kürschner et al., 1996, 2008; Retallack, 2009; Pearson and Palmer, 2000; Hönisch et al., 2009; Pagani et al., 2005, 2010; Seki et al., 2010). Through this comparison, a regression coefficient between temperature and CO_2 could be determined that allowed us to reconstruct a global mutually self-consistent and continuous overview of temperature, sea level and CO_2 over the past 20 Myr. Eventually the paper is concluded by a discussion on climate sensitivity following from the results.

5.2 Results in terms of sea level and temperature trends

Although the sea level and temperature reconstructions have been widely discussed in the previous two chapters, their main characteristics are repeated here in purpose

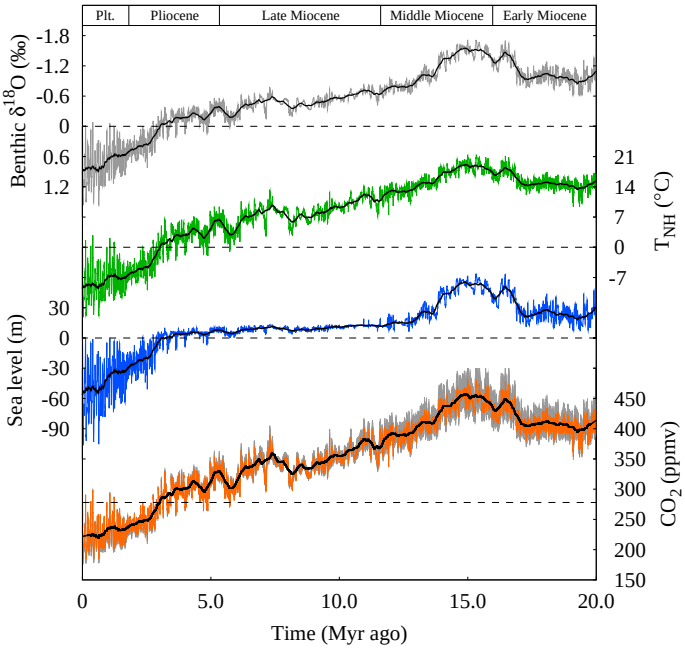

Figure 5.1 | *Records of key climate variables over the last 20 Myr.* *From top to bottom, forcing of the model are changes in the stacked benthic $\delta^{18}O$ record with respect to pre-industrial times (grey, Zachos et al. (2008)). Output is a consistent record for the Northern Hemisphere temperature change with respect to pre-industrial conditions (green) and sea level (blue). The reconstructed CO_2 record (orange) is obtained by inverting the relation between NH temperatures and CO_2 data. The thick black lines represent 400-kyr running mean. Grey shading in the lower plot indicates the standard deviation due to model and data input errors.*

of their relation to CO_2 variability. The model-based deconvolution shows a long-term decrease in ΔT_{NH} by 27 °C since the Miocene (about 10 °C in the global surface temperature) with superimposed orbitally forced changes (green curve in Fig. 5.1). Eustatic sea level, more strictly sea level from ice-volume changes only, gradually falls, but is roughly constant from 13 Myr ago (+15 m) to 3 Myr ago (+5 m) as the ice sheets in the SH are full grown and major ice sheets in the NH are not yet developed (blue curve in Fig. 5.1). Moreover, the deviation of the sea level changes from the 400 kyr running mean revealed only low amplitude sea level changes of 10 m during this time period, whereas it fluctuated up to ±20 m prior to 13 Myr ago and up to ±66 m after 3 Myr ago. Maximum sea level high-stand of +55 m occurred around 15 Myr ago, probably caused by a reduced EAIS (see also Chapter 3).

Fig. 5.2 shows that there is not a unique solution for sea level given a certain temperature. This results from the different timescales in the coupled system of ice sheets, changing deep-water temperatures, surface temperatures, bedrock adjustment,

and forcing and feedbacks of the mass balance height and albedo-temperature feedback. Obviously, sea level rises on average with temperature, for which the total sea level change (black line) is 6 m per °C temperature change. Close to present-day temperatures, i.e. -2 °C < ΔT_{NH} < +10 °C, only the GrIS and WAIS change in size. This results in only minor sea level fluctuations, which are approximately 5 times lower compared to warm or cold conditions, expressed per °C temperature change. During warmer (ΔT_{NH} > +10 °C) and colder climates (ΔT_{NH} < -2 °C), sea level changes are stronger due to variations in the size of the NaIS, EuIS and EAIS, for colder climates, the NaIS, EuIS, and GrIS are vulnerable to changing temperature, whereas the WAIS and EAIS are sensitive to temperature changes during warmer climates. The total sea level sensitivity to temperature change is approximately similar for warm and cold climates as indicated by the black line in Fig. 5.2 and shown in Fig. 4.4, around 7 m $°C^{-1}$. Also on the level of an individual ice sheet, transient effects impede a simple and unique solution between temperature and sea level, which implies that inverting climate information from sea level, has to be considered with great care.

In contrast to the sea level record, temperature shows a more gradual decline from the Miocene maximum around 15 Myr ago to the start of the major glaciation in the

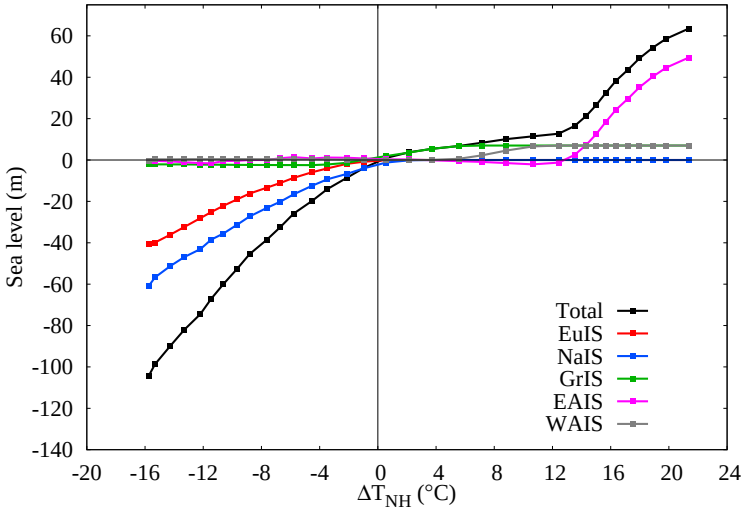

Figure 5.2 | *Sea level equivalent ice volume relative to temperature.* *The response in meters sea level equivalent ice volume of the five individual ice sheets relative to temperature shown for the EuIS (red), the NaIS (blue), the GrIS (green), the EAIS (orange), the WAIS (grey) and total ice volume (black). Sea level and temperature are averaged from the transient simulations, similar to Fig. 3.5, all values are relative to the present-day ice volume, for the GrIS and WAIS set to 7 m s.e. and for the EAIS set to 56 m. Note the strong transient and nonlinear response for each ice sheet. Results are adopted from Chapter 3.*

NH around 3 Myr ago (Fig. 5.1). The gradual increase in the benthic δ^{18}O record leads to a long-term cooling of the climate between 13 and 3 Myr ago. The amplitude of temperature and sea level variability both increase once the major ice sheets develop in the NH around 3 Myr ago. As has been shown in the previous chapters, many tests have been performed with the model to assess the uncertainties in the input and model parameters on sea level and temperature results. The most important tests allow us to estimate the uncertainty range as displayed in Fig. 4.6 at the end of Chapter 4. For the δ^{18}O input the uncertainty was determined to be 0.16‰, which is derived from the root mean squared difference between the smoothed marine record and the actual data points. The key model parameters contributing to the uncertainty are: (1) the deep-water to surface-air temperature coefficient, (2) the temperature difference between ΔT_{NH} and the temperatures on Antarctica, and (3) the isotopic content of the ice sheets. For the three model parameters, maximum and minimum values are used to test the effect on modelled temperature and sea level. The resulting standard deviation varies over time, but is on average 2.4 °C for temperature and 8.3 m for sea level over the past 20 Myr, as shown in Table 4.3. In order to interpret the results one has to bear in mind that the reconstructed temperatures are strictly only valid in the continental areas of the NH where ice sheets develop (about 40°- 80°N), implying that they are therefore not a representative for the entire globe. A relationship between ΔT_{NH} and the global temperature anomaly ΔT_g is developed later on.

5.3 Reconstruction of CO_2

In order to get a consistent CO_2 record, the relation between temperature and proxy CO_2 records is investigated based on B/Ca ratio (Tripati et al., 2009), δ^{11}B (Pearson and Palmer, 2000; Hönisch et al., 2009), alkenones (Pagani et al., 2005, 2010), a combination of alkenones and δ^{11}B (Seki et al., 2010), stomata (Kürschner et al., 1996, 2008; Retallack, 2009) and ice cores (Petit et al., 1999; Siegenthaler et al., 2005; Lüthi et al., 2008), all shown in Fig. 5.3. The paleosol record presented by Beerling and Royer (2011) has not been taken into account because of their large uncertainty. All data points are representative for different discrete time intervals, with obviously a bias towards the more modern data points, and each having its advantages and drawbacks. For example, the boron isotope derived estimates of the CO_2 concentration are based on the fact that higher atmospheric concentrations lead to more dissolved CO_2 in the surface ocean, which causes a reduction in the pH of the ocean.

As the pH can be derived from measurements of the δ^{11}B of calcium carbonate (Pearson and Palmer, 2000), CO_2 can be calculated provided that another parameter of the marine carbonate system (e.g. alkalinity) is known (Zeebe and Wolf-Gladrow, 2001). The method is expensive, time consuming, and only well-preserved foraminiferal specimen are suitable for the analysis, resulting in only low-resolution

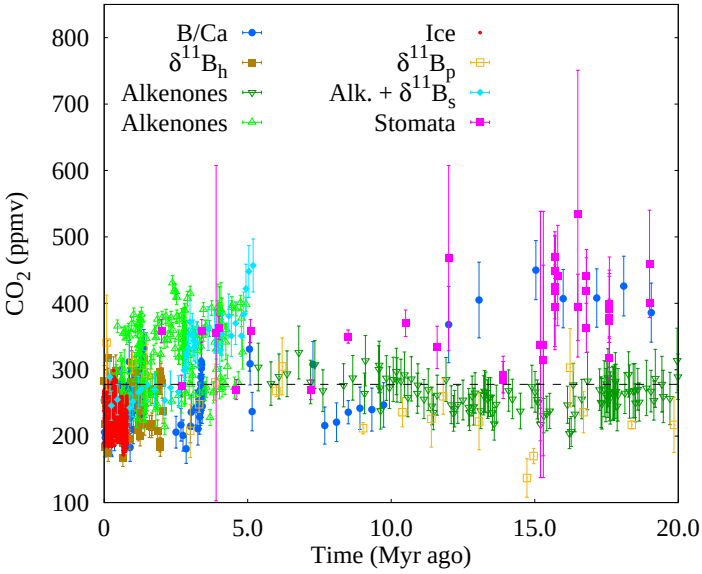

Figure 5.3 | *CO_2 records as a function of time.* *The different CO_2 records plotted together, indicating the inhomogeneous distribution in amount and range for the different proxies. Data are B/Ca (Tripati et al., 2009), stomata data (Kürschner et al., 1996, 2008; Retallack, 2009), alkenones with $\delta^{11}B_s$ (Seki et al., 2010), $\delta^{11}B_p$ (Pearson and Palmer, 2000), $\delta^{11}B_h$ (Hönisch et al., 2009), alkenones (Pagani et al., 2005, 2010) and ice (Petit et al., 1999; Siegenthaler et al., 2005; Lüthi et al., 2008). The symbols and colours for the different proxies are similar in all figures. Alkenone data by Pagani et al. (2005, 2010) are treated as two different datasets in order to test whether one of the two could be used for further analysis.*

records up to now. Ice cores provide the most robust and high-resolution CO_2 archive as they directly preserve the atmospheric concentrations, but only for the past 800,000 years (Lüthi et al., 2008). Here, all data are accepted as they are published without any further correction. The general picture is that the scatter in the different approaches is large, but there is a tendency for higher CO_2 values in the early Cenozoic (Ruddiman, 2003; Zachos et al., 2008), with ambiguous results for the last 20 Myr. Moreover none of the proxies has a continuous record for the last 20 Myr (Fig. 5.3). For this reason there is a need to compile all available records in a consistent manner. The decomposition of the marine benthic $\delta^{18}O$ record offers a framework to do so.

The modelled temperature is used as a tool to select mutually consistent CO_2 records by assuming that there is a relation between CO_2 and ΔT_{NH}, which is comparable to the relation found in ice cores. In fact this is justified as several independent proxies do show a similar linear relation (Fig. 5.4). Different methodologies may explain why the $\delta^{11}B_h$ ($\delta^{11}B$ from Hönisch et al. (2009)) is more consistent with the ice cores CO_2 data then the $\delta^{11}B_p$ ($\delta^{11}B$ from Pearson and Palmer (2000)). Hönisch

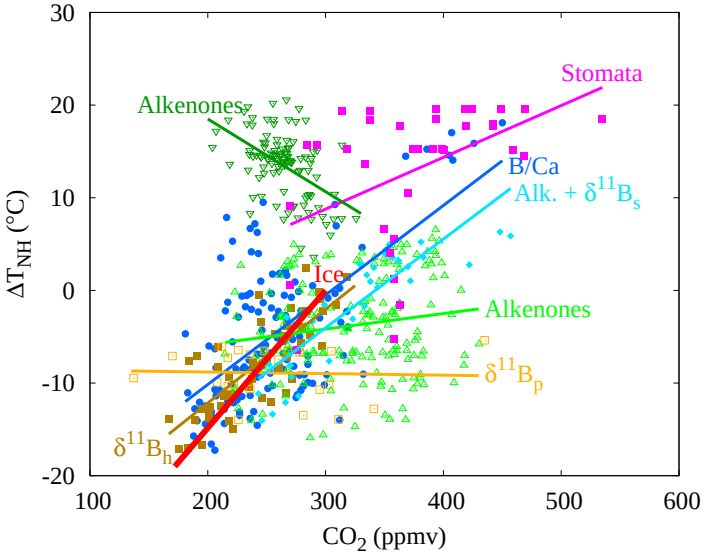

Figure 5.4 | *Scatter plot of the different CO_2 proxies vs. temperature*. *The CO_2 proxies are plotted as a function of the reconstructed temperature derived from the benthic $\delta^{18}O$ record as shown in Fig. 5.1. Only records with filled symbols $\delta^{11}B_h$ (Hönisch et al., 2009), B//Ca (Tripati et al., 2009), alkenones + $\delta^{11}B_s$ (Seki et al., 2010), stomata data (Kürschner et al., 1996, 2008), and the ice-core record (Petit et al., 1999; Siegenthaler et al., 2005; Lüthi et al., 2008) are used for further analysis. For reasons of transparency CO_2 is plotted in ppmv. If CO_2 would be plotted as $\ln(CO_2/CO_{2,ref})$ a similar picture emerges. The latter is physically more consistent as it takes the saturation of the absorption bands into account.*

et al. (2009) selected samples around glacial and interglacial extremes, which was not done by Pearson and Palmer (2000). In addition, it has been argued that the Pearson and Palmer (2000) data need to be rejected for reasons related to diagenesis, use of incorrect fractionation factors, and poor modelling of seawater alkalinity and $\delta^{11}B$ (Foster et al., 2006). The comparison in Fig. 5.4 reveals that the CO_2 estimates derived from the ice cores, B/Ca, stomata, $\delta^{11}B_h$ and the combination of alkenones and $\delta^{11}B_s$ ($\delta^{11}B$ from Seki et al. (2010)) are mutually consistent, because they reveal similar slopes, whereas the $\delta^{11}B_p$, and alkenones-derived CO_2 estimates do not show a consistency with the ice-core record.

Hence, only the consistent records are selected to derive an empirical relationship between temperature and CO_2. This relation is used to calculate CO_2 from the reconstructed ΔT_{NH} in order to generate a continuous CO_2 proxy series that is mutually consistent with the benthic $\delta^{18}O$ record. The application of the correlation between CO_2 and temperature implies, however, that the regression needs to cover the temperature range as shown in Fig. 5.1 without having too much bias to the data-rich cold

climate state. For this reason, the CO_2 observations are binned in intervals of 1 °C NH temperature change, for which results are shown in Fig. 5.5. The temperature records are running averages over 2000 years, in order to prevent outliers due to a mismatch in dating of the CO_2 proxy and the benthic record. Furthermore, several tests have been performed to weigh the different accepted CO_2 proxies, by uncertainty in modelled temperature and measured CO_2. In addition, the effect of the binning size and averaging period is tested, which contribute to the uncertainty in the reconstructed CO_2. Omitting one of the proxies affects the end result by at most 6% (B/Ca data) in the slope between $\ln(CO_2/CO_{2,ref})$. Based on all these tests, the uncertainty is estimated to be 10% in the slope between $\ln(CO_2/CO_{2,ref})$ and ΔT_{NH} around a central value of 39 °C. A log-linear regression between ΔT_{NH} and CO_2 is used because of the saturation of the absorption bands for CO_2 (Myhre et al., 1998). Accordingly, the CO_2 record as presented in Fig. 5.1 has an uncertainty of 20 ppmv for cold climates and up to 45 ppmv for warm climates. The larger uncertainty for warmer climates is due to the logarithmic relation between CO_2 and temperature.

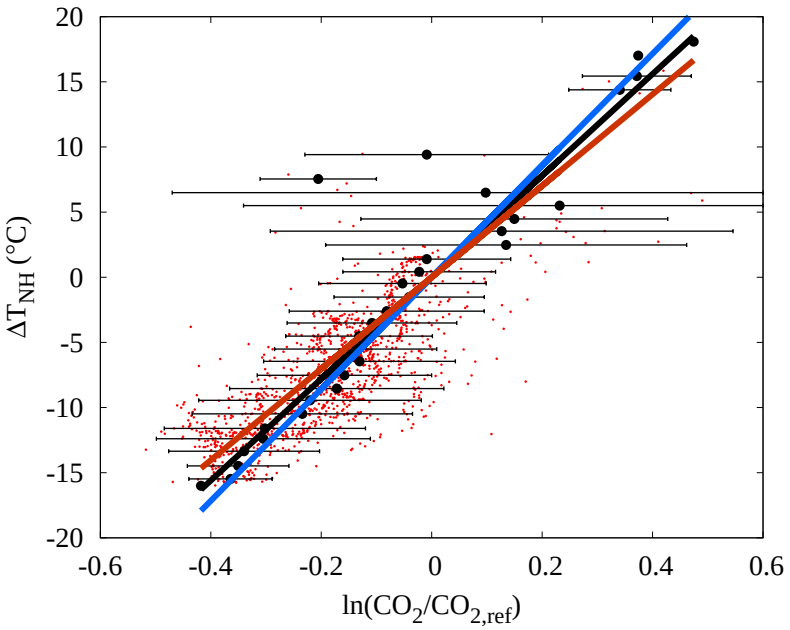

Figure 5.5 | *Selected CO_2 data vs. temperature*. *The selected (n = 1302) proxy CO_2 data (red dots) binned in intervals of 1 °C NH temperature change. The error bars represent one standard deviation variability of the data in the selected temperature interval. The additional lines show the range in C values from different weighing tests, blue: C +10% and red: C -10%. The slope of the regression line corresponding to C is 39 °C.*

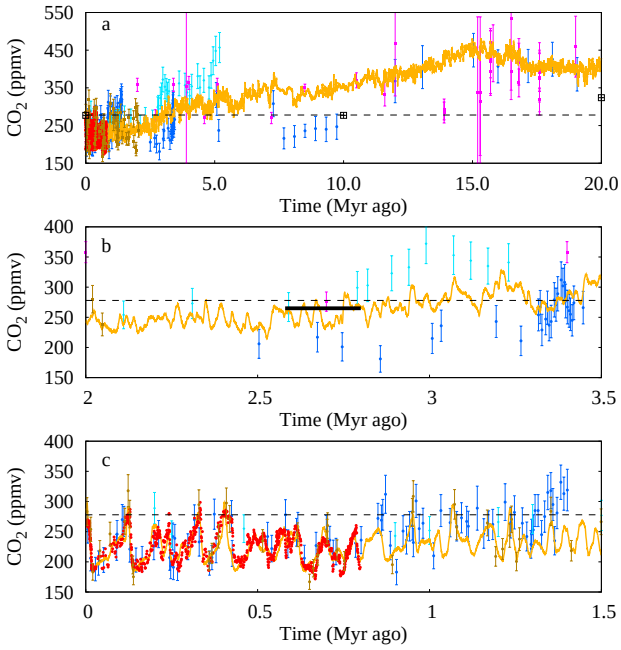

Figure 5.6 | *CO_2 reconstruction with proxy records.*. *Comparison of reconstructed CO_2 record (orange) with C = 39 °C, with proxy records (symbols as in Fig. 5.3). Panel a) for the full 20 Myr period, b) for the period around the Northern Hemisphere glacial inception and c) for the mid-Pleistocene transition. Note that the vertical scale is different for the different panels. The horizontal bar in panel b) indicates the onset of major glaciation in the Northern Hemisphere. The crosses with open squares in panel a) are the GEOCARB data (Berner, 1994).*

Over the past 800 kyr the reconstructed CO_2 record is in good agreement with the ice-core record, as shown in Fig. 5.6c, which is, however, input to the reconstruction and therefore not an independent result. Over the mid-Pleistocene transition (defined here from 1.5 to 0.5 Myr ago), the results indicate a gradual decline of about 23 ppmv, and at the same time an increase in the amplitude. Carbon-cycle simulation results over the last 2 Myr across the Mid-Pleistocene Transition (Köhler and Bintanja, 2008) support the change in amplitude, but suggest stable glacial CO_2 values and reduced interglacial CO_2. It is also unclear why the combined $\delta^{11}B$ and alkenone record is higher than the reconstruction for the last 1.5 Myr. Around 10 Myr ago the B/Ca data measured on planktonic foraminifera indicate much lower CO_2 concentrations, in fact more in line with the GEOCARB (carbon-cycle model Berner, 1994) estimates (see Fig. 5.6a). Ultimately this implies an inconsistency between benthic $\delta^{18}O$ reconstructions and B/Ca. The difference is too large to be attributed to model uncertainties.

5.4 Long-term knowledge on climate sensitivity

Since a continuous record of ΔT_{NH} and CO_2 has been obtained, the long-term climate sensitivity can be investigated in more detail. There are various ways to define climate sensitivity. Here, climate sensitivity (S) is defined as the functional dependency of changes in global surface temperature (ΔT_g) on CO_2, thus ΔT_g = f(CO_2). It is calculated from the radiative forcing (ΔR) caused by changes in CO_2, other greenhouse gases, and various fast and slow feedbacks (f), which will be specified below. A general formulation for the global temperature is:

$$\Delta T_g = S\frac{\Delta R}{1-f}. \tag{5.1}$$

In this general setting, changes in CO_2 might be the cause for climate change, thus represent the forcing term ΔR or a feedback. A functional relationship between the global temperature and CO_2 can subsequently be developed, assuming that CO_2 is causing the radiative imbalance, ΔR = f(CO_2), while the initial perturbation of this imbalance might be caused by other processes. This by no means implies that changes in CO_2 were always the driver for climate change over the last 20 Myr, but it is used to derive a functional relationship between ΔT_g and CO_2. The opposite procedure (forcing by other processes and feedbacks by CO_2) is certainly a valid option, but for reasons of simplicity only one of the two possible calculations is used here. From radiative transfer theory it is known that due to the saturation of the absorption bands, a logarithmic relationship has to be applied for the radiative forcing of CO_2:

$$\Delta R = \beta ln\left(\frac{CO_2}{CO_{2,ref}}\right), \tag{5.2}$$

where ΔR is the radiative forcing in W m^{-2}, and β is estimated to be 5.35 W m^{-2} (Myhre et al., 1998). This implies a radiative forcing of -2.4 W m^{-2} for the observed changes in CO_2 from the LGM to present-day, and +3.7 W m^{-2} for a doubling of CO_2, with $CO_{2,ref}$ = 278 ppmv, the pre-industrial level. Non-CO_2 greenhouse gases like CH_4 and N_2O enhance this direct radiative forcing of CO_2. Hence, for the last 800 kyr this enhancement was about 30% (Köhler et al., 2010), which is represented by γ = 1.3. The sensitivity S of the climate system to external forcing is typically described by the Charney sensitivity S_c (Charney et al., 1979), which includes the fast feedbacks of the system (water vapour, lapse rate, albedo, snow and sea ice, clouds). It is the quantity usually calculated by coupled ocean-atmosphere models. Here, a sensitivity S_p derived from paleo data of 0.72 °C / (W m^{-2}) (Köhler et al., 2010) is used. It is based on a LGM cooling of $\Delta T_{g,LGM}$ = -5.8 °C (Schneider von Deimling et al., 2006), and a total radiative forcing ΔR_{LGM} = -9.5 W m^{-2} (Köhler et al., 2010)

The total forcing of the system (ΔR') includes the forcing ΔR caused by all greenhouse gases, which is amplified by a feedback factor f consisting of the slow feedbacks not included in S_p. It represents the feedbacks from albedo changes caused by land ice, vegetation and dust:

$$\Delta R' = \frac{\gamma \Delta R}{1-f} \tag{5.3}$$

For the last 800 kyr, a value for f = 0.71 and γ = 1.3 is derived from proxy-based evidence (Köhler et al., 2010). For ΔT_{NH} a value of -15.8 °C averaged over the period 23 to 19 kyr BP (LGM) is obtained, which is 2.7 times larger than the global temperature change of -5.8 °C. This is in line with estimates of the polar amplification factor (α) from a GCM model of 2.5-3 by Singarayer and Valdes (2010). The final expression for the change of ΔT_{NH} can now be written as:

$$\Delta T_{NH} = C ln\left(\frac{CO_2}{CO_{2,ref}}\right), \tag{5.4}$$

with,

$$C = \frac{\alpha \beta \gamma S_p}{1-f}. \tag{5.5}$$

Calculation of C (α = 2.7, β = 5.35, γ = 1.3, S_p = 0.72, f = 0.71 and $CO_{2,ref}$ = 278 ppm) results in an indicative value of 47.0 °C for cold conditions (i.e., past 800,000 years) as f is based on LGM proxy data. Where it might be noted that application of $CO_{2,ref}$ = 278 ppmv implies that ΔT_{NH} is expressed relative to pre-industrial levels. This calculated value for C is, however, considerable larger than the 39 ± 3.9 °C that was found for the slope between $\ln(CO_2/CO_{2,ref})$ and ΔT_{NH} over the past 20 Myr as shown in Fig. 5.5. Remarkably enough Fig. 5.5 does not indicate that C depends on the CO_2 concentration itself. One might expect f to be smaller for warmer conditions, but this is apparently compensated by a change in one of the other parameters, likely the polar amplification factor α. From Fig. 5.5 it is clear that the scatter for warmer conditions is large and we have to await more proxy data for warmer conditions to see whether this log-linear relation holds. A source of uncertainty is the value for S_p, which is derived from LGM conditions. Hargreaves et al. (2007) argued that this value is 15% smaller than the value for 2×CO_2, close to the derived values for the early Miocene climatic optimum. A similar change in the sensitivity implies that C would decrease to a value of 40.0 °C, which is well within the uncertainty of the estimated value for C of 39 ± 3.9 °C derived from Fig. 5.5.

Another source of uncertainty in this analysis is probably the assumption that the polar amplification factor, α, is constant over time. Theories and observations on much warmer climate states suggest a decrease in the meridional temperature gradient (e.g. Huber and Caballero, 2011) implying a decrease in α. The fact that C does not

vary with increased temperature suggests that a possible change in α or the long-term feedbacks compensate one another. The applied method does not allow separating α from the long-term feedbacks or the GHG forcing. In theory, if α were much smaller for warmer climate conditions and f smaller, it would imply that considerably higher CO_2 concentrations in the past are necessary to explain the temperatures derived from the benthic $\delta^{18}O$ record. However, the stomata-derived CO_2 data, the GEOCARB data (Berner, 1994), and the B/Ca data do not indicate much higher CO_2 concentrations, at least not over the period considered here, suggesting that this theoretical example is not likely.

Too little information is available to attribute individual changes in the parameters over 20 Myr. But given the fact that the fitted value of C based on the presented data in this chapter, and the estimated value of C based on the knowledge of the system (Köhler et al., 2010) are close to each other, implies that the combined effect of the key processes affecting benthic $\delta^{18}O$ records, temperature and CO_2 are incorporated sufficiently accurately for at least the period that there is ice on Earth. The implication of equations (5.4) and (5.5) is that systematic errors in the various components can cancel each other very easily, complicating the interpretation of the sensitivity. A 20% increase in α can be compensated by a 20% decrease in β, γ or S_p, or an equally large increase of (1-f). As we determine C directly from the model inversion one cannot expect improved insights in the different values for in α, β, γ, S_p or f from the methodology used here. The fact that the values used in the literature eventually lead to a similar value for C merely indicates that there is no reason to adjust literature values for climate sensitivity based on the inversion used here.

To set the approach used here into context with existing calculations of climate sensitivity one might simply calculate the pure Charney climate sensitivity out of equations (5.1), (5.4) and (5.5) by choosing $f = 0$ (no slow feedbacks of ice sheets and vegetation) and $\gamma = 1$ (no non-CO_2 GHG), which leads to $C = 7.2$ °C and $\Delta T_g = 2.7$ °C for a CO_2 doubling. This is close to the original value and well within the uncertainties of 3 ± 1.5 °C (Charney et al., 1979). For the interpretation of the climate sensitivity values one needs to be careful. In order to calculate temperature changes from CO_2 changes as presented in the literature often different feedbacks are included. Here, the feedback factor obtained by Köhler et al. (2010) based on paleo proxy evidence for the LGM is used to show that the obtained value of C is in agreement with estimates of α, β, γ, S_p and the 15% reduction in S_p depending on the climate state as proposed by Hargreaves et al. (2007). Adopting a lower value for f as maybe deduced from Hansen et al. (2008) would indicate that the value for C would be too large. Of course this can be compensated by assuming a larger value for α, implying an even larger meridional temperature gradient, but that seems unlikely. In other words, the temperatures based on the benthic $\delta^{18}O$ records support the feedback factor as derived by Köhler et al. (2010). If this value ($f = 0.71$) is excluded from C to consider

the short-term climate sensitivity to facilitate a more realistic comparison with Hansen et al. (2008), a value for the sensitivity is obtained which is smaller than the sensitivity by Hansen et al. (2008). Furthermore, Hansen et al. (2008) uses in their calculations a global LGM cooling of ΔT_g = -5 °C, while here a temperature anomaly of -5.8 °C is used, which is understood to be best supported by proxy data. This readily explains a similar larger difference of 16% in the projected temperature changes of the two approaches calculated for future climate with doubled CO_2.

5.5 Discussion and Conclusion

Accepting the CO_2 concentration as presented in Fig. 5.1 with all its caveats and limitations, completes the picture of the key climate variables over the last 20 Myr. The figure shows a gradual decline from about 450 ppmv around 15 Myr ago to a mean level during the last 1 Myr of 225 ppmv or a decrease of 225 ppmv. This is about 2.2 times the increase in CO_2 concentration over the last century as well as 2.2 times the range in the ice-core record over the past 800 kyr. If only the ice-core record would have been used, Middle Miocene values of 300 ppmv above present-day level would have been obtained, and the sensitivity would not agree with the analyses presented in the previous paragraph as the sensitivity (C) would decrease to a value as low as 28.5 °C. Hence the application of the inverse model and the stacked binning procedure is crucial for the results.

It should be realised that the result are as good as the input is for the model. To reconstruct the ΔT_{NH}, the widely used benthic δ^{18}O record of Zachos et al. (2008) has been used to force the 1-D model, which has δ^{18}O values during the Middle Miocene that are comparable to the values at the E-O transition. As a consequence the modelled Middle Miocene ice volume is small. As was already shown in Section 4.5, a test with the stacked record by Cramer et al. (2009), which addresses in more detail inter-basin changes of δ^{18}O records, indicate a larger ice volume for the Middle Miocene (see Fig. 4.7. As a consequence temperature and CO_2 changes are different, yielding Middle Miocene CO_2 values of 410 ppm.

The question remains of course what causes these subtle changes in the carbon cycle on the long timescale. In order to answer this question much higher resolution and accuracy of CO_2 records are necessary. The large sensitivity implies that, in contrast to earlier conclusions (Hönisch et al., 2009), subtle changes in CO_2 (possibly internal), may have caused the MPT, when dominant 41-kyr glacial cycles evolved into a dominant 100-kyr rhythm. The results indicate an average change of only 23 ppmv between 1.5 and 0.5 Myr ago, and also an increasing amplitude. This result seems to be more in line with a recent estimate by Lisiecki (2010) based on marine δ^{13}C measurements and the δ^{11}B data by Hönisch et al. (2009) than with the B/Ca derived CO_2 data by Tripati et al. (2009), which indicates a larger change in CO_2 over

the MPT. However, the trend in CO_2 over time is too small given the accuracy of the applied methods to draw firm conclusions on this point.

With respect to the inception of the Northern Hemisphere ice around 2.7 Myr ago the results indicate that the trend in CO_2 before the inception is higher than the average rate of change (see Fig. 5.1), and that the inception takes place once the long-term average concentration drops below 265 $\pm$ 20 ppmv (Fig. 5.6b). So for this climate transition a change in CO_2 seems to be more important than for the mid-Pleistocene transition.

In conclusion, the self-consistency of the approach used here should enable researchers from various disciplines to identify more easily whether new CO_2 proxies are in line with the reconstructed temperature change derived from the $\delta^{18}O$ record and the ice-core derived CO_2, $\delta^{11}B_h$, $\delta^{11}B_s$ + alkenones, B/Ca, and stomata. Various geological processes important during the last 20 Myr such as mountain uplift (e.g. Foster et al., 2010) and changes in the gateways are not considered here. However, for global climate changes CO_2 induced changes dominate as shown by Henrot et al. (2010), who argued based on a model of intermediate complexity that geological processes like mountain building and changes in ocean gateways are of secondary importance for global temperature and cannot explain the proxy reconstructions of the change in temperature within their modelling framework.

As a final remark, it is important to realise that the relation between CO_2 and Northern Hemisphere temperature may change for instance by a changing strength of feedbacks or a different relation between global and Northern Hemisphere temperature changes, and as such it complicates the interpretation of paleo data as analogue for present-day conditions. Paleo data provide the range of natural fluctuations, but the rate of change of key variables is shown to be depending on the state of the system (Köhler et al., 2010), the timescale of interest and the processes at stake, which are not necessarily similar in the past as for present-day climate change. Paleo data should be interpreted in the context of the conditions and forcing prevailing at that time.

Acknowledgements. P. Köhler is funded by PACES, the research program of AWI.

6

An assessment of ice-volume variations over the past 1 million years from inverse 3-D ice-sheet modelling

During the Plio-Pleistocene, sea-level records show strong variability going from one interglacial to the other. On this time scale, sea-level changes are dominated by changes of ice volume on land. Predominantly by the waxing and waning of the large ice sheets on the Northern Hemisphere. However, the separate contributions of ice in the Northern or Southern Hemisphere are not precisely known. In this chapter, a fully coupled system of four 3-D ice-sheet models is used, simulating glaciations on Eurasia, North America, Greenland and Antarctica, explicitly calculating all ice-volume contributions. The ice-sheet models use a combination of the SSA and SIA to determine sheet-shelf and sliding velocities. The model is forced with deep-sea benthic δ^{18}O records over the past 1 million years, and uses an inverse forward modelling approach to reconstruct a self-consistent record of temperature and ice volume. It is shown that for both eustatic sea level and sea water δ^{18}O changes, the Eurasian and North American ice sheets are responsible for the largest part of the variability. The combined contribution of the Antarctic and Greenland ice sheets is about 10% for sea level and about 20% for sea water δ^{18}O during glacial maxima. This chapter describes the first complete simulation of global ice-volume variations over the past million years with the possibility to model changes above and below present-day ice volume, following the observations of benthic δ^{18}O proxy data. Moreover, eustatic sea level is computed from modelled ice volume and serves as an implicit forcing to the ice-sheet models.

This chapter is based on:
De Boer, B., R. S. W. van de Wal, L. J. Lourens, R. Bintanja and T. J. Reerink, An assessment of ice-volume variations over the past 1 million years from inverse 3-D ice-sheet modelling, *in preparation*

6.1 Introduction

Deep-sea sediment records can go back to tens of million years (Lisiecki and Raymo, 2005; Zachos et al., 2008; Cramer et al., 2009). Although there are several climate proxies that can be obtained from such records, benthic δ^{18}O data are well known to present past climate changes in global ice volume and local deep-water temperature (Chappell and Shackleton, 1986). During the Pleistocene, i.e. the past 2.6 million years (Myr), ice volume variations where mainly dominated by large ice sheets in the Northern Hemisphere (NH) (e.g. Bintanja et al., 2005a; Bintanja and Van de Wal, 2008). In the study of Bintanja and Van de Wal (2008), a 3-D ice-sheet model combined with an inverse forward modelling approach is used to obtain temperature and ice volume consistent with the benthic δ^{18}O LR04 stack (Lisiecki and Raymo, 2005) over the past 3 Myr.

In their study, two ice-sheet models are used to reconstruct the ice sheets in Eurasia and North America, which are largely representative for the sea level and temperature fluctuations during the past 3 Myr. To compensate for the changes of the Greenland and Antarctic ice sheets, the sea-level contribution of the NH ice sheets was assumed to be 85% of the total sea-level change. Similarly, the contribution to seawater δ^{18}O (δ_w) variations was estimated at 95% (Bintanja et al., 2005a). In this Chapter, this research will be extended by coupling a newly developed 3-D ice-sheet model to the inverse model, performing experiments with all four major ice-sheets combined. The Antarctic Ice Sheet (AIS), the Greenland Ice Sheet (GrIS), the North American Ice Sheet (NaIS), which represents the Laurentide and Cordellian ice sheets, and the Eurasian Ice Sheet (EuIS), largely representing the Fennoscandian ice sheet and other ice caps on the continent. In this way a full assessment of past ice volume and temperature variability will be made over the past 1 Myr. Since sea-level changes are implicitly calculated within the model from ice-volume variations, the four ice sheets directly interact through changes in eustatic sea level.

Firstly, the model will be shortly introduced, for which a full description is found in Chapter 2, but the new implementations regarding the mass balance will be discussed here. Secondly, an assessment is made on the separate contributions of all ice sheets to sea-level change. Modelling results will be compared with other studies using models or observations of past sea level and temperature. Also, the separate contributions to δ_w are investigated and compared with findings from other studies. Finally, an analysis is performed on the hysteresis and the glacial response to temperature and sea level of the four ice-sheet models.

6.2 Ice-sheet model

In this chapter, a 3-D coupled ice sheet-ice shelf-bedrock model, called ANICE, is used in combination with the inverse methodology (Chapter 2) to reconstruct past ice-volume variations for four ice sheets. The 3-D model has been thoroughly described in Chapter 2, Section 2.4, and is based on the ice-sheet models used by Huybrechts (1990); Van de Wal (1999a); Bintanja et al. (2002, 2005b) and Bintanja and Van de Wal (2008). For each ice sheet the equations are solved on a 2-D grid, with a grid distance of 20 km for the Greenland Ice Sheet (GrIS) and 40 km for the Eurasian, North American and Antarctic Ice Sheets (EuIS, NaIS and AIS, respectively). Individual grid size and distance are shown in Table 6.1. The ice velocities are solved with a combination of two approximate equations, the Shallow Ice Approximation (SIA) (Hutter, 1983) and the Shallow Shelf Approximation (SSA) (Morland, 1987). The SIA determined velocities are dominated in the interior of the ice sheets, where the horizontal scale is far larger than the ice thickness, the SSA velocities are used as the ice-shelf and sliding velocities, similar to the approach used in the Parallel Ice sheet Model (PISM; Bueler and Brown, 2009; Martin et al., 2011; Winkelmann et al., 2011). The basal velocity, determined by the SSA, is simply added to the SIA for land grid points (Winkelmann et al., 2011).

Furthermore, mass is conserved using a combination of diffusive and advective fluxes that are adjusted to the available ice thickness for each grid point. For all four ice-sheet models, monthly initial precipitation and temperatures are adopted from the ERA-40 Re-analysis dataset, averaged from 1971 to 2000 (Uppala et al., 2005). These temperature fields are uniformly adjusted with the temperature anomaly ΔT_{NH}, which has been determined by the inverse routine. However, some additional parameterisations are needed for especially the temperature and precipitation fields of the EuIS and NaIS. This in order to reconstruct a realistic distribution of past ice-sheet cover during glacial periods (for example shown by Ehlers and Gibbard, 2007).

6.2.1 Temperature parameterisations

Often the initial 2-m air temperature fields are uniformly adjusted in ice-sheet model experiments with a constant temperature to simulate past or future climate change. However, modelling experiments with Global Circulation Models (GCMs) indicate that temperature differences between PD and the Last Glacial Maximum (LGM; 21 kyr ago) are not uniformly distributed over the Earth (Braconnot et al., 2007). As can be seen in Fig. 6.1, the strongest decrease in surface temperatures is found over areas with the largest increase in elevation, i.e. the location of the large NH ice sheets on Eurasia and North America. Although elevation changes in Antarctica and Greenland are substantially less, temperatures are also significantly lower during the LGM.

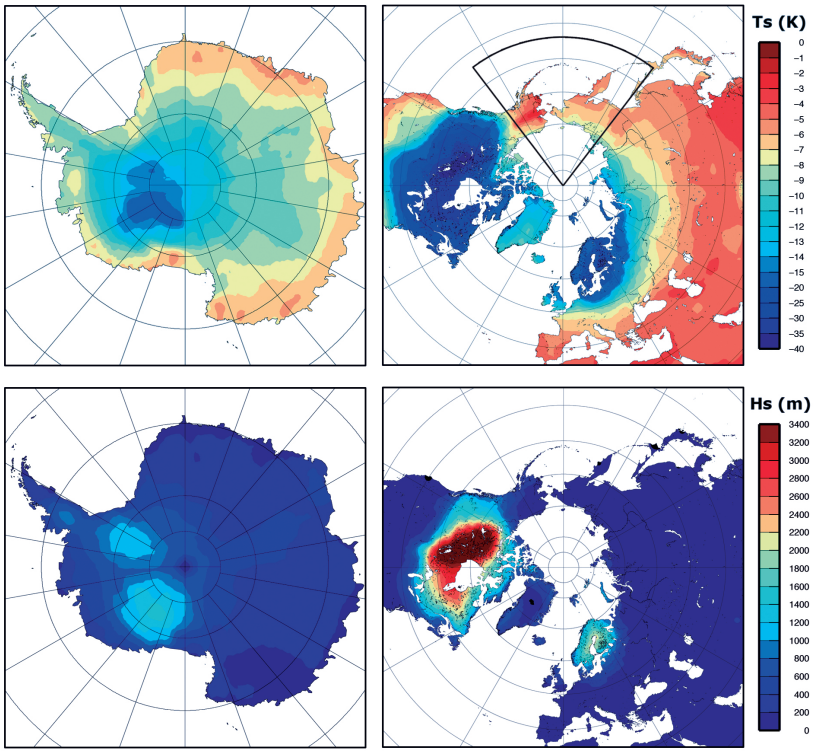

Figure 6.1 | *Differences between the LGM and PD from 5 PMIP2 models.* *The mean differences for five PMIP2 models as calculated for Antarctica (left) and the NH (right) over the present day continents. The ocean-atmosphere models used are: CCSM3, IPSL-CM4, HadCM3M2, MIROC3.2 and FGOALS-g1.0 (Braconnot et al., 2007). Top figures show the differences for the 2-meter surface-air temperature (K), the bottom figures show the difference in surface topography (m). The area bounded by the black line in the top figure indicates the region where the temperature anomaly is reduced to zero (see text).*

In ANICE, the temperature anomaly ΔT_{NH} represents changes over land areas reduced to sea level. Additionally, temperatures are reduced as function of elevation change with a constant atmospheric lapse rate for the NH ice sheets, as shown in Table 6.2. Over Antarctica, temperatures are adjusted with a separate lapse rate above and below 1500 m, incorporating the strong temperature inversion present over the AIS. Furthermore, two additional effects are needed to be taken into account in order to simulate a more realistic change in ice volume and ice cover.

Firstly, the temperature anomaly ΔT_{NH}, as inverted from equation 2.1, is added to the temperature fields for the three NH ice-sheet models, the GrIS, EuIS and NaIS. For the latter two models, however, the anomaly is reduced to zero over the Bering Strait region, i.e. no temperature adjustment (see boxed area in Fig. 6.1). This region

is shown to have much less pronounced reduced temperatures during the LGM, or even a positive anomaly (e,g, Zweck and Huybrechts, 2005; Braconnot et al., 2007). Secondly, a temperature correction is applied to the anomaly forwarded to the AIS. The formation of the large ice sheets on the NH continents themselves have influence on the regional climate. Therefore, temperatures, reduced to sea level, in the NH show a stronger decrease in glacial periods compared to the SH, as is also indicated by comparing LGM and PD averaged temperatures from GCMs. Using an average of 5 PMIP2 ocean-atmosphere GCMs this difference is estimated to be $\sim$3 K on average (Braconnot et al., 2007). The 3 K difference is used to adjust the temperature anomaly applied for the AIS as function of the total area of the EuIS and NaIS such that $\Delta T_{SH} = \Delta T_{NH}$ + 3 K at their approximate LGM surface area and 0 K for the PD climate.

6.2.2 Ice Sheet δ^{18}O

The ice-volume contribution to benthic δ^{18}O (i.e. δ_w) is mainly determined by the mean δ^{18}O of the ice sheets as is indicated by the 2nd and 3rd term on the r.h.s. of equation (2.2). The δ^{18}O concentration of the ice at the surface, equals the concentration of the precipitation and is calculated with the formulation introduced by Cuffey (2000):

$$\delta^{18}O_{surf} = \delta^{18}O_{PD} + \beta_T \Delta T_s + \beta_Z \Delta Z, \tag{6.1}$$

where $\delta^{18}O_{PD}$ (in ‰) is the PD distribution over the ice sheet as a function of the ERA-40 PD mean annual 2-m air temperature. The additional terms relate δ^{18}O$_i$ to changes in temperature (in °C) and surface elevation (in km) with respect to the PD reference fields. Values for the isotopic parameters β_T and β_Z are shown in Table 6.1 and selected within the range presented by Lhomme and Clarke (2005). In order to construct a PD $\delta^{18}O_i$ field from surface temperatures, the present literature contains several possibilities for both the Greenland and Antarctic ice sheets, mostly as a function of surface temperature only. For a consistent picture for all four ice sheets used, the relations introduced by Zwally and Giovinetto (1997) and Giovinetto and Zwally (1997) are used here. In these studies a δ^{18}O-Temperature relation has been derived for both present-day existing ice sheets:

$$GrIS: \quad \delta^{18}O_{PD} = 0.691 T_s - 13.43 \tag{6.2}$$

$$AIS: \quad \delta^{18}O_{PD} = 0.852 T_s - 6.78 \tag{6.3}$$

In case of the EuIS and NaIS, equation (6.2) is used, with the same parameters as for the GrIS (see Table 6.1). Additionally the $\delta^{18}O_i$ is spatially redistributed across the ice sheet using an advection scheme with the vertical averaged horizontal velocities. The $\delta^{18}O_i$ at the surface is furthermore adjusted via the Surface Mass Balance (SMB). As explained in Chapter 4, there is quite some uncertainty in the exact reference value

for the mean PD $\delta^{18}O_i$ of the AIS and GrIS. In ANICE, these values are set to the values resulting from modelling both ice sheets for four glacial cycles (Table 6.1). As will be shown later on, the ice volume contributions to δ_w of all four ice sheets are shown to be with the range of other estimates in the literature (e.g. Duplessy et al., 2002).

Table 6.1 | *Separate model parameters for the four ice-sheet models.*

Parameter	Description	EuIS	NaIS	GrIS	AIS
nx	number of x grid points	241	200	141	141
ny	number of y grid points	121	130	77	141
Δx	grid scale (km)	40	40	20	40
β_T	Isotopic sensitivity (‰ °C^{-1})	0.35	0.35	0.35	0.6
β_Z	Isotopic lapse rate (‰ km^{-1})	–6.2	–6.2	–6.2	–11.2
PD ΔS	PD ice volume (m s.e.)	0.0	0.0	7.09	60.35
PD $\delta^{18}O_i$	PD ice-sheet isotopic content (‰)	0.0	0.0	–29	-43

6.3 Mass balance

The mass balance model serves as the coupling between the climate and the dynamical ice-sheet model. As mentioned earlier, PD climate fields of monthly precipitation and temperature are used to force the ice-sheet models. Following the changes in temperatures as described above, the precipitation rate is also influenced by temperature. As follows from Clausius-Clapeyron, lower temperatures reduce the average precipitation rate since the atmosphere moisture capacity is reduced. Additionally, changes in elevation (surface slopes) are needed to be taken into account, creating, or reducing uplift of moisture.

6.3.1 Accumulation changes in Antarctica

To simulate changes in precipitation for the AIS, an equation as function of the free atmospheric temperature above the inverse layer (in K) is used:

$$T_I = 88.9 + 0.67 T_s. \tag{6.4}$$

This equation has been derived for the atmospheric conditions over Antarctica, where a strong inversion layer prevails over the ice sheet (e.g. Bintanja et al., 2002). The precipitation change can then be formulated as:

$$P = P_{PD} \left(\frac{T_{I,PD}}{T_I} \right)^2 exp \left[22.47 \left(\frac{T_0}{T_{I,PD}} - \frac{T_0}{T_I} \right) \right], \tag{6.5}$$

with P_{PD} the ERA-40 reference field of precipitation (in m yr^{-1}) and $T_{I,PD}$ the reference temperature above the inverse layer (in K). The above equations accounts for both elevation changes, which are incorporated in the temperature adjustment, and for changes in the moisture content of the atmosphere, resulting in lower precipitation rates during colder climates (Huybrechts, 2002).

6.3.2 Accumulation for the NH ice sheets

For the other three ice sheets a precipitation model is used to adjust the PD precipitation field. The model includes orographic forcing of precipitation and changes in the moisture content, which are calculated from the 2-m surface-air temperature and the 850 hPa wind fields (Roe and Lindzen, 2001; Roe, 2002):

$$P = e_{sat} Max[0,(a+bw)]\, f(w) dw. \tag{6.6}$$

Here, the saturation vapour pressure e_{sat}, is related to the moisture content of the atmosphere given by the Clausius-Clapeyron relation as function of the surface-air temperature (Roe, 2002):

$$e_{sat} = e_0 e^{c_1 T_s/(c_2+T_s)}. \tag{6.7}$$

The three parameters, e_0, c_1 and c_2 are included in Table 6.2 and are adopted from Roe (2002). The vertical uplift is controlled by parameters a and b (shown in Table 6.2) that define the background precipitation rate and the influence of the vertical velocity, respectively (Roe and Lindzen, 2001). The vertical velocity w is defined as an approximate function of the 850 hPa horizontal winds and the surface slope, similar to the approach in Roe (2002):

$$w = Max\left[0, w_x \frac{\partial H_s}{\partial x} + w_y \frac{\partial H_s}{\partial y}\right]. \tag{6.8}$$

The mid-atmospheric flow patterns at 850 hPa are shown to be the most appropriate to represent uplift due to a sloping edge (Roe, 2002). In equation 6.8, w_x and w_y are the interpolated wind fields in the x and y direction of the ice-sheet grid, respectively, and H_s is the surface elevation. The function $f(w)$ is a Gaussian probability distribution function of w, and defined as:

$$f(w) = \frac{e^{-\left(\frac{w-w_0}{a_{vv}}\right)^2}}{N}, \tag{6.9}$$

with a_{vv} a measure for the variability of the vertical velocity and N a normalisation factor (Roe, 2002). This formulation takes into account the spatial variability of the uplift. Equation (6.6) is analytically solved through integration and using error functions as

shown in the Appendix of Roe and Lindzen (2001). The modelled precipitation from equation (6.6) is calculated as a ratio relative to the PD modelled precipitation calculated from the PD temperature and surface elevation. With a maximum ratio of 2, this ratio is used to adjust the monthly precipitation from ERA-40. Results show that precipitation is largely reduced over the ice sheets in colder climates and that ice sheets grow in the upwind direction.

Table 6.2 | *Physical parameters used for the 3-D ice-sheet model.*

Constant & description		value
ρ_i	ice density (kg m^{-3})	910
ρ_w	seawater density (kg m^{-3})	1028
e_0	reference saturation vapour pressure (mbar)	6.112
c_1	Clausius-Clapeyron parameter 1	17.67
c_2	Clausius-Clapeyron parameter 2 (°C)	243.5
a	background precipitation rate (m^2 s kg^{-1})	2.5×10^{-11}
b	uplift precipitation parameter (m s^2 kg^{-1})	5.9×10^{-9}
a_{vv}	variability in vertical velocity (s m^{-1})	100
ρ_i	ice density (kg m^{-3})	910
ρ_w	seawater density (kg m^{-3})	1028
α_w	albedo of ocean water	0.1
α_g	albedo of bare soil	0.2
α_{ice}	albedo of glacier ice	0.5
α_{sn}	albedo of fresh snow	0.85
c_p	specific heat capacity of ice (J kg^{-1} °C^{-1})	2009
c_{pO}	specific heat capacity of ocean (J kg^{-1} °C^{-1})	3974
γ_T	thermal exchange velocity (m s^{-1})	10^{-4}
F_{melt}	sub ice-shelf melt parameter (m s^{-1})	5×10^{-3}
L	Latent heat of fusion (J kg^{-1})	3.35×10^5
Γ_{low}	lapse rate $<$ 1500 m (K km^{-1})	5.102
Γ_{high}	lapse rate $>$ 1500 m K km^{-1})	14.285
Γ_{NH}	lapse rate for the NH (K km^{-1})	8.0
T_0	triple point of water (K)	273.16
M_e	CD, PD and WM ocean melt rate for exposed shelf (m yr^{-1})	0, 3, 6
M_d	CD, PD and WM ocean melt rate for deep-ocean areas (m yr^{-1})	2, 5, 10
T_{oc}	CD, PD and WM sub ice-shelf temperature (°C)	-5, -1.7, 2

6.3.3 Ablation and refreezing

The ablation rate (in m w.e. yr^{-1}) used here is a parameterisation based on PD mass balance observations and modelling results for Antarctica and Greenland (Bintanja et al., 2002; Van den Berg et al., 2008) and incorporates changes in temperature and insolation:

$$A = \Delta t(4T_s + 0.55(1-\alpha)Q + C_{abl})/(\rho_{fw}L), \tag{6.10}$$

here Q is the monthly incoming shortwave radiation at the top of the atmosphere (W m^{-2}), which is changed every 1000 years (Laskar et al., 2004), ρ_{fw} = 1000 kg

m^{-3} is the density of fresh water and L the latent heat of melt. The constant 4 (W m^{-2} K^{-1}) shows the dependence on the temperature, and 0.55 is an average value for the transmissivity of the atmosphere. The constant C_{abl} is used to compensate for other melt processes and is set to C_{abl} = -32 for all four ice sheets. Furthermore, the transmissivity is set to a value of 0.55, a slightly higher value with respect to Bintanja et al. (2002) therefore creating a slightly higher sensitivity to changes in insolation. These values are chosen in a way that after several glacial cycles PD ice volume is closely matched the current observations of ice volume and that the present-day mass balance patterns are in coherence with observations.

As is illustrated in Fig. 6.2, the model performs well for glacial-interglacial variability. However, with respect to other modelling experiments that use the same parameterisation approach differences might occur in the choice of parameters. For example, (Bintanja et al., 2002) used a much higher value of C_{abl} for the AIS of -88, probably due to the exclusion of refreezing. In ANICE refreezing is included and therefore the largest part of the (summer) melt that occurs on Antarctica in the model is refrozen, leading to a similar surface mass balance as Bintanja et al. (2002). Also, the studies of Van den Berg et al. (2008) and Robinson et al. (2011) show a different choice of parameters for the EuIS and GrIS, respectively. These difference are mainly explained by the use of different climate/precipitation models and the initial data fields used in these studies such as initial topography, precipitation and temperature, which is in ANICE used as monthly input. Furthermore, the surface albedo is defined as:

$$\alpha = Max(\alpha_g, \alpha_{sn} - (\alpha_{sn} - \alpha_{su})e^{-15d} - 0.015A) \tag{6.11}$$

where α_g, α_{sn} and α_{su} are the soil, snow and surface (soil or ice) albedo, respectively (listed in Table 6.2), d is the snow depth (m) and A is the ablation rate at the previous time step, calculated from equation (6.10). The e-folding term represents the effect of snow thickness and patchiness on the albedo, with the snow depth determined within the model as a function of the cumulative mass balance (Bintanja et al., 2005b).

Additionally, refreezing of rain and melt water is incorporated according to the model described by Janssens and Huybrechts (2000), with the potential retention as function of the surface temperature (model (iii) in Janssens and Huybrechts (2000)). In this model, the refreezing process is determined by two fractions of the total precipitation P; (i) the "available-water fraction", w_r, which is the sum of rain and melt water, and (ii) the "potential-retention fraction", p_r, which is the maximum amount of superimposed ice:

$$p_r = Min\left(\frac{2c_p}{L}\frac{T_0 - T_{surf}}{P}; 1\right) \tag{6.12}$$

This maximum amount of superimposed ice is equal to the latent heat released to raise the temperature of the top 2 meters of the ice-sheet surface to the melting point T_0

(Huybrechts and de Wolde, 1999). Here, L is the latent heat of fusion, and c_p the heat capacity of ice (both shown in Table 6.2). Finally, the "effective-retention fraction" follows from: $e_r = \text{Min}(w_r, p_r) \leq 1$, which is multiplied by the total precipitation to obtain the final results included in the surface mass balance. Although refreezing processes over the larger part of Antarctica can be neglected, due to too cold temperature throughout the year, for the NH ice sheets refreezing can have a significant contribution to the SMB.

All the above parameterisations are explicitly calculated for each grid point with a time step of one month. Ablation is set to zero if positive, therefore giving only negative values, i.e. melt, during the actual melt season. Moreover, for all models the monthly snow accumulation is obtained as a temperature-dependent fraction of the total precipitation (Bintanja et al., 2002). The total SMB (in m yr^{-1}) is then finally calculated as:

$$SMB = P - A + e_r P, \tag{6.13}$$

and is forwarded to the mass continuity equation (2.22), for which the SMB is rescaled to ice equivalent meters using a water density of 1000 kg m^{-3} and an ice density of 910 kg m^{-3}.

6.3.4 Sub ice-shelf oceanic melt

An important aspect of the growth and decay of ice shelves, i.e. the floating parts of an ice sheet, is the description of melt below the ice shelves. In ANICE, a combination is used of the parameterisation introduced by Pollard and DeConto (2009) and the temperature based formulation applied by Martin et al. (2011). For the GrIS model ice shelves are considered negligible and not taken into account. PD sub-ice-shelf oceanic melt (m yr^{-1}) is given by:

$$M = (1 - z_d)\left[(1 - z_e)\, S_{melt} + z_e M_e\right] + z_d M_d, \tag{6.14}$$

with S_{melt} the melt flux from shelf to ocean (m yr^{-1}). M_e is the melt rate for exposed shelves and M_d the melt rate for the deep ocean, which are spatially invariant. Both are adjusted with a weighting function (equation (6.20)) which is a function of temperature and insolation, and therefore a function of time. Different values for cold (CD), PD and warm (WM) climate conditions are shown in Table 6.2. The weighting factor for the deep ocean is given as a function of bedrock height below sea level:

$$z_d = Max(0, Min(1, (\Delta S - H_b + Z_{shelf})/200)), \tag{6.15}$$

where Z_{shelf} defines the boundary for the continental shelf depth, chosen to be -1800 m for the AIS, -1200 m for the NaIS and -800 m for the EuIS. The weighting factor

for the exposed shelves is given by:

$$z_e = Max(0, Min(1, (\theta_{sub} - 80)/30))e^{-D_{open}/100}. \quad (6.16)$$

Here, θ_{sub} is the total angle (in degrees) subtended by the set of straight lines from the grid point to the open ocean, and D_{open} is the distance (in km) to the closest open ocean grid point (Pollard and DeConto, 2009). The melt rate underneath the ice shelves, S_{melt}, in equation (6.14) is based on heat transfer between the bottom of the ice and the ocean water beneath (Beckmann and Goosse, 2003; Martin et al., 2011). Firstly, the freezing temperature of the saline ocean water (in °C) at the shelf base is calculated with:

$$T_f = 0.0939 - 0.057 \cdot S_0 + 7.64 \times 10^{-4} z_b. \quad (6.17)$$

Here, S_0 = 35 psu, the average salinity of the ocean water and z_b is the depth of the ice-shelf base calculated as: $z_b = -(\rho_i/\rho_w)H_i$. Next, the heat flux from ocean to ice is calculated as:

$$Q_{heat} = \rho_w c_{pO} \gamma_T F_{melt} (T_{oc} - T_f), \quad (6.18)$$

with the different parameters adopted from Martin et al. (2011) and shown in Table 6.2. T_{oc} is the ocean-water temperature (in °C) adjusted with a weighting function (equation (6.20)). The heat flux can have both positive and negative values, either leading to melting of ice shelves or (re)freezing of ocean water (Beckmann and Goosse, 2003). Finally, the mass flux from shelf to ocean, S_{melt}, used in equation (6.14) is given by:

$$S_{melt} = Q_{heat}/L\rho_i. \quad (6.19)$$

To simulate glacial-interglacial climate variability, the melting rates M_e, M_d and T_{oc} in equations (6.14) and (6.18) are adjusted with a weighting function, which has a similar form as given by Pollard and DeConto (2009):

$$w_g = 1 + \Delta T/12 + Max(0, \Delta q_j/40) \in [0;2]. \quad (6.20)$$

Here ΔT is the applied temperature anomaly relative to PD, either ΔT_{NH} from the inverse routine equation (2.1), or the slightly reduced temperature anomaly for the SH. Similarly, for the insolation anomaly relative to PD Δq_j separate values are used. For the AIS the January 80°S anomaly, and the June 65°N anomaly relative to PD (W m^{-2}) for the NH ice sheets. The melt rate for exposed shelves, M_e, deep-ocean areas, M_d, and sub-shelf ocean temperatures, T_{oc}, are adjusted for colder than PD periods, when $0 \leq w_g < 1$, as:

$$V_{melt} = (1 - w_g)V_{CD} + w_g V_{PD}, \quad (6.21)$$

and for warm periods, when $1 \leq w_g \leq 2$:

$$V_{melt} = (2 - w_g)V_{PD} + (w_g - 1)V_{WM}. \tag{6.22}$$

Here, V_{CD}, V_{PD} and V_{WM} indicate the cold, present day and, warm value of the melt variables, respectively, shown in Table 6.2. The melt rates and ocean temperature are adapted such that ANICE produces realistic PD ice shelves and grounding line location for the AIS. Fig. 6.2 illustrates the temporal evolution of all mass balance terms of the four ice sheets over one glacial cycle. All variables are summed separately over ice sheet grid points, so Hi > 0, and ice shelf grid points for Hi > 200 m. The yellow shading indicates stages when the ice sheet is thinning, white areas indicate an increase in ice volume. Mass balance variations for the AIS are shown in Fig. 6.2a, clearly illustrating the dominance of the basal melt or refreezing (during glacial stages) and the ice discharge (grey) which balances the SMB (orange). In case of all three NH ice sheets, glacial stages are dominated by a larger SMB relative to little basal melting (light blue) and intermediate ice discharge. During the glacial termination (from 340 to 330 kyr ago) the decrease in ice volume of the EuIS and NaIS, Fig. 6.2b and d respectively, is both caused by increasing loss through ice discharge (grey lines) and a rapid increase in ablation (red lines).

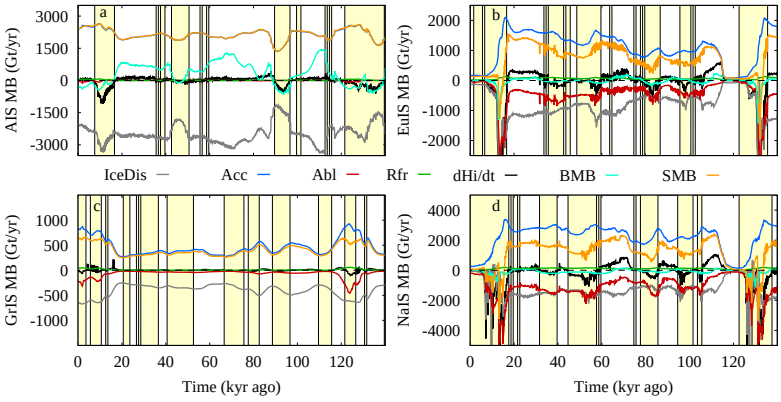

Figure 6.2 | *Evolution of mass balance variables over 1 glacial cycle.* *The time variability of the total mass balance and dynamical terms in Gt per year (= 10^{12} kg) are shown for a) AIS, b) EuIS, c) GrIS, d) NaIS. All variables are integrated over all ice sheet grid points, and shelf grid points with an ice thickness above 200 m. The different colours indicate: grey: ice discharge (ice flux towards grid points without ice), blue: accumulation, red: ablation, green: refreezing, light blue: basal mass balance, orange: surface mass balance, black: total change in ice thickness. The yellow shading indicates when ice volume is decreasing, i.e. dHi/dt < 0.*

6.4 Results

6.4.1 Reconstruction over the past 1 Myr

With the setup as described above, model simulations have been performed over the past 1 Myr, reconstructing global ice volume with four ice-sheet models and NH continental mean temperature (between 40° and 80°N) relative to PD. For the forcing of the model, the LR04 benthic δ^{18}O stack of 57 deep-sea sediment records has been used (Lisiecki and Raymo, 2005) as input in the inverse routine equation (2.1). The main results obtained with the model are shown in Fig. 6.3, presenting a self-consistent reconstruction of past surface-air temperature (Fig. 6.3b in green) and eustatic sea level (Fig. 6.3c in blue) derived from ice volume over the past 1 Myr.

Fig. 6.3a shows the benthic δ^{18}O stack as forcing of the model (black) with the separate contributions of ice volume (δ_w in blue) and temperature (green). Clearly, there is a lot of variability in both contributions. The ice-volume variations dominate the signal during glacial periods. The same picture emerged from previous studies (Bintanja et al., 2005a; Bintanja and Van de Wal, 2008) and from the 1-D model

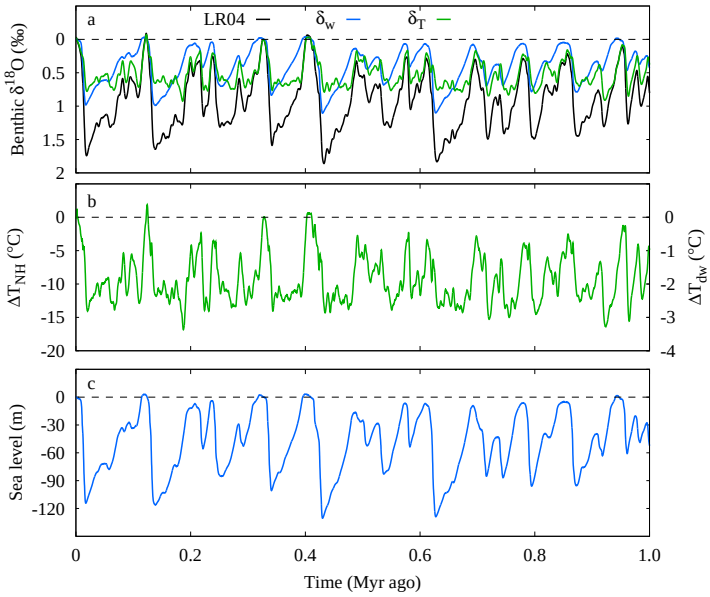

Figure 6.3 | *3-D modelling results over the past 1 Myr.* *From top to bottom, the Lisiecki and Raymo (2005) benthic $\delta^{18}O$ stack (LR04 in black) , separated in an ice volume contribution, (δ_w in blue) and a temperature contribution (δ_T in green). Reconstructed surface-air temperature for the NH (green) and eustatic sea level from ice volume (blue). All variables are relative to PD which is indicated by the dashed lines..*

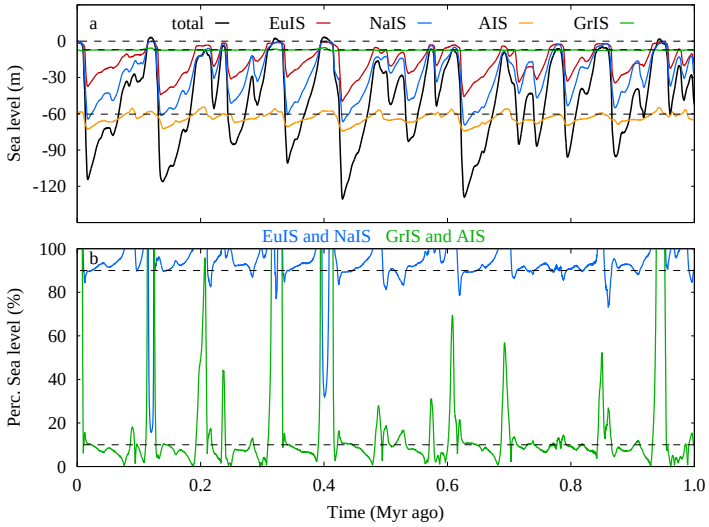

Figure 6.4 | *Separate contribution to eustatic sea level over the past 1 Myr.* *The top figure shows the separate ice volume variations (in m s.e.) per ice sheet, EuIS(red), NaIS(blue), AIS(orange), GrIS(green) and total eustatic sea level in black, all relative to PD. The bottom figure shows the separate contribution, in percentage of eustatic sea level, from the EuIS and NaIS (blue) and the GrIS and AIS (green). Dashed lines indicate the 90 and 10% levels.*

reconstruction presented in Chapters 3 and 4. In contrast to earlier studies, the full ANICE 3-D model reconstruction presented here creates the possibility for a complete assessment of the separate contributions of the four ice sheets to eustatic sea level and δ_w variability. Therefore simulating eustatic sea-level both above and below the present level.

6.4.2 Contributions to sea level

As can be seen in Fig. 6.4a, the largest contribution to eustatic sea level relative to PD over the past 1 Myr originate as expected from the EuIS and NaIS, the red and blue curve respectively. The GrIS only shows significant variability during interglacial periods (in green), for example during the previous interglacial, the Eemian (ca. 125 kyr ago), contributing to a sea level rise. Also, the AIS (in orange) experiences some melt during these periods, up to 2 m s.e., which predominantly originates from the marine West Antarctic ice sheet. During glacial times, equivalent sea level of the AIS increases with a typical value of about 10-12 m s.e., similar to other modelling studies (e.g. Huybrechts, 2002; Pollard and DeConto, 2009). Combined, the GrIS and AIS are responsible for ca. 10% of the total eustatic sea level variations during glacial maxima, as illustrated in Fig. 6.4b. This is close to the value as was originally esti-

mated by Bintanja et al. (2005a), who estimated the contribution to be 15%. Naturally this number varies quite significantly, whereas at the start of a glacial cycle sea-level changes are dominated by the EuIS and NaIS. During interglacials, however, the GrIS and AIS contribution increases to 100% when both the EuIS and NaIS decrease in volume rapidly or even completely disappear (Fig. 6.4b).

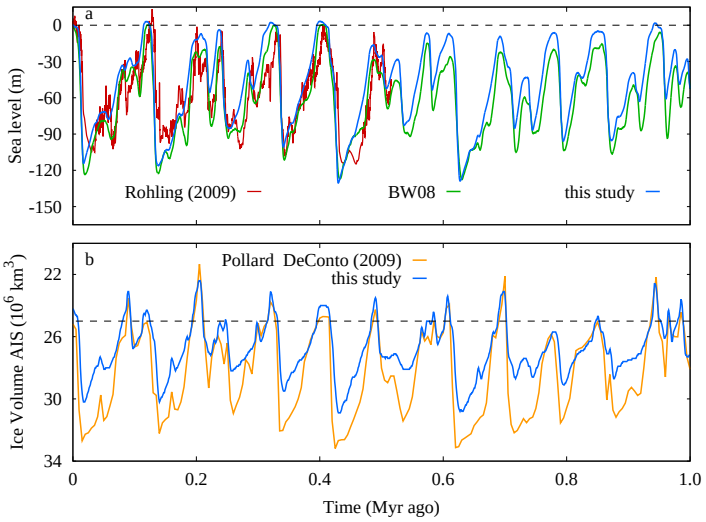

Figure 6.5 | *Comparing sea level and ice volume with models and observations.* *The top figure shows a comparison for eustatic sea level from this study (blue) with the Red Sea relative sea-level reconstruction (red) from Rohling et al. (2009) and NH (only EuIS and NaIS) sea level reconstruction from Bintanja and Van de Wal (2008) (BW08 in green), all relative to PD. The bottom figures shows a comparison for total Antarctic ice volume (blue) with the modelling work by Pollard and DeConto (2009) in orange.*

6.4.3 Comparing with sea level reconstructions

In Fig. 6.5 the ANICE results are compared with previous modelling results and observations over the past 1 Myr. Firstly, Fig. 6.5a shows a comparison of the ANICE results (blue) with the previous NH result from Bintanja and Van de Wal (2008) (BW08; green). The previous estimated 15% contribution from the GrIS and AIS yields an excellent coherence in sea level variations during glacial periods. Off course, as is illustrated in Fig. 6.4b, the relation does not hold for periods with high sea level stands, where the BW08 results clearly underestimate the obtained eustatic sea level curve from the ANICE models. In this study, the combination of the four ice-sheet models makes it possible to also model sea level variations above PD, i.e. melt of the AIS or GrIS, therefore simulating a more realistic estimate of interglacial eustatic sea level.

Secondly, as can be seen in Fig. 6.5a, a good correlation is found with the Red Sea record (red) over the past 0.5 Myr (Rohling et al., 2009). Although the steep variability is not met for especially a lowering of sea level, for example during the previous glaciation (200 to 150 kyr ago). Lastly, Fig. 6.5b shows an independent comparison with modelled Antarctic ice volume from Pollard and DeConto (2009). Since both models are driven by the same δ^{18}O record of Lisiecki and Raymo (2005), they show a coherent timing of ice-sheet growth and retreat. Although for most interglacial periods the modelled ice volume agrees quite well, the Pollard and DeConto (2009) study shows a far larger AIS during glacial stages. These differences can be attributed to the use of different mass balance models, both surface and sub-shelf, and the difference in the methodology to solve grounding line dynamics and basal sliding.

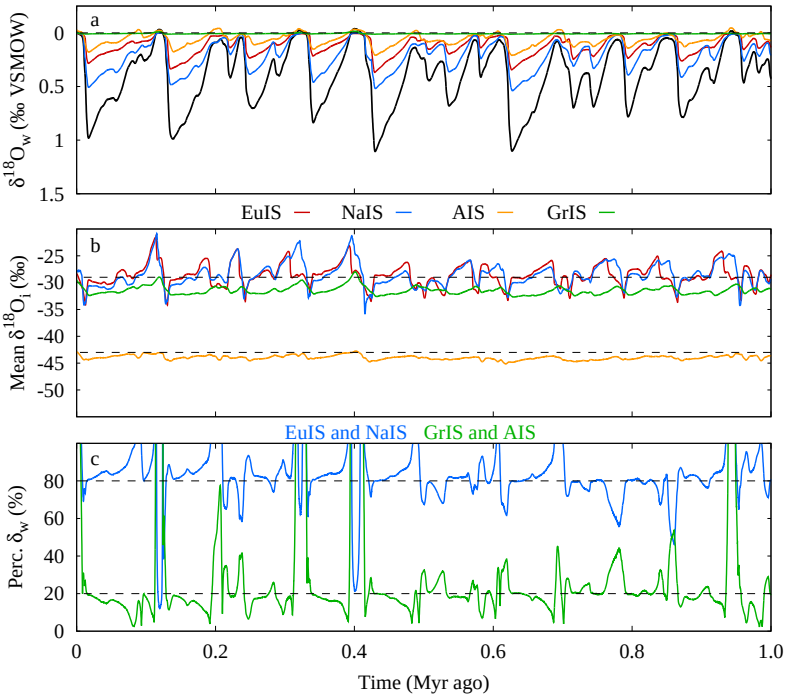

Figure 6.6 | *Separate contributions to δ_w variations.* *From top to bottom, the separate contributions to δ_w (VSMOW) relative to PD from the four ice sheets, colors as in Fig. 6.4. The second figure shows the variations in the mean $\delta^{18}O_i$ of the ice sheets, used to calculate δ_w weighted with ice volume (equation (2.2)). The last figure shows the separated contribution, in percentage of δ_w, from the EuIS and NaIS (blue) and the GrIS and AIS (green). The dashed lines indicate the 80 and 20% levels.*

Table 6.3 | *Comparison of LGM contribution to δ_w, all values in ‰ VSMOW. For the mean estimate of Duplessy et al. (2002) the root mean square difference is shown in parentheses.*

Source	δ_w	AIS	GrIS	EuIS	NaIS
ANICE	0.953	0.175	0.010	0.283	0.486
Duplessy et al. (2002)	1.200 (0.23)	0.318	0.073	0.195	0.615
Lhomme and Clarke (2005)		0.190	0.010		
Sima et al. (2006)					0.630

6.4.4 Contributions to δ_w

Similar to the evaluation of the separate ice-volume contributions, the contributions to δ_w are illustrated in Fig. 6.6. Note that the ice-volume contributions to δ_w are calculated according to equation (2.2), and are a weighted value of ice-sheet mean $\delta^{18}O_i$ changes with ice volume. As is clear from Fig. 6.6a, the EuIS and NaIS (in red and blue, respectively) are responsible for the largest part of the variability in δ_w, analogue to the eustatic sea level variations. Furthermore, the contribution from the GrIS (in green) is very small, due to the relatively small changes in ice volume. Although mean $\delta^{18}O_i$ variations, as shown in Fig. 6.6b are quite significant for the GrIS. Moreover, the AIS contribution (in orange) is quite substantial despite the limited volume changes, mainly due to the much lower values in mean $\delta^{18}O_i$, as can be seen Fig. 6.6b.

The combined contributions from the AIS and GrIS are quite substantial, as is shown by the green curve in Fig. 6.6c. On average, this varies between 10 to 20% during glacial periods, and increasing to 100% for interglacial stages. The variability is highly coherent with the signals for sea level, as shown in Fig. 6.4b. However, due to the large negative values of mean $\delta^{18}O_i$, caused by the geographical location and higher surface elevation, the contribution of the AIS increases quite substantially. Moreover, this estimate is much larger than the assumed contributions of 5% by (Bintanja et al., 2005a).

In Table 6.3, the ANICE model output is compared with other estimates of ice-volume contributions for the Last Glacial Maximum (LGM). As can be seen, the total value of δ_w relative to PD (in VSMOW) is lower compared to the average estimate of Duplessy et al. (2002). However, the range given by Duplessy et al. (2002), a rmsd of 0.23‰, is also substantial. The separate contributions are comparable, especially compared with the estimates of Lhomme and Clarke (2005), who modelled the mean $\delta^{18}O_i$ with a tracer-transport scheme. Although the modelled values in ANICE are substantially higher, the variability is shown to be very much alike. For ANICE the same isotopic sensitivity and lapse rates are used as in Lhomme and Clarke (2005), see Table 6.1. Hence, this indicates that the use of vertically averaged velocities for transport of $\delta^{18}O_i$ are a good approximation of δ_w variability relative to the use of a full scale tracer-transport scheme. The individual estimates with ANICE are quite

different from those presented by Duplessy et al. (2002). Compared to their lowest estimate (not shown), the differences for the AIS and NaIS are much less, whereas the estimate for the GrIS stays the same and the value for the EuIS is substantially reduced. The estimate of Sima et al. (2006) is quite high compared to ANICE, largely due to the higher ice volume of the NaIS during the LGM.

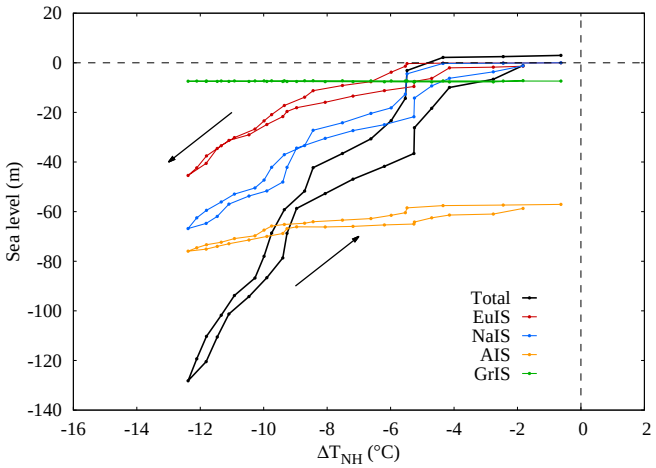

Figure 6.7 | *Equilibrium experiment.* *The equilibrium experiment with the four 3-D ice sheets, plotted sea level (in m s.e.) vs. temperature (ΔT_{NH} in K) at each $\delta^{18}O$ step. Total sea level (black), the EuIS (red), the NaIS (blue), the AIS (orange) and the GrIS (green). All values are relative to PD, the arrows indicate the direction of the stepwise changing benthic $\delta^{18}O$.*

6.4.5 Investigating hysteresis

Similar to a previous experiment with the 1-D models, shown in Section 3.3, also the hysteresis for the combined four 3-D ice-sheet models has been investigated with a stepwise changing δ^{18}O. For this experiment the benthic δ^{18}O as forcing was varied with steps of 0.1‰. The experiment was initiated at a δ^{18}O value of 3.2‰, close to the LR04 PD value of 3.228‰ and increased to a maximum value of 5‰, from which δ^{18}O was reduced back to the initial value. Each δ^{18}O value was kept constant for 25 kyr allowing the ice sheets to develop to a steady state, resulting in an equilibrium temperature and sea level corresponding to every δ^{18}O value. In Fig. 6.7 sea level is shown as a function of the corresponding equilibrium ΔT_{NH} for total eustatic sea level (black) and for the separate ice sheets. The increasing δ^{18}O is depicted by the upper branch, so decreasing sea level and temperatures. All four models show little evidence for hysteresis, providing confidence in the interactions with sea level and temperature variations, in coherence with other studies (e.g. Pollard and DeConto, 2009).

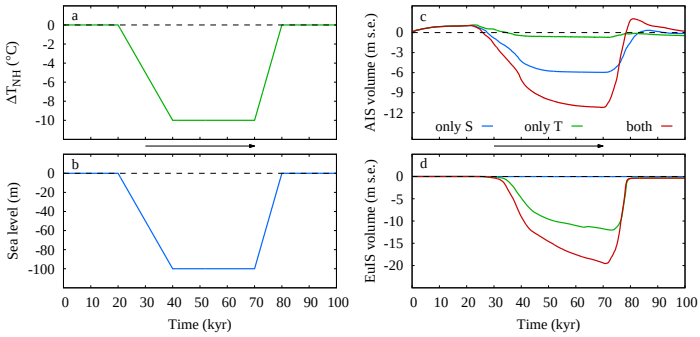

Figure 6.8 | *Linear glacial forcing with sea level and/or temperature.* *Sensitivity tests with linear forcing sea level and/or temperature to a minimum of -100 m and -10 K, respectively. a) Temperature forcing, b) sea level forcing, c) Antarctic ice volume (m s.e.) and d) Eurasian ice volume (m s.e.). in c) and d), green is for temperature only, blue for sea level only and red for forcing with both variables. Arrows indicate the direction of the time evolution.*

6.4.6 Response to sea level and temperature

To furthermore assess the sensitivity to changes in the forcing, an experiment was carried out with linear glacial forcing of sea level and temperature below PD. Over the course of 100 kyr, temperature and sea level are varied as shown in Fig. 6.8a and b, respectively. The experiments were performed as stand alone experiments with the usual setup of the ice-sheet models but without benthic δ^{18}O forcing and varying insolation. The standard experiments, the red curves in Fig. 6.8c,d, are forced with both linear sea level and temperature 'records'. Additionally, two sensitivity tests were performed with forcing the models with either temperature (green curves) or sea level (blue curves). When temperature variations are not taken into account also the weighting function equation (6.20) is not adjusted, keeping sub-shelf melt/refreezing at PD magnitude.

Fig. 6.8a shows the ice volume changes for the AIS (in m s.e. relative to PD). When only temperature is varied (green curve) the ice sheet shows a very limited increase in ice volume for a temperature 10 K below PD. On the other hand, sea level does show to have a significant impact on Antarctic ice volume (blue curve). The volume gain for the combined forcing is clearly more than the sum of the two separate experiments, whereas the changes in ice volume are enhanced by a decrease in temperature, due to a decrease in sub-shelf oceanic melt. The opposite emerges from the experiments with the EuIS, for which Fig. 6.8d shows ice volume variations (m s.e.). When only sea level is varied, there is no significant response in ice volume. Since temperature are fixed to PD conditions there is therefore no change in the surface mass balance. However, when temperatures are decreased the ice growth is initiated

due to a positive SMB. The combined forcing shows again the strongest response. This is mainly due to a progression of the coast line and therefore ice can advance to lower parts around the continent. The NaIS behaves in a similar way (not shown).

6.5 Conclusions

In this chapter, the inverse methodology is applied on four 3-D ice-sheet models, simulating glaciation on Antarctica, Greenland, Eurasia and North America. The inverse forward modelling approach is forced with benthic δ^{18}O data from the LR04 stack of 57 deep-sea sediment records (Lisiecki and Raymo, 2005), calculating the NH temperature anomaly relative to PD ΔT_{NH}. The temperature anomaly is forwarded to the ice-sheet models to determine ice volume and ice-sheet mean $\delta^{18}O_i$, and is used to calculate the deep-water temperature anomaly (equation (2.3)). Combined, the modelled benthic δ^{18}O can be calculated according to equation (2.2). The root mean square difference between the observed LR04 data and the modelled δ^{18}O is only 0.0547‰, implying a nearly perfect reproduction of benthic δ^{18}O by the methodology applied here.

During the Pleistocene glacial cycles, variations in eustatic sea level (derived from ice volume) are dominated by changes in ice volume of the EuIS and NaIS. The contribution of the GrIS and AIS to eustatic sea level are about 10%, similar to earlier estimates and modelling results (Huybrechts, 2002; Bintanja et al., 2005a; Pollard and DeConto, 2009). Naturally, during interglacial stages the GrIS and AIS dominate changes in eustatic sea level, also contributing to sea level above PD, i.e. melt of ice. Negative changes for the AIS predominantly originate from the marine based West Antarctic ice sheet. Furthermore, the ANICE modelling result show a good coherence with observed sea level changes during the past 0.5 Myr (Rohling et al., 2009).

Also, the ice-volume contributions to sea water δ^{18}O (δ_w) are evaluated. Since the variations in eustatic sea level are dominated by the EuIS and NaIS, these ice sheets also provide the largest contributions to δ_w during glacial stages. The contribution of the GrIS is very limited due to the relatively small changes in ice volume. However, although AIS ice volume change is relatively small, the weight is larger due to the much lower mean $\delta^{18}O_i$. The combined contribution of the GrIS and AIS varies between 10 to 20%, a significantly higher contribution as was originally estimated by Bintanja et al. (2005a). Furthermore, the contributions to δ_w at the LGM relative to PD are comparable with published estimates (Duplessy et al., 2002; Lhomme and Clarke, 2005; Sima et al., 2006). The total value of about 1.0‰ agrees rather well with the estimates provided by Duplessy et al. (2002) and other studies (e.g. Schrag et al., 2002). Also for the individual ice sheets the estimates in this study are comparable with results of other modelling studies (Lhomme and Clarke, 2005; Sima et al., 2006). although subject to quite some uncertainty.

Moreover, an equilibrium experiments has been performed by forcing the model with a stepwise changing benthic δ^{18}O, providing limited evidence for hysteresis in coherence with earlier studies (e.g. Pollard and DeConto, 2009). The individual ice sheets have furthermore been tested on their sensitivity to changes in sea level and temperature. Forcing the ice sheets with a linear function of either temperature (to -10 K) or sea level (to -100 m) provided a striking difference between the AIS and the EuIS and NaIS. For Antarctica, a decrease in sea level results in a significant increase in ice volume, which is enhanced by lowering temperatures and hence a decrease in oceanic shelf melt. In contrary, ice volume variations on Eurasia are initiated with a decrease in temperature and enhanced by sea level. This experiments shows the greater importance of simultaneously simulating the four prominent ice sheets during the Pleistocene. Therefore, the interaction with changes in sea level is possible, which is internally calculated in the model and thus a function of ice volume.

The results presented in this chapter are the first self-consistent assessment of temperature and global ice volume simulation over the past 1 Myr with 3-D ice-sheet models. The four models combined create the possibility to evaluating contributions to eustatic sea level and δ_w. The parameterisations used in ANICE can be tested on their sensitivity, similarly to the 1-D model reconstruction as shown in Chapters 3 and 4. Although the climate physics in the model do show to be capable of producing realistic changes in ice volume and temperature, there is quite some room for improvements. As will be discussed in the successive chapter, both interaction with the climate and the ocean could be quite easily improved by using (simplified) models for the atmosphere and changes in regional sea level.

Acknowledgements. For the use of the PMIP2 GCM model output, we acknowledge the international modelling groups for providing their data for analysis, the Laboratoire des Sciences du Climat et de l'Environnement (LSCE) for collecting and archiving the model data. The analyses were performed using version 01-07-2010 of the database. David Pollard is thanked for providing Antarctic ice volume data over the past 5 Myr.

7

Conclusions and outlook

Concluding from the modelling work presented in this thesis, a full assessment is made on ice-sheet variability during the past 40 million years. The inverse forward modelling approach is used to derive temperatures relative to PD from benthic δ^{18}O data, a prime climate proxy for past changes in ice volume and deep-water temperature. Firstly, in combination with five 1-D ice-sheet models a full 40 million year reconstruction of past temperature and sea level is created. The Cenozoic reconstruction is shown to be coherent with other model and observations of ice volume and is used to analyse the transient behaviour of the Earth's climate during this interval. Secondly, the temperature reconstructions is used to create a continuous CO_2 record over the past 20 million years in coherence with observations and proxies of CO_2. Thirdly, the inverse methodology is combined with four 3-D ice-sheet models, for a high-resolution assessment of ice volume and temperature variability during the past 1 million years. In this Chapter a short summary is given of the main results of both modelling experiments. Lastly, some shortcomings in the methodology are discussed together with future improvements that could be implemented.

7.1 Introduction

Knowledge on past climate change largely emerges from sediment records drilled from the ocean floor and ice-core records from the Antarctic and Greenland ice sheets. From these records proxy data is obtained indicating changes in, for example, temperature, sea level and greenhouse gas concentrations. A key parameter that emerges from the sediment records is the oxygen isotope ratio, δ^{18}O, from fossilised benthic foraminiferal shells ($CaCO_3$). The benthic δ^{18}O data serves as a proxy for changes in deep-water temperature and ice volume. In this thesis an inverse forward modelling approach (Bintanja et al., 2005a,b) has been used to decompose the benthic δ^{18}O data into an ice-volume and temperature contribution. With the use of ice-sheet models and a simplified deep-water temperature model a complete and self-consistent record of past changes in ice volume and temperature is reconstructed, in coherence with the benthic δ^{18}O observations.

During the Cenozoic era, the past 65 million years (Myr), the climate of the Earth has experienced significant changes in both prime climate variables, temperature and sea level. Both variables are strongly linked to changes in the Earth's cryosphere, i.e. fluctuations of land based ice masses, and to changes in greenhouse gas concentrations in the atmosphere. In the early part of the Cenozoic the climate was dominated by high levels of greenhouse gasses in the atmosphere, enhancing the greenhouse effect and leading to much higher surface-air temperatures in the atmosphere. During this period the Earth had no vast ice masses on land, such as the large Antarctic and Greenland ice sheets that are present today. From about 50 to 35 Myr ago the climate cooled drastically, mainly thought to be caused by a decrease in greenhouse gas concentrations in the atmosphere.

7.2 Results

7.2.1 Reconstruction over the past 40 Myr

Combining the inverse methodology with five 1-D ice-sheet models, records of ice volume and temperature were reconstructed over the past 40 Myr as derived from benthic δ^{18}O data shown in Chapter 3. At the Eocene-Oligocene transition, ca. 34 Myr ago, the first large ice sheet formed on Antarctica. During the Oligocene and early Miocene coherent fluctuations in both eustatic sea level (derived from ice volume) and temperature occur. A relative short interval in the middle Miocene, the Mid-Miocene climate optimum ($\sim$15 Myr ago) is shown to have an increase in temperatures and hence a smaller Antarctic ice sheet. Thereafter, temperatures decreased strongly again leading to the formation of the East Antarctic ice sheet close to its present day form. The reconstruction showed no large changes in ice volume during the following 10

Myr, whereas temperatures continued to decrease in coherence with the increase in benthic δ^{18}O. The decoupling of both variables during this period in time is mainly due to a fully glaciated AIS, but temperatures were too warm to initiate Northern Hemisphere (NH) glaciation. Modelled glaciation on the NH started about 3 Myr ago, leading to the Plio-Pleistocene glacial cycles that are related to Milankovich insolation forcing. The large fluctuations during the past 3 Myr are mainly caused by changes in the NH, predominantly by ice sheets on Eurasia and North America.

The use of a global coverage of ice volume changes, with different ice-sheet models, is important for interpreting the benthic δ^{18}O data in a transient mode as discussed in Chapter 4. The decoupling of temperature and sea level during the late Miocene is shown to be a quite distinctive period in time during the last 40 Myr, with a very low response of ice volume on changes in temperature (low $\Delta S/\Delta T$). The transient nature of the climate also emerges by comparing eustatic sea level changes, derived from ice volume, with changes in δ_w. Often, this relation is assumed constant over time for the interpretation of paleoclimate proxies. However, the 1-D model reconstruction shows that also for this relation there is quite some variability, demonstrating the importance of the self-consistent modelling approach used in this thesis.

7.2.2 Reconstructing CO_2

Following the long-term reconstruction of temperature, in Chapter 5 an analysis has been performed on changes of CO_2 concentrations in the atmosphere over the past 20 Myr. As can be deduced from the ice-core records over the past 800 kyr, there is a clear relation between temperature and CO_2, which is extracted from air bubbles trapped within the ice. Using the temperature reconstruction from the 1-D ice-sheet models, a variety of different CO_2 proxies are tested for their coherence with the ice-core data. Henceforth, the most coherent records are selected to derive a self-consistent and continuous CO_2 record over the past 20 Myr. Moreover, the long-term climate sensitivity of temperature to CO_2 changes is derived, which includes radiative forcing of CO_2, short and fast feedbacks and a correction for other greenhouse gasses. There is quite some uncertainty in the derived CO_2 reconstruction, related to both model and observations. Nevertheless, this theoretically derived relation is close to the model based climate sensitivity of temperature to CO_2, indicating that the key processes influencing CO_2 and benthic δ^{18}O are included in the reconstructions of temperature and CO_2. The large sensitivity derived here implies that subtle changes in atmospheric CO_2 could be related to the MPT and the initiation of NH glaciation.

7.2.3 3-D model reconstruction over the past 1 Myr

With comprehensive 3-D ice-sheet models including both the SIA and SSA, modelling sheet and shelf flow, a more in-depth analysis has been performed in Chapter 6

on ice volume changes over the past 1 Myr. Models for Antarctica, Greenland, Eurasia and North America are initialised with present-day topography, ice thickness and 30-year mean temperatures and precipitation. The inverse routine combined with the 3-D model creates the possibility to make a full assessment of the separate contribution of ice volume on sea-level and δ_w variations. For the first time the separate contributions of these four ice sheets have been calculated explicitly over this time interval. With respect to eustatic sea level, the large NH ice sheets are naturally responsible for the largest variability during the Plio-Pleistocene. Coherently, these ice sheets also provide the largest contribution to δ_w. The Antarctic and Greenland ice sheets contribute about 10% to changes in eustatic sea level. For δ_w the contribution is even larger, between 10 and 20%, mainly due to the relatively much lower $\delta^{18}O_i$ values of the Antarctic ice sheet.

Finally, the individual ice sheets are forced with a linear approximation of glacial climate variability. Most apparent is the difference between the AIS and the EuIS and NaIS in climate sensitivity to changes in sea level or temperature. Ice volume on Antarctica is increased due to lowering of sea level, which is enhanced by decreasing temperatures and hence lower shelf melt. On the contrary, ice growth on Eurasia and North America starts when temperatures drop, due to a positive surface mass balance. This is enhanced by a drop in sea level. Coherently, the AIS does not show a large response to a reduction of only temperature, and ice growth on Eurasia and North America does not start at all when only sea level is decreased. This shows the importance of the interaction between ice sheets and sea level, which in the full coupled model with four ice sheets is internally calculated from ice volume changes relative to present day.

7.3 Conclusions

In this thesis, it is shown that both 1-D and 3-D models can be used to analyse climate on different time scales. Although both models have their own shortcomings, both have shown their value in investigating past climate change and do show coherent changes in temperature and ice volume over long time scales. Because of the simplified geometry of the 1-D model it is possible to analyse long-term climate change. With the five ice-sheet models used here a full glacial reconstruction has been created over the past 40 Myr. Additionally, it is easy to test the sensitivity of the model to different parameterisations and assess the uncertainty over these long time scales. The 3-D model, however, is far more sophisticated and therefore restricted to be used for shorter time scales up to a few million years. Naturally, with these models a much more realistic reconstruction can been made over this time span. The models provide much more detail in the exact behaviour of the regional ice volume fluctuations and the related changes in temperature. In summary, the combination of the inverse

methodology with ice-sheet models covering global glaciation is shown to be of great use for interpreting paleoclimate proxies. Furthermore, the reconstructed sea level, temperature and atmospheric CO_2 are coherent with the benthic $\delta^{18}O$ data, yielding a self-consistent record of past climate variability over long time scales.

7.4 Outlook

Coupling to a simplified climate model

Although the results show a coherent picture of temperature, ice volume and CO_2, there are several aspects that can be improved related to the parameterisations used to simulate climate change. One of the major simplifications in this thesis is the deep-ocean temperature parameterisation, for which a linear relation is used between deep-water temperature change and ΔT_{NH}, incorporating a time lag. Coupling the 3-D models to a climate model, including atmosphere and oceans, would yield a stronger physical basis for deep-ocean temperatures. For the long-term climate change, the use of a simplified climate model, rather than much more sophisticated GCMs, has the advantage to keep additional computational demands to a minimum. With the use of a Zonally averaged Energy Balance Climate model (ZEBCM, e.g. North (1975); Bintanja (1997)), temperatures both in the atmosphere and deep ocean are calculated as function of the latitude. Therefore, no additional assumptions are needed to include differences between the two hemispheres as used in the current setup. Lastly, changes in greenhouse gas forcing could be included in the atmosphere combined with a carbon-cycle model (e.g. Köhler and Fischer, 2006; Köhler and Bintanja, 2008). Hence, including the influence of, for example, pCO_2 on air temperatures and transmissivity in the energy balance of the atmosphere. This will eventually also allow to incorporate modelling of $\delta^{13}C$ for an independent comparison with paleo data.

Regional sea level variations

A second issue concerns the interaction of ice sheets with changes in regional sea level. So far, changes in ice volume are uniformly divided over the surface area of the oceans, hence calculating eustatic sea level change. As has been shown by for example Raymo et al. (2011), regional sea level changes deviate quite significantly from eustatic sea level. Due to the gravitational attraction of additional ice mass during ice-sheet growth, changes in earth loading and therefore glacial isostatic adjustment, regional sea level would actually increase near the ice-sheet margin. In contrary to eustatic sea level that will lower due to the evaporation of ocean water that forms precipitation over the ice sheet. In Chapter 6, the short experiments with simplified artificial changes in temperature and sea level have shown that there is a clear interaction with local sea level change for ice sheets on both hemispheres. Regional changes

in sea level can be calculated with a so called 'sea-level equation' model (e.g. Spada and Stocchi, 2007; Slangen et al., 2011). In combination with the 3-D ice-sheet models this would allow for a more realistic treatment of: the hysteresis of ice volume; the strongly related response of ice sheets to sea level changes; and the lead and lags of ice volume changes of the individual ice sheets.

Bibliography

Alvarez, L. W., W. Alvarez, F. Asaro and H. V. Michel, 1980. Extraterrestrial cause for the Cretaceous-Tertiary extinction, *Science*, **208**(4448), 1095–1108.

Bamber, J. L. and R. L. Layberry, 2001. A new ice thickness and bed data set for the Greenland ice sheet 1. Measurements, data reduction, and errors, *J. Geophys. Res.*, **106**.

Bartoli, G., M. Sarnthein, M. Weinelt, H. Erlenkeuser, D. Garbe-Schönberg and D.W. Lea, 2005. Final closure of Panama and the onset of northern hemisphere glaciation, *Earth Planet. Sci. Lett.*, **237**, 33–44.

Becker, J. J., D. T. Sandwell, W. H. F. Smith, J. Braud, B. Binder, J. Depner, D. Fabre, J. Factor, S. Ingalls, S-H. Kim, R. Ladner, K. Marks, S. Nelson, A. Pharaoh, R. Trimmer, J. Von Rosenberg, G. Wallace and P. Weatherall, 2009. Global Bathymetry and Elevation Data at 30 Arc Seconds Resolution: SRTM30_PLUS, *Marine Geodesy*, **32**(4), 355–371.

Beckmann, A. and H. Goosse, 2003. A parameterization of ice shelf-ocean interaction for climate models, *Ocean Modelling*, **5**(2), 157–170.

Beerling, D. J. and D. L. Royer, 2011. Convergent Cenozoic CO_2 history, *Nature Geosci*, **4**, 418–420.

Berger, A. and M.F. Loutre, 1992. Astronomical solutions for paleoclimate studies over the last 3 million years, *Earth and Plan. Sc. Let.*, **111**, 369–382.

Berger, A., M. F. Loutre and H. Gallée, 1998. Sensitivity of the LLN climate model to the astronomical and CO_2 forcings over the last 200 ky, *Clim. Dyn.*, **14**, 615–629.

Berger, A. L., 1992. Astronomical theory of Paleoclimates and the last glacial-interglacial cycle, *Quat. Sci. Rev.*, **11**(5), 571–581.

Berner, R. A., 1994. GEOCARB II; a revised model of atmospheric CO 2 over Phanerozoic time, *Am J Sci*, **294**, 56–91.

Bijl, P. K., A. J. P. Houben, S. Schouten, S. M. Bohaty, A. Sluijs, G.-J. Reichart, J. S. Sinninghe Damste and H. Brinkhuis, 2010. Transient Middle Eocene Atmospheric CO_2 and Temperature Variations, *Science*, **330**, 819–821.

Bintanja, R., 1997. Sensitivity experiments performed with an energy balance atmosphere model coupled to an advection-diffusion ocean model, *Theor. Appl. Climatol.*, **56**, 1–24.

Bintanja, R. and J. Oerlemans, 1996. The effect of reduced ocean overturning on the climate of the last glacial maximum, *Climate Dynamics*, **12**, 523–533.

Bintanja, R. and R. S. W. Van de Wal, 2008. North American ice-sheet dynamics and the onset of 100,000-year glacial cycles, *Nature*, **454**, 869–872.

Bintanja, R., R. S. W. Van de Wal and J. Oerlemans, 2002. Global ice volume variations through the last glacial cycle simulated by a 3-D ice-dynamical model, *Quat. Int.*, **95-96**, 19–23.

Bintanja, R., R. S. W. Van de Wal and J. Oerlemans, 2005a. Modelled atmospheric temperatures and global sea level over the past million years, *Nature*, **437**, 125–128.

Bintanja, R., R. S. W. Van de Wal and J. Oerlemans, 2005b. A new method to estimate ice age temperatures, *Clim. Dyn.*, **24**, 197–211.

Bohaty, S. M., J. C. Zachos, F. Florindo and M. L. Delaney, 2009. Coupled greenhouse warming and deep-sea acidification in the middle Eocene, *Paleoceanography*, **24**(2).

Braconnot, P., B. Otto-Bliesner, S. Harrison, S. Joussaume, J.-Y. Peterchmitt, A. Abe-Ouchi, M. Crucifix, E. Driesschaert, Th. Fichefet, C. D. Hewitt, M. Kageyama, A. Kitoh, A. Laîné, M.-F. Loutre, O. Marti, U. Merkel, G. Ramstein, P. Valdes, S. L. Weber, Y. Yu and Y. Zhao, 2007. Results of PMIP2 coupled simulations of the Mid-Holocene and Last Glacial Maximum - Part 1: experiments and large-scale features, *Clim. Past*, **3**(2), 261–277.

Brewer, S., J. Guiot, M. F. Sánchez-GoÒi and S. Klotz, 2008. The climate in Europe during the Eemian: a multi-method approach using pollen data, *Quaternary Science Reviews*, **27**(25-26), 2303–2315.

Brohan, P., J. J. Kennedy, Harris I., Tett S. F. B. and P. D. Jones, 2006. Uncertainty estimates in regional and global observed temperature changes: A new data set from 1850, *J. Geophys. Res.*, **111**.

Bueler, E. and J. Brown, 2009. Shallow shelf approximation as a "sliding law" in a thermomechanically coupled ice sheet model, *J. Geophys. Res.*, **114**, f03008.

Chappell, J. and N. J. Shackleton, 1986. Oxygen isotopes and sea level, *Nature*, **324**, 137–140.

Charney, J. G., A. Arakawa, D. J. Baker, B. Bolin, R. E. Dickinson, R. M. Goody, C. E. Leith, H. M. Stommel and C. I. Wunsch, 1979. Carbon Dioxide and Climate: A Scientific Assessment, National Academy of Science.

Clark, P. U., D. Archer, D. Pollard, J. D. Blum, J. A. Rial, V. Brovkin, A. C. Mix, N. G. Pisias and M. Roy, 2006. The middle Pleistocene transition: characteristics, mechanisms, and implications for long-term changes in atmospheric pCO_2, *Quat. Sci. Rev.*, **25**(23-24), 3150–3184.

Clark, P. U. and D. Pollard, 1998. Origin of the Middle Pleistocene Transition by Ice Sheet Erosion of Regolith, *Paleoceanography*, **13**(1), 1–9.

Clarke, G. K. C., 2005. Subglacial processes, *Ann. Rev. Earth Planet. Sc.*, **33**, 247–276.

Clarke, G. K. C., N. Lhomme and S. J. Marshall, 2005. Tracer transport in the Greenland ice sheet: three-dimensional isotopic stratigraphy, *Quat. Sci. Rev.*, **24**, 155–171.

CLIMAP Project members, 1976. The surface of the ice-age earth, *Science*, **191**, 793–796.

Conway, H., Hall B.L., G.H. Denton, A.M. Gades and E.D. Waddington, 1999. Past and future grounding-line retreat of the West Antarctic Ice Sheet, *Science*, **286**, 280–283.

Coxall, H. K., P. A. Wilson, H. Palike, C. H. Lear and J. Backman, 2005. Rapid stepwise onset of Antarctic glaciation and deeper calcite compensation in the Pacific Ocean, *Nature*, **433**, 53–57.

Cramer, B. S., J. R. Toggweiler, J. D. Wright, M. E. Katz and K. G. Miller, 2009. Ocean overturning since the Late Cretaceous: Inferences from a new benthic foraminiferal isotope compilation, *Paleoceanography*, **24**(4).

Cuffey, K. M., 2000. Methodology for use of isotopic climate forcings in ice sheet models, *Geophys. Res. Lett.*, **27**(19), 3065–3068.

Dansgaard, W., 1964. Stable isotopes in precipitation, *Tellus*, **16**, 436–468.

DeConto, R. M. and D. Pollard, 2003a. A coupled climate-ice sheet modeling approach to the early Cenozoic history of the Antarctic ice sheet, *Palaeogeogr. Palaeoclimatol. Palaeoecol.*, **198**, 39–42.

DeConto, R. M. and D. Pollard, 2003b. Rapid Cenozoic glaciation of Antarctica triggered by declining atmospheric CO_2, *Nature*, **421**, 245–249.

Schneider von Deimling, T., A. Ganopolski, H. Held and S. Rahmstorf, 2006. How cold was the Last Glacial Maximum?, *Geophys. Res. Lett.*, **33**(14).

Dekens, P. S., A. C. Ravelo, M. D. McCarthy and C. A. Edwards, 2008. A 5 million year comparison of Mg/Ca and alkenone paleothermometers, *Geochem. Geophys. Geosyst.*, **9**(10).

Duplessy, J.-C., L. Labeyrie and C. Waelbroeck, 2002. Constraints on the ocean oxygen isotopic enrichment between the Last Glacial Maximum and the Holocene: Paleoceanographic implications, *Quat. Sc. Rev.*, **21**, 315–330.

Edwards, M., 1992. Global Gridded Elevation and Bathymetry, in Kineman, J.J., and Ohrenschall, M.A., eds., Global Ecosystems Database, Version 1.0 (on CD-ROM), Documentation Manual, Disc-A: National Geophysical Data Center, Key to Geophysical Records Documentation No. 26 (Incorporated in: Global Change Database, Volume 1): Boulder, CO, National Oceanic and Atmospheric Administration, Pages = A14-1 to A14-4,.

Ehlers, J. and P. L. Gibbard, 2007. The extent and chronology of Cenozoic Global Glaciation, *Quaternary International*, **164-165**, 6–20.

Elderfield, H., M. Greaves, S. Barker, I. R. Hall, A. Tripati, P. Ferretti, S. Crowhurst, L. Booth and C. Daunt, 2010. A record of bottom water temperature and seawater δ^{18}O for the Southern Ocean over the past 440 kyr based on Mg/Ca of benthic foraminiferal Uvigerina spp., *Quaternary Science Reviews*, **29**(1-2), 160–169.

Emiliani, C., 1955. Pleistocene temperatures, *J. Geol.*, **63**, 538–578.

Epica Community Members, 2006. One-to-one interhemispheric coupling of millennial polar climate variability during the last glacial, *Nature*, **444**, 195–198.

Etourneau, J., P. Martinez, T. Blanz and R. Schneider, 2009. Pliocene-Pleistocene variability of upwelling activity, productivity, and nutrient cycling in the Benguela region, *Geology*, **37**(10), 871–874.

Fairbanks, R. G., 1989. A 17,000-year glacio-eustatic sea level record: influence of glacial melting rates on the Younger Dryas event and deep-ocean circulation, *Nature*, **342**(6250), 637–642.

Fan, Y. and H. van den Dool, 2008. A global monthly land surface air temperature analysis for 1948 – present, *J. Geophys. Res.*, **113**.

Foster, G. L., D. J. Lunt and R. R. Parrish, 2010. Mountain uplift and the glaciation of North America –a sensitivity study, *Clim. Past*, **6**(5), 707–717.

Foster, G. L., Y. Ni, B. Haley and T. Elliott, 2006. Accurate and precise isotopic measurement of sub-nanogram sized samples of foraminiferal hosted boron by total evaporation NTIMS, *Chemical Geology*, **230**, 161 – 174.

Ganopolski, A., R. Calov and M. Claussen, 2010. Simulation of the last glacial cycle with a coupled climate ice-sheet model of intermediate complexity, *Clim. Past*, **6**(2), 229–244.

Gat, J. R., W. G. Mook and H. A. J. Meijer, 2001. Environmental isotopes in the hydrological cycle, Principles and applications: Volume II, Atmospheric water, UNESCO, Paris.

Giovinetto, M.B. and H.J. Zwally, 1997. Areal distribution of the oxygen-isotope ratio in Antarctica: an assessment based on multivariate models, *Ann. Glaciol.*, **25**, 153–158.

Gladstone, R. M., A. J. Payne and S. L. Cornford, 2010. Parameterising the grounding line in flow-line ice sheet models, *The Cryosphere*, **4**(4), 605–619.

GRIP Members, 1993. Climate instability during the last interglacial period recorded in the GRIP ice core, *Nature*, **364**, 203–207.

Hansen, J., M. Sato, P. Kharecha, D.J. Beerling, R. Berner, V. Masson-Delmotte, Mark Pagani, Maureen E. Raymo, Dana L. Royer and James C. Zachos, 2008. Target Atmospheric CO_2: Where should humanity Aim?, *The Open Atmoshperic Science Journal*, **2**, 217–231.

Hargreaves, J. C., A. Abe-Ouchi and J. D. Annan, 2007. Linking glacial and future climates through an ensemble of GCM simulations, *Clim. Past*, **3**(1), 77–87.

Hays, J., J. Imbrie and N.J. Shackleton, 1976. Variation in the Earth's orbit: pacemakers of the ice ages, *Science*, **194**, 1121–1132.

Haywood, A. M., M. A. Chandler, P. J. Valdes, U. Salzmann, D. J. Lunt and H. J. Dowsett, 2009. Comparison of mid-Pliocene climate predictions produced by the HadAM3 and GCMAM3 General Circulation Models, *Glob. Planet. Change*, **66**(3-4), 208–224.

Helsen, M. M., 2006. On the interpretation of stable isotopes in Antarctic precipitation, PhD thesis, Utrecht University.

Henrot, A. J., L. François, E. Favre, M. Butzin, M. Ouberdous and G. Munhoven, 2010. Effects of CO_2, continental distribution, topography and vegetation changes on the climate at the Middle Miocene: a model study, *Clim. Past*, **6**(5), 675–694.

Herbert, T. D., L. C. Peterson, K. T. Lawrence and Z. Liu, 2010. Tropical Ocean Temperatures Over the Past 3.5 Million Years, *Science*, **328**, 1530–1534.

Holbourn, A., W. Kuhnt, M. Schulz and H. Erlenkeuser, 2005. Impacts of orbital forcing and atmospheric carbon dioxide on Miocene ice-sheet expansion, *Nature*, **438**, 483–487.

Hönisch, B., N. G. Hemming, D. Archer, M. Siddall and J. F. McManus, 2009. Atmospheric Carbon Dioxide Concentration Across the Mid-Pleistocene Transition, *Science*, **324**, 1551–1554.

Huber, M., H. Brinkhuis, C. E. Stickley, K. Döös, A. Sluijs, J. Warnaar, S. A. Schellenberg and G. L. Williams, 2004. Eocene circulation of the Southern Ocean: Was Antarctica kept warm by subtropical waters?, *Paleoceanography*, **19**(4).

Huber, M. and R. Caballero, 2011. The early Eocene equable climate problem revisited, *Clim. Past*, **7**, 603–633.

Hutter, L., 1983. Theoretical Glaciology, D. Reidel, Dordrecht.

Huybers, P., 2007. Glacial variability over the last two million years: an extended depth-derived agemodel, continuous obliquity pacing, and the Pleistocene progression, *Quat. Sci. Rev.*, **26**, 37–55.

Huybrechts, P., 1990. A 3-D model for the Antarctic ice sheet: a sensitivity study on the glacial-interglacial contrast., *Clim. Dyn.*, **5**(2), 79–92.

Huybrechts, P., 1992. The Antarctic ice sheet and environmental change: a three-dimensional modelling study, PhD thesis, Geografisch Instituut, Vrije Universiteit Brussel.

Huybrechts, P., 2002. Sea-level changes at the LGM from ice-dynamic reconstructions of the Greenland and Antarctic ice sheets during the glacial cycles, *Quat. Sci. Rev.*, **21**, 203–231.

Huybrechts, P. and J. de Wolde, 1999. The Dynamic Response of the Greenland and Antarctic Ice Sheets to Multiple-Century Climatic Warming, *Journal of Climate*, **12**(8), 2169–2188.

Imbrie, J., A.L. Berger, E. A. Boyle, S. C. Clemens, A. Duffy, W. R. Howard, G. Kukla, J. Kutzback, D. G. Martinson, A. McIntyre, A. C. Mix, B. Molfino, J. J. Morley, L. C. Peterson, N. G. Pisias, W. L. Prell, M. E. Raymo, N. J. Shackleton and J. R. Toggweiler, 1993. On the structure and origin of major glaciation cycles 2. The 100,000-year cycle, *Paleoceanography*, **8**, 699–735.

Imbrie, J., E. A. Boyle, S. C. Clemens, A. Duffy, W. R. Howard, G. Kukla, J. Kutzbach, D. G. Martinson, A. McIntyre, A. C. Mix, B. Molfino, J. J. Morley, L. C. Peterson, N. G. Pisias, W. L. Prell, M. E. Raymo, N. J. Shackleton and J. R. Toggweiler, 1992. On the Structure and Origin of Major Glaciation Cycles 1. Linear Responses to Milankovitch Forcing, *Paleoceanography*, **7**(6), 701–738.

Imbrie, J. and J. Z. Imbrie, 1980. Modeling the Climatic Response to Orbital Variations, *Science*, **207**(4434), 943–953.

Jansen, E. J., J. Overpeck, K. R. Briffa, J.-C. Duplessey, F. Joos, V. Masson-Delmotte, D. Olago, B. Otto-Bliesner, W. R. Peltier, S. Rahmstorf, R. Ramesh, D. Raynaud, D. Rind, O. Solomina, R. Villalba and D. Zhang, 2007. Paleoclimate, In Climate change 2007: The physical Science basis. Contribution of Working Group I to the Fourth Assessment Report of the Intergovernmental Panel on Climate Change, Cambridge University Press, Cambridge, United Kingdom and New York, NY, USA, chap. 6, 433–497.

Janssens, I. and P. Huybrechts, 2000. The treatment of meltwater retention in mass-balance parameterizations of the Greenland ice sheet, *Ann. Glaciol.*, **31**, 133–140.

Jouzel, J., N. I. Barkov, J. M. Barnola, M. Bender, J. Chappellaz, C. Genthon, V. M. Kotlyakov, V. Lipenkov, C. Lorius, J. R. Petit, D. Raynaud, G. Raisbeck, C. Ritz, T. Sowers, M. Stievenard, F. Yiou and P. Yiou, 1993. Extending the Vostok ice-core record of palaeoclimate to the penultimate glacial period, *Nature*, **364**, 407–412.

Jouzel, J., V. Masson-Delmotte, O. Cattani, G. Dreyfus, S. Falourd, G. Hoffmann, B. Minster, J. Nouet, J. M. Barnola, J. Chappellaz, H. Fischer, J. C. Gallet, S. Johnsen, M. Leuenberger, L. Loulergue, D. Luethi, H. Oerter, F. Parrenin, G. Raisbeck, D. Raynaud, A. Schilt, J. Schwander, E. Selmo, R. Souchez, R. Spahni, B. Stauffer, J. P. Steffensen, B. Stenni, T. F. Stocker, J. L. Tison, M. Werner and E. W. Wolff, 2007. Orbital and Millennial Antarctic Climate Variability over the Past 800,000 Years, *Science*, **317**, 793–796.

Kageyama, M., S. Charbit, C. Ritz, M. Khodri and G. Ramstein, 2004. Quantifying ice-sheet feedbacks during the last glacial inception, *Geophys. Res. Lett.*, **31**(24).

Kennett, J. P. and L. D. Stott, 1991. Abrupt deep-sea warming, palaeoceanographic changes and benthic extinctions at the end of the Palaeocene, *Nature*, **353**, 225–229.

Köhler, P. and R. Bintanja, 2008. The carbon cycle during the Mid Pleistocene Transition: the Southern Ocean Decoupling Hypothesis, *Climate of the Past*, **4**(4), 311–332.

Köhler, P., R. Bintanja, H. Fischer, F. Joos, R. Knutti, G. Lohmann and V. Masson-Delmotte, 2010. What caused Earth's temperature variations during the last 800,000 years? Data-based evidence on radiative forcing and constraints on climate sensitivity, *Quat. Sci. Rev.*, **29**, 129–145.

Köhler, P. and H. Fischer, 2006. Simulating low frequency changes in atmospheric CO_2 during the last 740 000 years, *Clim. Past*, **2**, 57–78.

Kominz, M. A., J. V. Browning, K. G. Miller, P. J. Sugarman, S. Mizintseva and C. R. Scotese, 2008. Late Cretaceous to Miocene sea-level estimates from the New Jersey and Delaware coastal plain coreholes: an error analysis, *Basin Research*, **20**, 211–226.

Kürschner, W. M., J. van der Burgh, H. Visscher and D. L. Dilcher, 1996. Oak leaves as biosensors of late Neogene and early Pleistocene paleoatmospheric CO_2 concentrations, *Marine Micropaleontology*, **27**, 299–312.

Kürschner, W. M., Z. Kvacek and D. L. Dilcher, 2008. The impact of Miocene atmopsheric carbon dioxide fluctuations on climate and the evolution of terrestial ecosystems, *PNAS*, **105**, 440–453.

Lambeck, K. and J. Chappell, 2001. Sea level change through the last glacial cycle, *Sciene*, **292**, 679–686.

Langebroek, P. M., A. Paul and M. Schulz, 2009. Antarctic ice-sheet response to atmospheric CO_2 and insolation in the Middle Miocene, *Climate of the Past*, **5**(4), 633–646.

Langebroek, P. M., A. Paul and M. Schulz, 2010. Simulating the sea level imprint on marine oxygen isotope records during the middle Miocene using an ice sheet-climate model, *Paleoceanography*, **25**(4).

Laskar, J., P. Robutel, F. Joutel, M. Gastineau, A. C. M. Correia and B. Levrard, 2004. A long-term numerical solution for the insolation quantaties of the Earth, *Astron. Astroph.*, **428**, 261–285.

Le Brocq, A. M., A. J. Payne and A. Vieli, 2010. An improved Antarctic dataset for high resolution numerical ice sheet models (ALBMAP v1), *Earth Syst. Sci. Data*, **2**(2), 247–260.

Lear, C. H., T. R. Bailey, P. N. Pearson, H. K. Coxall and Y. Rosenthal, 2008. Cooling and ice growth across the Eocene-Oligocene transition, *Geology*, **36**(3), 251–254.

Lear, C. H., Elderfield H. and P. A. Wilson, 2000. Cenozoic deep-sea temperatures and global ice volumes from Mg/Ca in benthic foraminiferal calcite, *Science*, **287**, 269–272.

Lear, C. H., E. M. Mawbey and Y. Rosenthal, 2010. Cenozoic benthic foraminiferal Mg/Ca and Li/Ca records: Toward unlocking temperatures and saturation states, *Paleoceanography*, **25**(4).

Lhomme, N. and G. K. C. Clarke, 2005. Global budget of water isotopes inferred from polar ice sheets, *Geophys. Res. Lett.*, **32**.

Liebrand, D., L. J. Lourens, D. A. Hodell, B. De Boer, R. S. W. Van de Wal and H. Pälike, 2011. Antarctic ice sheet and oceanographic response to eccentricity forcing during the early Miocene, *Climate of the Past*, **7**(3), 869–880.

Lisiecki, L. and M.E Raymo, 2005. A Pliocene stack of 57 globally distributed benthic δ^{18}O records, *Paleoceanography*, **20**.

Lisiecki, L. and M.E. Raymo, 2007. Plio-Pleistocene climate evolution: trends and transitions in glacial cycle dynamics, *Quat. Sci. Rev.*, **26**, 56–69.

Lisiecki, L. E., 2010. A benthic δ^{13}C-based proxy for atmospheric pCO_2 over the last 1.5 Myr, *Geophys. Res. Lett.*, **37**(21).

Littler, K., S. A. Robinson, P. R. Bown, A. J. Nederbragt and R. D. Pancost, 2011. High sea-surface temperatures during the Early Cretaceous Epoch, *Nature Geosci*, **4**(3), 169–172.

Liu, Z., M. Pagani, D. Zinniker, R. M. DeConto, M. Huber, H. Brinkhuis, S. R. Shah, R. M. Leckie and A. Pearson, 2009. Global cooling during the Eocene-Oligocene climate transition, *Science*, **323**, 1187–1190.

Lourens, L. J., J. Becker, R. Bintanja, F. J. Hilgen, E. Tuenter, R. S. W. Van de Wal and M. Ziegler, 2010. Linear and non-linear response of late Neogene glacial cycles to obliquity forcing and implications for the Milankovitch theory, *Quat. Sci. Rev.*, **29**, 352 – 365.

Lourens, L. J., A. Sluijs, D. Kroon, J. C. Zachos, E. Thomas, U. Rohl, J. Bowles and I. Raffi, 2005. Astronomical pacing of late Palaeocene to early Eocene global warming events, *Nature*, **435**(7045), 1083–1087.

Lourens, L. J. and E. Tuenter, 2009. The role of variations of the Earth's orbital characteristics in climate change, Letcher, Trevor M., ed., Climate change: Observed impacts on Planet Earth, Elsevier, 103–123.

Lüthi, D., M. Le Flock, B. Bereiter, T. Blunier, J.-M. Barnola, U. Siegenthaler, D. Raynaud, J. Jouzel, H. Fischer, K. Kawamura and T.F. Stocker, 2008. High-resolution carbon dioxide concentration record 650,000–800,000 years before present., *Nature*, **453**, 379–382.

Martin, M. A., R. Winkelmann, M. Haseloff, T. Albrecht, E. Bueler, C. Khroulev and A. Levermann, 2011. The Potsdam Parallel Ice Sheet Model (PISM-PIK) –Part 2: Dynamic equilibrium simulation of the Antarctic ice sheet, *The Cryosphere*, **5**(3), 727–740.

Masson-Delmotte, V., S. Hou, A. Ekaykin, J. Jouzel, A. Aristarain, R. T. Bernardo, D. Bromwich, O. Cattani, M. Delmotte, S. Falourd, M. Frezzotti, H. Gallée, L. Genoni, E. Isaksson, A. Landais, M. M. Helsen, G. Hoffmann, J. Lopez, V. Morgan and H. Motoyama, 2008. A Review of Antarctic Surface Snow Isotopic Composition: Observations, Atmospheric Circulation, and Isotopic Modeling., *J. Clim.*, **21**(13), 3359–3387.

Milankovitch, M., 1930. Mathematische Klimalehre und Astronomische Theorie der Klimaschwankungen, Gebruder Borntreger, Berlin.

Miller, K. G., M. A. Kominz, J. V. Browning, J. D. Wright, G. S. Mountain, M. E. Katz, P. J. Sugarman, B. S. Cramer, N. Christie-Blick and S. F. Pekar, 2005. The Phanerozoic record of global sea-level change, *Sciene*, **310**, 1293–1298.

Miller, K. G., J. D. Wright and R. G. Fairbanks, 1991. Unlocking the Ice House: Oligocene-Miocene Oxygen Isotopes, Eustasy, and Margin Erosion, *J. Geophys. Res.*, **96**(B4), 6829–6848.

Mix, A. C., J. Le and N. J. Shackleton, 1995. Benthic foraminiferal stable isotope stratigraphy from Site 846: 0-1.8 Ma., Pisias, N. G., L.A. Mayer, T.R. Janecek, A. Palmer-Julson and T. H. van Andel, eds., Proc. Ocean Drill. Program Sci. Results, vol. 138, 839–847.

Morland, L. W., 1987. Unconfined ice-shelf flow, de Veen, C. J. Van and J. Oerlemans, eds., Dynamics of the West Antarctic Ice Sheet, D. Reidel, 99–116.

Moucha, R., A. M. Forte, J. X. Mitrovica, D. B. Rowley, S. Quéré, N. A. Simmons and S. P. Grand, 2008. Dynamic topography and long-term sea-level variations: There is no such thing as a stable continental platform, *Earth Planet. Sci. Lett.*, **271**, 101–108.

Müller, R. D., M. Sdrolias, C. Gaine, B. Steinberger and C. Heine, 2008. Long-Term Sea-level Fluctuations Driven by Ocean Basin Dynamics, *Science*, **319**, 1357–1362.

Myhre, G., E. J. Highwood, K. P. Shine and F. Stordal, 1998. New estimates of radiative forcing due to well mixed greenhouse gases, *Geophys. Res. Lett.*, **25**(14), 2715–2718.

North, G. R., 1975. Theory of energy-balance climate models., *J. Atmos. Sci.*, **32**, 2033–2043.

Oerlemans, J., 1980. Model experiments on the 100,000-yr glacial cycle, *Nature*, **287**, 430–432.

Oerlemans, J., 1982. Glacial cycles and ice-sheet modelling, *Climatic Change*, **4**, 343–374.

Oerlemans, J., 2004a. Antarctic ice volume and deep-sea temperature during the last 50 Myr: a model study, *Ann. Glaciol.*, **39**, 13–19.

Oerlemans, J., 2004b. Correcting the Cenozoic δ^{18}O deep-sea temperature record for Antarctic ice volume, *Palaeog., Palaeocl., Palaeoec.*, **208**, 195–205.

Pagani, M., Z. Liu, J. LaRiviere and A. C. Ravelo, 2010. High Earth-system climate sensitivity determined from Pliocene carbon dioxide concentrations, *Nature Geosci.*, **3**, 27–30.

Pagani, M., J. C. Zachos, K. H. Freeman, B. Tipple and S. Bohaty, 2005. Marked Decline in Atmospheric Carbon Dioxide Concentrations During the Paleogene, *Science*, **309**(5734), 600–603.

Paillard, D., L. Labeyrie and P. Yiou, 1996. Macintosh program performs time-series analysis, *Eos Trans. AGU*, **77**, 379.

Pearson, P. N. and M. R. Palmer, 2000. Atmospheric carbon dioxide concentrations over the past 60 million years, *Nature*, **406**, 695–699.

Petit, J. R., J. Jouzel, D. Raynaud, N. I. Barkov, J. M. Barnola, I. Basile, M. Bender, J. Chappellaz, M. Davis, G. Delaygue, M. Delmotte, V. M. Kotlyakov, M. Legrand, V. Y. Lipenkov, C. Lorius, L. PEpin, C. Ritz, E. Saltzman and M. Stievenard, 1999. Climate and atmospheric history of the past 420,000 years from the Vostok ice core, Antarctica, *Nature*, **399**(6735), 429–436.

Pollard, D., 2010. A retrospective look at coupled ice sheet-climate modeling, *Clim. Change*, **100**(1), 173–194.

Pollard, D. and R. M. DeConto, 2007. A coupled ice-sheet/ice-shelf/sediment model applied to a marine-margin flowline: forced and unforced variations, Blackwell Publishing, chap. 2, Spec. Publ. 39, International Association of Sedimentologists, 37–52.

Pollard, D. and R. M. DeConto, 2009. Modelling West Antarctic ice sheet growth and collapse throught the past five million years, *Nature*, **458**, 329–332.

Raymo, M. E, 1994. The initiation of Northern Hemisphere glaciation, *Annu. Rev. Earth Planet. Sci.*, **22**, 353–383.

Raymo, Maureen E., Jerry X. Mitrovica, Michael J. O/'Leary, Robert M. DeConto and Paul J. Hearty, 2011. Departures from eustasy in Pliocene sea-level records, *Nature Geosci*, **4**, 328–332.

Reerink, T. J., M. A. Kliphuis and R. S. W. Van de Wal, 2010. Mapping technique of climate fields between GCM's and ice models, *Geoscientific Model Development*, **3**(1), 13–41.

Retallack, Gregory J., 2009. Greenhouse crises of the past 300 million years, *Geological Society of America Bulletin*, **121**(9-10), 1441–1455.

Robinson, A., R. Calov and A. Ganopolski, 2011. Greenland ice sheet model parameters constrained using simulations of the Eemian Interglacial, *Clim. Past*, **7**(2), 381–396.

Roe, G. H., 2002. Modeling precipitation over ice sheets: an assessment using Greenland, *J. Glaciol.*, **48**(160), 70–80.

Roe, G. H. and R. S. Lindzen, 2001. The Mutual Interaction between Continental-Scale Ice Sheets and Atmospheric Stationary Waves, *Journal of Climate*, **14**(7), 1450–1465.

Rohling, E. J., K. Grant, M. Bolshaw, A. P. Roberts, M. Siddall, Ch. Hemleben and M. Kucera, 2009. Antarctic temperature and global sea level closely coupled over the past five glacial cycles, *Nature Geosci.*, **2**, 500–504.

Royer, D. L., 2006. CO_2-forced climate thresholds during the Phanerozoic, *Geochimica et Cosmochimica Acta*, **70**(23), 5665–5675.

Ruddiman, W. F., 2003. Orbital insolation, ice volume, and greenhouse gasses, *Quat. Sci. Rev.*, **22**, 1597–1629.

Ruddiman, W. F., 2008. Earth's climate: Past en Future, W. H. Freeman and company, New York, second ed.

Ruddiman, W. F., 2010. A paleoclimatic Enigma?, *Science*, **328**, 838–839.

Sato, T. and K. Kameo, 1996. Pliocene to Quaternary calcareous nannofossil biostratigraphy of the Arctic ocean, with reference to Late Pliocene glaciation, Thiede, J., A.M. Myhre, J.V. Firth, G.L. Johnson and W.F. Ruddiman, eds., Proc. Ocean Drill. Program Sci. Results, vol. 151, 39–59.

Schoof, C., 2010. Coulomb friction and other sliding laws in a higher-order glacier flow model, *Math. Models Methods Appl. Sci.*, **20**(1), 157–189.

Schouten, S., E. C. Hopmans, E. Schefufl and J. S. Sinninghe DamstÈ, 2002. Distributional variations in marine crenarchaeotal membrane lipids: a new tool for reconstructing ancient sea water temperatures?, *Earth and Planetary Science Letters*, **204**(1-2), 265–274.

Schrag, D. P., J. F. Adkins, K McIntyre, J. L. Alexander, D. A. Hodell, C. D. Charles and J. F. McManus, 2002. The oxygen isotopic composition of seawater during the Last Glacial Maximum, *Quat. Sci. Rev.*, **21**, 331–342.

Seki, O., G. L. Foster, D. N. Schmidt, A. Mackensen, K. Kawamura and R. D. Pancost, 2010. Alkenone and boron-based Pliocene pCO_2 records, *Earth Planet. Sci. Lett.*, **292**, 201 – 211.

Shackleton, N. J., 1974. Attainment of isotopic equilibrium between ocean water and the benthonic foraminifera genus Uvigerina: isotopic changes in the ocean during the last glacial, *Cent. Nat. Sci. Colloq. Int.*, **219**, 203–209.

Shackleton, N. J., 2000. The 100.000-year ice-age cycle identified and found to lag temperature, carbon dioxide and orbital eccentricity, *Science*, **289**, 1897–1902.

Shackleton, N. J. and J. P. Kennett, 1975. Paleotemperature History of the Cenozoic and the Initiation of Antarctic Glaciation: Oxygen and Carbon Isotope Analyses in DSDP Sites 277, 279 and 281, *Initial Report Deep Sea Drilling Project*, **29**, 743–755.

Siddall, M., E. J. Rohling, A. Almogi-Labin, Ch. Hemleben, D. Meischner, I. Schmelzer and D. A. Smeed, 2003. Sea-level fluctuations during the last glacial cycle, *Nature*, **423**, 853–858.

Siegenthaler, U., T. F. Stocker, E. Monnin, D. Luthi, J. Schwander, B. Stauffer, D. Raynaud, J.-M. Barnola, H. Fischer, V. Masson-Delmotte and J. Jouzel, 2005. Stable Carbon Cycle-Climate Relationship During the Late Pleistocene, *Science*, **310**, 1313–1317.

Sima, A., A. Paul, M. Schulz and J. Oerlemans, 2006. Modeling the oxygen-isotopic composition of the North American Ice Sheet and its effect on the isotopic composition of the ocean during the last glacial cycle, *Geophys. Res. Lett.*, **33**(15).

Singarayer, J. S. and P. J. Valdes, 2010. High-latitude climate sensitivity to ice-sheet forcing over the last 120 kyr, *Quat. Sci. Rev.*, **29**, 43–55.

Slangen, A. B. A., C. A. Katsman, R. S. W. Van de Wal, L. L. A. Vermeersen and R. E. M. Riva, 2011. Towards regional projections of twenty-first century sea-level change based on IPCC SRES scenarios, *Climate Dynamics*, 1–19.

Sluijs, A., S. Schouten, M. Pagani, M. Woltering, H. Brinkhuis, J. S. Sinninghe Damsté, G. R. Dickens, M. Huber, G.-J. Reichart, R. Stein, J. Matthiessen, L. J. Lourens, N. Pedentchouk, J. Backman, K. Moran and the Expedition 302 Scientists, 2006. Subtropical Arctic Ocean temperatures during the Palaeocene/Eocene thermal maximum, *Nature*, **441**, 610–613.

Snyder, J. P., 1987. Map projections - A working manual; available at: http://pubs.er.usgs.gov/usgspubs/pp/pp1395, USGS Professional Paper 1395.

Sosdian, S. and Y. Rosenthal, 2009. Deep-Sea Temperature and Ice Volume Changes Across the Pliocene-Pleistocene Climate Transitions, *Science*, **325**, 306–310.

Sowers, T., M. Bender, L. Labeyrie, D. Martinson, J. Jouzel, D. Raynaud, J. J. Pichon and Y. S. Korotkevich, 1993. A 135,000-Year Vostok-Specmap Common Temporal Framework, *Paleoceanography*, **8**(6), 737–766.

Spada, G. and P. Stocchi, 2007. SELEN: A Fortran 90 program for solving the "sea-level equation", *Computers & Geosciences*, **33**(4), 538–562.

Tarasov, L. and W. R. Peltier, 1997. Terminating the 100 kyr ice age cycle, *J. Geophys. Res.*, **102**, 21655–21693.

Tarasov, L. and W. R. Peltier, 2003. Greenland glacial history, borehole constraints, and Eemian extent, *J. Geophys. Res.*, **108**.

Tripati, A. and H. Elderfield, 2005. Deep-Sea Temperature and Circulation Changes at the Paleocene-Eocene Thermal Maximum, *Science*, **308**(5730), 1894–1898.

Tripati, A. K., C. D. Roberts and R. A. Eagle, 2009. Coupling of CO_2 and Ice Sheet Stability Over Major Climate Transitions of the Last 20 Million Years, *Science*, **326**(5958), 1394–1397.

Tziperman, E. and H. Gildor, 2003. On the mid-Pleistocene transition to 100-kyr glacial cycles and the asymmetry between glaciation and deglaciation times, *Paleoceanography*, **18**.

Uppala, S. M. et al., 2005. The ERA-40 re-analysis, *Quart. J. Roy. Meteor. Soc.*, **131**, 2961–3012.

Van den Berg, J., R.S.W. Van de Wal and J. Oerlemans, 2006. Effects of spatial discretization in ice-sheet modelling using the shallow-ice approximation, *J. Glaciol.*, **52**(176), 89–98.

Van den Berg, J., R. S. W. Van de Wal and J. Oerlemans, 2008. A mass balance model for the Eurasian Ice Sheet for the last 120,000 years, *Glob. and Plan. Change*, **61**, 194–208.

Van Tuyll, C. I., R. S. W. van de Wal and J. Oerlemans, 2007. The response of a simple Antarctic ice-flow model to temperature and sea-level fluctuations over the Cenozoic era, *Ann. Glaciol.*, **46**, 69–77.

Van der Veen, C. J., 1999. Fundamentals of glacier dynamics, A.A. Balkema Publishers, Rotterdam.

Waelbroeck, C., L. Labeyrie, E. Michel, J. C. Duplessy, J. F. McManus, K. Lambeck, E. Balbon and M. Labracherie, 2002. Sea-level and deep water temperature changes derived from benthic foraminifera isotopic records, *Quat. Sci. Rev.*, **21**, 295–305.

Van de Wal, R. S. W., 1999a. The importance of thermodynamics for modeling the volume of the Greenland ice sheet, *J. Geophys. Res.*, **104**, 3887–3898.

Van de Wal, R. S. W., 1999b. Processes of buildup and retreat of the Greenland ice sheet, *J. Glaciol.*, **104**, 3899–3906.

Wang, Y., S. Hou, V. Masson-Delmotte and J. Jouzel, 2009. A new spatial distribution map of δ^{18}O in Antarctic surface snow, *Geophys. Res. Lett.*, **36**(6).

Weertman, J., 1957. On the sliding of glaciers, *J. Glaciol.*, **3**, 33–38.

Whitman, J. M. and W. H Berger, 1992. Pliocene-Pleistocene oxygen isotope record Site 586, Ontong Java Plateau, *Mar. Micropal.*, **18**, 171–198.

Wilschut, F., R. Bintanja and R. S. W. Van de Wal, 2006. Ice-sheet modelling characteristics in sea-level-based temperature reconstructions over the last glacial cycle, *J. Glaciol.*, **52**, 149–158.

Winkelmann, R., M. A. Martin, M. Haseloff, T. Albrecht, E. Bueler, C. Khroulev and A. Levermann, 2011. The Potsdam Parallel Ice Sheet Model (PISM-PIK) –Part 1: Model description, *The Cryosphere*, **5**(3), 715–726.

You, Y., M. Huber, R. D. Müller, C. J. Poulsen and J. Ribbe, 2009. Simulation of the Middle Miocene Climate Optimum, *Geophys. Res. Lett.*, **36**.

Zachos, J., M. Pagani, L. Sloan, E. Thomas and K. Billups, 2001. Trends, Rhythms, and Aberrations in Global Climate 65 Ma to Present, *Science*, **292**, 686–693.

Zachos, J. C., G. R. Dickens and R. E. Zeebe, 2008. An early Cenozoic perspective on greenhouse warming and carbon-cycle dynamics, *Nature*, **451**, 279–283.

Zachos, J. C., U. Röhl, S. A. Schellenberg, A. Sluijs, D. A. Hodell, D. C. Kelly, E. Thomas, M. Nicolo, I. Raffi, L. J. Lourens, H. McCarren and D. Kroon, 2005. Rapid Acidification of the Ocean During the Paleocene-Eocene Thermal Maximum, *Science*, **308**(5728), 1611–1615.

Zeebe, R. E. and D. A. Wolf-Gladrow, 2001. CO_2 in seawater: Equilibrium, Kinetics, Isotopes, vol. 65, Elsevier Science Publishing, Elsevier Oceanography Book Series.

Ziegler, M., L. J. Lourens, E. Tuenter, F. Hilgen, G.-J. Reichart and N. Weber, 2010. Precession phasing offset between Indian summer monsoon and Arabian Sea productivity linked to changes in Atlantic overturning circulation, *Paleoceanography*, **25**(3).

Zwally, H. J. and M. B. Giovinetto, 1997. Areal distribution of the oxygen-isotope ratio in Greenland,, *Ann. Glaciol.*, **25**, 208–213.

Zweck, C. and P. Huybrechts, 2005. Modeling of the northern hemisphere ice sheets during the last glacial cycle and glaciological sensitivity, *J. Geophys. Res.*, **110**.

Dankwoord

Vanaf deze plaats wil ik iedereen bedanken die op wat voor manier dan ook heeft bijgedragen aan het tot stand komen van dit proefschrift: BEDANKT! Op de eerste plaats wil ik graag Roderik bedanken. Na het afronden van mijn studie was ik even zoekende naar een vervolg, ik wist wel dat ik graag een promotieonderzoek wilde gaan doen, maar waar en bij wie? In deze periode heb je me in een aantal gesprekken goed op weg geholpen. Uiteindelijk kreeg ik de kans aangeboden voor het hier opgeschreven werk. Hiervoor ben ik je heel dankbaar! Ik had van te voren niet gedacht dat ik het zo leuk zou vinden! Het was heel fijn om met je samen te werken en ik ben ook blij dat we dit een vervolg kunnen geven. In deze wil ik ook Hans bedanken voor het geven van deze kans en het vertrouwen in ons verdere onderzoek. Lucas en Richard bedankt voor jullie inbreng in het project. Ik ben blij dat ik het middelpunt mocht (en mag) zijn van zoveel kennis uit verschillende richtingen, ook jullie bijdrage was onmisbaar geweest. Lucas ook bedankt voor het vertrouwen, mooi dat onze samenwerking wordt voortgezet. Erik Tuenter ook bedankt voor je inbreng. Peter Köhler thank you for the fruitfull cooperation during the past couple of years. I am looking forward to the next part of our collaboration.

This would not have been possible without a good working environment. Therefore many thanks to everyone at the IMAU for creating such a good working atmosphere, during lunch, coffee breaks and especially during the BBOS meetings. Also thanks to all Friday afternoon runners of the IMAU and the BBOS musicians and singers I played with during the years. De ijs en klimaat groep bedankt voor de goede discussies, tijdens werkbesprekingen en daarbuiten. Vanaf deze plaats wil ook alle ijs en klimaat AIO's bedanken waarmee ik samen heb gewerkt tijdens de afgelopen 4 jaar. Het HOEMBA overleg is een fijne, nuttige en gezellige bijeenkomst waar we met alle AIO's onze laatste frustraties, bevindingen en overwinningen kunnen delen en vieren. Irene, Marianne, Paul, Jan, Aimée, Stefan, Jan, Ward, Malou, Matthijs en Melchior bedankt. Zonder kamergenoten was het een stuk minder gezellig geweest de afgelopen jaren. Rianne, bedankt voor je altijd goede humeur, je was (en bent!) een fijne kamergenoot. Sinds april zorgt Matthijs ook voor de nodige gezelligheid en enthousiasme in kamer 602, waarvoor dank. Oud studiegenoten Yvonne en Niels ook bedankt voor de interesse, hulp en geklets. Niels veel succes met je laatste loodjes, ik weet zeker dat je het goed gaat doen!

In de zomer van 2010 heb ik de kans gekregen om op veldwerk mee te gaan naar Groenland. Ik wil dan ook Paul Smeets en Wim Boot bedanken voor hun bijdrage hieraan. De (constante stroom van) verhalen over (vroeger) veldwerk waren fascinerend om naar te luisteren. Het bleek maar weer dat planning een relatief begrip is... Het was een geweldige ervaring om nooit te vergeten. Yvonne, Wanda en Sandra bedankt voor jullie ondersteuning, Marcel bedankt voor het goed onderhouden van de iMac. Henk Snellen ook bedankt voor de technische ondersteuning. Ik wil ook graag Peter-Paul Borsboom (ex-IMAU) bedanken voor zijn modelondersteuning in de eerste twee jaar. Michael ook bedankt voor het helpen met het model en de samenwerking in deze.

Zonder ontspanning buiten het werk om was de het schrijven van dit proefschrift een stuk lastiger geweest. Hardlopen is voor mij het belangrijkste middel om even weg te zijn van alles. Hiervoor wil ik dan ook Groep 1 van de Altena Road Runners bedanken voor de altijd goede sfeer en gezonde competitie. Ik hoop dat we nog vele jaren samen zullen trainen naar mooie wedstrijden. Ook de band en de vriendengroep bedankt. Leuke uitjes, verjaardagen, concertbezoeken, ons jaarlijkse weekendje Ardennen, het blijft super gezellig en ik hoop dat we dit nog lang vol zullen houden. Aline, Pieter en Jantine ook bedankt voor het doorlezen van de Nederlandse samenvatting.

Dit alles was onmogelijk geweest zonder mijn naaste familie. Frank, Laura, Erik en Stefanie bedankt. Ook al liggen onze interesses en ons werk wat ver uit elkaar, het enthousiasme voor jullie eigen werk en hobby's werkt inspirerend. Veel dank gaat ook uit naar mijn tweelingbroertje Rob. Bedankt voor alles. Je was me net voor, ik hoop dat ik over 4 jaar aan jouw zijde mag staan ;-). Pa en Ma, dit is bijna niet in woorden te bevatten maar ik ga toch een poging wagen. Zonder jullie steun en vertrouwen, toewijding en liefde (aan ons allemaal) was ik niet de persoon die ik nu ben. Jullie staan altijd voor ons klaar en dat geeft zoveel moed en vertrouwen, bedankt voor alles.

Curriculum Vitae

Bas de Boer werd geboren, samen met zijn tweelingbroer Rob, op 4 april 1982 in het Beatrix ziekenhuis in Gorinchem. Zijn jeugd bracht hij door in Andel en later in Sleeuwijk, waar hij in 1999 zijn HAVO en in 2001 zijn VWO diploma behaalde aan het Altena College. In 2001 begon hij aan de opleiding Meteorologie en Fysische Oceanografie (MFO) aan de Universiteit Utrecht. Tijdens de eerste vijf maanden van 2006 studeerde hij, samen met een aantal studiegenoten, aan de Universiteit van Oklahoma in de Verenigde Staten. In juli 2007 begon Bas met zijn afstudeeronderzoek bij Bart van der Hurk op het Koninklijk Nederlands Meteorologisch Instituut (KNMI) in De Bilt, waar hij onderzoek deed naar de invloed van klimaatverandering op extreme neerslag in Oost Afrika. Na een jaar onderzoek ronde hij in augustus 2007 zijn studie af. In december van datzelfde jaar begon hij aan zijn promotieonderzoek onder begeleiding van Roderik van de Wal bij het Instituut voor Marien en Atmosferisch onderzoek Utrecht (IMAU). Het resultaat hiervan staat opgeschreven in dit proefschrift.

Bas de Boer was born, together with his twin brother Rob, on April 4th 1982 in the Beatrix hospital in Gorinchem. He spent his childhood in Andel and in Sleeuwijk, where he obtained his HAVO diploma in 1999 and his VWO diploma in 2001 at the Altena College. In 2001 he started the study 'Meteorology, Physical Oceanography and Climate (MPOC)' at Utrecht University. During the first 5 months of 2006 he studied, together with a few classmates, at the University of Oklahoma in the United States of America. In July 2007 Bas started his Master research project under the supervision of Bart van den Hurk at the Royal Netherlands Meteorological Institute (KNMI) in De Bilt, investigating the influence of climate change on precipitation extremes in East Africa. After one year of research he graduated in August 2007. In December of the same year he started his PhD research under the supervision of Roderik van de Wal at the Institute of Marine and Atmospheric research Utrecht (IMAU). The results obtained from this research are presented in this thesis.

Publications

First author

De Boer, B., R. S. W. van de Wal, R. Bintanja, L. J. Lourens and E. Tuenter, 2010. Cenozoic global ice volume and temperature simulations with 1-D ice-sheet models forced by marine δ^{18}O records, *Annals of Glaciology*, **51**(55), 23–33.

De Boer, B., R. S. W. van de Wal, L. J. Lourens and R. Bintanja, 2011. Transient nature of the Earth's climate and the implications on the interpretation of benthic δ^{18}O records, *Palaeogeography, Palaeoclimatology, Palaeoecology*, doi: 10.1016/j.palaeo.2011.02.001

De Boer, B., R. S. W. van de Wal, L. J. Lourens, R. Bintanja and T. J. Reerink, 2012. A full assesment of ice-volume variations over the past 1 million years from inverse 3-D ice-sheet modelling, *in preparation.*

Co-author

Shongwe, M. E., G. J. van Oldenborgh, B. J. J. M. van den Hurk, B. de Boer, C. A. S. Coelho and M. K. van Aalst, 2009. Projected Changes in Mean and Extreme Precipitation in Africa under Global Warming. Part I: Southern Africa, *Journal of Climate*, **22**, 3819-3837.

Liebrand, D., L. J. Lourens, D. A. Hodell, B. de Boer, R. S. W. van de Wal and H. Pälike, 2011. Antarctic ice sheet and oceanographic response to eccentricity forcing during the early Miocene, *Climate of the Past*, **7**(3), 869–880.

Maris, M. N. A., B. de Boer, J. Oerlemans, 2011. A model comparison study for the Antarctic region: present and past, *Climate of the Past Discussions*, **7**, 3584-3607.

de Olaizola, M., R. S. W. van de Wal, M. M. Helsen, B. de Boer, 2011. Present-day mass changes for the Greenland ice sheet and their interaction with bedrock adjustment, *The Cryosphere Discussions*, **5**, 3455-3477.

Van de Wal, R. S. W., B. de Boer, L. J. Lourens, P. Köhler and R. Bintanja, 2011. Reconstruction of a continuous and high-resolution CO_2 records over the past 20 million years *Climate of the Past*, **7**(4), 1459-1469.

Koenig, S., A. M. Dolan, B. de Boer, D. J. Hill, R. M. DeConto, A. Haywood, A. Abe-Ouchi, D. J. Lunt, D. Pollard, A. Quiquet, F. Saito, J. Savage, C. Stepanek, 2012. Greenland ice sheet sensitivity and sea level contribution to the mid-Pliocene Warm Period: Pliocene Ice Sheet Model Intercomparison Project (PLISMIP) - Part I, *to be submitted to Climate Dynamics*

Köhler, P., R. S. W. van de Wal, B. de Boer, M. Butzin, T. Bickert et al., 2012. A process-based understanding of the late Cenozoic carbon cycle, *in preparation*